TURBULENT FLOW

OF

DRAG-REDUCING FIBRE SUSPENSION

KWOK TUNG JOHN CHAN

Thesis submitted for the Degree of

Doctor of Philosophy

University of Edinburgh

1980

DECLARATION

I declare:

a) that this thesis has been composed by myself, and

b) that the work described is my own.

K.T.J. Chan
Department of Mechanical Engineering
University of Edinburgh
1980

Contents

Acknowledgements

I would like to thank my supervisor Dr W.D. McComb for his invaluable supervision, direction and continued encouragement, without which this work could not have reached this level.

I would like to thank Professor J.L. King for the permission to use the facilities of the Mechanical Engineering Department.

I would also like to thank Mrs Duncan, Dr G.O. Goudie, Dr G.M. Alder, Mr M. Currie for their helps and considerations, and to thank Mr G. Smith and the technical staffs for their helps to me on some technical problems.

The financial support of the University of Edinburgh in granting me the one-year studenship from 1978 to 1979 is acknowledged with gratefulness.

I am indebted to Dr J.L. Hutchison, who has provided me helpful suggestions to improve the English.

I would like to thank Mr K.H. Ong for his help during the time I did my further work in Edinburgh.

I should like to thank my wife, Rosabella, not only for her typing this thesis but also for her patience all the time when I was preparing it.

I am grateful to my parents who maintained me at university for higher education.

There are three things that
are too amazing for me
... that I do not
understand:
the way of an eagle in the sky
the way of an ...
the way of a ship on the high
seas,

Proverbs 30: 18, 19

Abstract

The turbulent flow of 300 ppm asbestos fibre suspension is studied by using LDA. The effect of degradation of the fibre suspension on the streamwise and transverse fluctuating velocities is examined. For the streamwise component, results of mean velocity profile, turbulent intensity distribution, spectra, correlation, integral length scales and bursting period are presented.

The effect of polymer additive on the fibre suspension is also examined with the LDA, the mixed system being shown to be less degradable.

The results show two distinct flow behaviours of the fibre suspension, one being 'fibre-like' and another 'polymer-like'. The 'fibre-like' behaviour appears to be associated with the undegraded fibre suspension while the 'polymer-like' behaviour associated with the degraded suspension. The transitional behaviour appears to be due to degradation of fibre suspension; the addition of polymer seems to suppress this transition.

NOTATION

Symbol	Quantity
A	Cross sectional area of the pipe
	Area under a correlation curve
	Constant, mean velocity profile
B	Constant, mean velocity profile
b	Fringe spacing
c	Volumetric concentration
	Speed of light
D	Diameter of the pipe
	Diameter of a fibre
DR(%)	Percentage drag reduction
d_{ij}	Deformation tensor
E	Streamwise energy spectrum
$\underline{e}$	Unit wave vector
e	Constant, ln e = 1
f	Friction factor
	Number of wave fronts
Δf	Difference between f and f_o ($= c/\lambda_o$)
f_o	Difference between light beam frequencies of Bragg cells
H_1, H_2	Liquid levels in tank
h_1, h_2	Liquid levels in manometer
K	Oscillator control constant of a tracker
$\underline{k}$	Wave number vector
'Khz'	Doppler frequency in Khz
L/D	Aspect ratio of fibre
L	Distance between two pressure tappings
L_{11}	Turbulence integral scale
M	Constant, the Prandtl-Karman equation
N	Constant, the Prandtl-Karman equation
n	Refractive index
P	Pressure drop (N/m^2)
P(x,y)	Point in probe volume
Q	Flow rate
R	Inner radius of the pipe

Symbol	Quantity
R_{11}	Turbulence correlation coefficient
R_E	Eulerian correlation coefficient
Re	Reynolds number
'Rms'	Root-mean-square of fluctuating signal
r	Outer radius of the pipe
	Separation of two points in turbulence field
s'	Location of the probe volume, transverse LDA
T_B	Bursting period
T_E	Eulerian integral time scale
ΔT	Time taken for liquid to rise from H_1 to H_2
t	Time
	Time lag
	Interval between two subsequent flashes, b/V_y
Δt	Time taken for liquid to rise 1 cm
U	Instantaneous turbulent velocity
U^+	Dimensionless mean velocity, $\bar{U}/u^* = 58\ VOLT/u^*$
$\bar{U}$	Local mean velocity, $\bar{U}(y)$
$\bar{U}_o$	Maximum velocity in the pipe
u	Root-mean-square of the streamwise fluctuations
u^*	Shear velocity,
u^+	$u/u^* = 58\ Rms/u^*$
$\langle u_1^2 \rangle$	Turbulence energy, same as $\langle u_2^2 \rangle$ and $\langle u_3^2 \rangle$
V	Mean flow velocity
$\underline{V}$	Velocity vector of a particle, $\underline{V} = V_x\underline{i} + V_y\underline{j}$
$V_o(t)$	Output varying signal from a tracker
'VOLT'	Output in volt
w	Intensity of the transverse fluctuating velocity
x	Displacement of the 'transverse' LDA system
y	Micrometer reading
	Distance of probe volume from the wall
y_w	Micrometer reading, at the wall
y^+	Distance from wall, dimensionless, u^*y/υ
$Z_1(t)$	Output from LP filter of a tracker
$Z_2(t)$	Output from LP filter of a tracker
γ	Angle defined as in figure A3.b, c
Γ_e	Rate of stretching

Symbol	Quantity
$\partial/\partial t$	Oldroyd time derivative
δ	Angle defined as in figure A3.b, c
θ	Relaxation time of a polymer molecule
	Angle of intersection between two beams
	Angle defined as in figure A3.b, c
θ'	Angle between two beams of the 'transverse' LDA, in air
Δ	Angle defined as in figure A3.b, c
λ, λ_0	Wavelength of light, in medium, in space
μ	Viscosity
μ_e	Effective viscosity of suspension
ν	Kinematic viscosity, μ/ρ
ρ	Density
τ_0	Wall shear stress
τ_{ij}	Deviatoric shear tensor
ϕ	Angle defined as in figure A3.b, c
	Volume fraction of the particle in suspension
$\omega_i(t)$	Instantaneous Doppler frequency
Ω	Angle defined as in figure A3.b, c

Chapter 1 Introduction

Drag Reduction in Fibre Suspensions

Drag reduction has been observed in the turbulent flow of fibre suspensions. Many papers have been put forward in the last two decades, considering the phenomenon and describing its flow characteristics. As yet, no detailed understanding of the mechanism underlying the drag reduction has been accepted. Some of the works are listed in table I-1.

Mih and Parker (1967) used 0.5% suspension of wood pulp fibres to get 33% drag reduction in a pipe of 5 cm diameter, showing that the drag reduction depended on Reynolds number. They also obtained drag reduction with rayon fibre.

They had used an annular purge impact tube (developed by themselves) to measure the local mean velocity in the flow and obtained results which were quite interesting. They found that a turbulent wall region and a plug core region (turbulence free) existed in the flow. In the wall region, the turbulent momentum transfer was shown to be suppressed by fibres. They attributed drag reduction to this.

Bobkowicz and Gauvin (1967), using turbulent diffusion technique, obtained turbulence data for nylon fibre suspension. Keeping the Reynolds number and pipe diameter constant, they examined the effect of fibre additives on the turbulent flow characteristics, showing that the turbulent diffusivity and radial intensity increased with

Table I.1 Drag Reduction of Fibre Suspension in Pipe Flow

Author	Fibre and size	Fluid and Tube I.D., cm	Concentration	Reynolds number	Drag reduction
Mih and Parker (1967)	wood pulp	water - 5.08	0.5%	8.0×10^4	33% *
			1.0%	2.0×10^4	22% *
		- 10.16	0.5%	1.3×10^5	32% *
			1.0%	4.0×10^5	28% *
	rayon $d \approx 17\ \mu m$ $l/d \approx 6 \times 10^3$	water - 5.08	0.2%	4.0×10^4	24% *
			0.5%	1.0×10^5	16% *
		- 10.16	0.2%	2.0×10^5	14% *
			0.5%	3.5×10^5	10% *
Bobkowicz and Gauvin (1967)	nylon $l/d \approx 11 - 51$	water - 5.13	0 - 4%	9.0×10^4	**
Ellis (1970)	TB asbestos $d \approx 0.05\ \mu m$ $l/d \approx 4 \times 10^4$	surfactant solution - 0.115	50 ppm	2.0×10^4	49% - 42% ***
		- 1.43	50 ppm	2.0×10^4	44% - 33% ***

Author	Fibre and size	Fluid and Tube I.D., cm	Concentration	Reynolds number	Drag reduction
Hoyt (1972)	JM asbestos $d \approx 0.02\,\mu m$ $l/d \approx 10^2 \sim 10^3$	0.8% Aerosol OT solution - 0.117	0.5%	1.4×10^4	63% +
	TB asbestos $d \approx 0.05\,\mu m$ $l/d \approx 4 \times 10^4$	0.8% Aerosol OT solution - 0.117	500 ppm	1.4×10^4	65% - 49% ***
Lee, Vaseleski and Metzner (1974)	nylon	water - 2.4	1000 ppm	1.0×10^5	15%
		- 4.9	1000 ppm	5.0×10^5	17%
	JM asbestos $d \approx 0.02\,\mu m$ $l/d \approx 10^2 \sim 10^3$	0.25% Aerosol OT solution - 2.4	200 ppm	2.0×10^5	2.5%
			800 ppm	2.0×10^5	19%
			200 ppm	1.0×10^5	4.5%
			800 ppm	1.0×10^5	21%
		- 4.9	800 ppm	1.0×10^5	18%
		- 7.0	200 ppm	1.0×10^5	13%
			800 ppm	1.0×10^5	22%
	TB asbestos $d \approx 0.05\,\mu m$ $l/d \approx 4 \times 10^4$	0.8% Aerosol OT solution - 2.4	200 ppm	2.0×10^5	27% - 14% ***
				1.0×10^5	22% - 13% ***
		- 4.9	200 ppm	1.0×10^5	28% - 15% ***

Author	Fibre and size	Fluid and Tube I.D., cm	Concentration	Reynolds number	Drag reduction
Kale and Metzner (1974)	nylon $d \approx 5.7\ \mu m$ $l/d \approx 350$	0.25% Aerosol OT solution - 2.42 - 4.86	800 ppm 800 ppm	1.0×10^5 8.0×10^4	25% 25%
Moyls and Sabersky (1978)	TB asbestos $d \approx 0.05\ \mu m$ $l/d \approx 4 \times 10^4$	surfactant (OT) solution - 0.95 smooth tube	300 ppm	7.0×10^4	64% (25.6^oC) *
		rough tube	300 ppm	3.0×10^4	80% (25.6^oC) *
			300 ppm	2.0×10^4	86% (5^oC) *

* drag reduction data are interpolated from the authors' f vs. Re diagrams, Re giving maximum drag reduction.

** drag reduction percentage was not reported.

*** level depends on extent of degradation.

\+ maximum drag reduction in the system.

increasing aspect ratio and concentration and that the turbulence scales depended on them.

They speculated that the increase in the radial turbulent intensity was due to the oscillations of the fibres that were aligned in the flow direction. The oscillations were supposed to be the consequence of interparticle collisions. Referring to the results by Daily and Bugliarello (1961), who showed that in a 5-cm pipe the streamwise turbulent intensity was suppressed by the fibre additives, they suggested that the overall Reynolds stress was suppressed in the suspension.

Ellis (1970) obtained 44% drag reduction with a dilute asbestos fibre suspension. He dispersed asbestos fibres produced by TBA Co. Ltd., England by using a surfactant solution. His results showed that TB asbestos fibre was subject to mechanical degradation like polymer.

Hoyt (1972) used a rotating disc to test the drag-reducing effectiveness of various kinds of fibres. Asbestos fibres were shown to be the most effective kind, with TB asbestos fibres being best.

He used a 304x microscope to examine each of these samples and took photographs, showing that TB asbestos fibres were extremely long and hair-like with entangled appearance. The Johns Manville asbestos fibres were of the same appearance but less entangled.

Peyser (1973), also using a rotating disc apparatus, obtained drag reduction with JM asbestos fibre suspension in Aerosol OT solution. He examined samples of the used

suspension in an electron microscope and showed that less than 10% of the fibres were fully separated and that other fibres appeared to entangle together to form bundles. He could not obtain drag reduction with similar asbestos fibres in ethylene glycol but showed that the photomicrographic appearance of the suspension was almost the same. Therefore, he suggested that it was the separated fibres which were active in drag reduction.

Moyls and Sabersky (1978) obtained friction factor versus Reynolds number curves for a 300 ppm TB fibre suspension in a 0.95 cm pipe, showing that drag reduction depended on Reynolds number and that a minimum point was reached for each curve, after which the friction factor appeared to increase with increasing Reynolds number. They obtained drag reductions up to about 80% and took photographs of these suspensions in an electron microscope. They saw individual fibres among strands of fibres in these photographs and suggested that the individual fibres and strands would have formed a rather dense mesh moving with the fluid, causing drag reduction. They further suggested that the mesh-like structure would have interfered with the motion caused by the turbulence producing vortices. Applying this idea to the drag reduction of polymer solution, they speculated that the polymer molecules might have agglomerated to form mesh-like structures of a suitable scale, interfering with the vortices in the boundary layer. This implies that both fibre and polymer are active in the wall region in reducing drag.

However, it has long been a general question if fibres and polymer molecules behave in the same way in causing drag reduction. A few conflicting suggestions have been presented.

Ellis (1970) stated that individual fibres interacted in some way with the flow instabilities to inhibit their growth like polymer agglomerates do. Peyser (1973) pointed out that individual fibres might be important in drag reduction. Vaseleski and Metzner (1974) and Lee et al (1974) showed however that fibres affected the momentum transfer of the flow in the core region, leaving the flow near the wall unchanged. Their experimental results showed no diameter effect in fibre suspension and that the mean velocity profiles in the core region had slopes changed with concentration of fibre.

Lee et al (1974) showed that when both fibre and polymer were used together, the drag reduction was higher than when using either one alone. They obtained drag reduction up to 94% in the mixed system, indicating that fibre and polymer acted concomitantly in two different manners. More interesting was the fact that the results showed the following observation: the drag reduction was 17% with 1000 ppm nylon fibre suspension; no drag reduction could be obtained in 150 ppm degraded polymer solution alone; however, the drag reduction was 36% in the mixture of them. Sharma, Seshadri and Malhotra (1979) observed the same behaviour in the fibre-polymer system also. This shows that fibre and polymer not only act independently in the flow but also reinforce each other in some way.

Sharma et al (1979) have used a pitot tube to get mean velocity profiles, showing that fibre alone changed the characteristics of the flow in the core but left those in the wall region unchanged. In the fibre-polymer mixture, the viscous sublayer was thickened. Thus, they suggested that, in the mixture, the fibres on the one hand reduced the momentum transfer rate in the core region and on the other increased the effectiveness of the polymer so as to thicken the viscous sublayer, causing additional drag reduction.

Kale and Metzner (1976) also used a pitot tube to measure mean velocity profiles and showed that the slopes of those of the fibre suspensions alone were equal to that of newtonian profile but that they shifted upward. In fibre-polymer mixture, they showed that the profile shifted further up without changing its slope. Therefore, they abandoned their former conclusion (Vaseleski and Metzner (1974) and Lee et al (1974)) and proposed that fibre, like polymer, was active in the wall region in reducing drag.

They thus suggested that fibre partly acted as an independent drag reducer in the wall region and partly interacted with the polymer solution, making it more effective. The mechanism of the interaction was not clearly stated however, but Metzner (1977) has proposed a rheological model, trying to explain the 'synergistic' effect.

In summary, it has been shown in the literature that suspensions of synthetic or papermaking fibres are drag-reducing. They can modify the turbulent flow structure;

in particular, they suppress the streamwise fluctuating velocity and enhance the radial component, seemingly making the turbulent pipe flow more isotropic as compared to the newtonian flow.

Asbestos fibres are found to be the most effective kind of fibres for drag reduction, TB fibre being best. Nevertheless, it is the only degradable fibre found so far. Surfactant solution is needed to disperse the asbestos fibre in preparing the suspension. In the electron microscope, the TB fibre suspension sample appears to be hair-like and to entangle together to form bundles, 10% of the fibres being fully separated.

The suggestion has been put forward that individual fibres are responsible for the drag reduction in fibre suspension. A conflicting idea has also been proposed that the entanglement of individual fibres and strands are responsible.

It has been shown that by using polymer and fibre together one can obtain a drag reduction level greater than the sum of the drag reductions when they are used alone.

The current understanding of the mechanism of the drag reduction of fibre suspension is still based on speculations, more experimental work should be done to describe the flow structure of the fibre suspension in the turbulent regime.

Drag Reduction in Polymer Solutions

Drag reduction by polymer additive was first reported by Toms (1948). He showed that 5 ppm of dilute polymer solution could have a mean flow rate much larger than that

of the solvent alone under the same pressure gradient. This is the essence of the drag reduction. The results are fascinating in the diluteness of the polymer solution used. He had used poly-methylmethacrylic in mono-chlorobenzene solution to get the drag reduction which was about 80%.

The discovery appeared not to attract much attention until Savins(1961) elucidated the drag reduction characteristics of polymer solution in turbulent flow by replotting the results of Toms in friction factor (f) versus Reynolds number (Re) diagrams, showing some interesting features.

Virk et al (1967) have pointed out two special features of drag reduction by polymers, one being the specific value of the onset wall shear stress and the other the maximum drag reduction asymptote.

They showed that the onset wall shear stress must be exceeded before drag reduction occurred in the turbulent flow of polymer solution. Collecting drag reduction data from various sources, they showed that the onset wall shear stress was dependent on polymer species only but independent of pipe diameter and roughness of the pipe wall (Virk, 1971). Virk (1975) showed that it was not dependent on the concentration of the solution and the viscosity of the solvent.

Virk et al hypothesized that onset occurs when the turbulent scale alters itself to a certain small value so as to interact with the polymer molecules. The hypothesis was shown to be reasonable for they found that the turbulent length scale (micro-scale) and the characteristic polymer length scale (radius of gyration) correlated rather well.

Yet, Lumley (1969) disagreed with this point of view; he argued that the smallest turbulence scale at onset is still much larger than the radius of gyration of the polymer molecule.

As an alternative, he suggested that the polymer molecules might have expanded in the turbulent flow, interacting with the turbulent small eddies. Onset of drag reduction occurs when the smallest flow time scale $\nu/(u^*)^2$ is comparable to the molecular relaxation time. The results of Virk et al showed that the relaxation time of the polymer did not correlate well with the flow time scale, disagreeing with the 'time' hypothesis. However, Berman and George (1974), using mono-disperse polymer species, showed that the 'time scale' data correlated rather well supporting the 'time' hypothesis.

The criterion suggested by Lumley (1973) for onset of drag reduction is

$$\left(\frac{u^{*2}}{\nu}\right)\theta \leqslant \frac{3}{2} \quad ,$$

where θ is the relaxation time of the polymer molecule.

Virk et al showed that the maximum drag reduction data from various sources clustered together, forming a straight line in a Prandtl-Karman diagram. The equation of the line was written as,

$$\frac{1}{\sqrt{f}} = 9.5 \log (Re\sqrt{f}) - 19.06$$

appearing to be universal. It is usually called the maximum drag reduction asymptote or simply called Virk's asymptote. It seems to set a limit beyond which no drag reduction data

can go, whatever the concentration of any given polymer solution is.

For newtonian fluid of zero drag reduction, the friction factor - Reynolds number relationship is written as,

$$\frac{1}{\sqrt{f}} = 2.0 \log (Re\sqrt{f}) - 0.8 \quad ,$$

for a smooth pipe. It sets the lower limit for drag-reducing flow of dilute polymer solution. It is known as the Prandtl-Karman law for the newtonian fluid (Schlichting, 1955) and can be obtained by integrating the mean velocity profile of the newtonian fluid,

$$U^+ = 2.5 \ln y^+ + 5.5 \quad ,$$

and through the definitions: $1/\sqrt{f} = V/u^*$ and $Re\sqrt{f} = u^* D/\nu$.

The general equation of a velocity profile can be written as,

$$U^+ = A \ln y^+ + B \quad ,$$

and the general equation of the Prandtl-Karman relationship is represented by

$$\frac{1}{\sqrt{f}} = M \log Re\sqrt{f} + N \quad ,$$

where A, B, M and N are constant coefficients related by the following matrix relation:

$$\begin{bmatrix} A \\ B \end{bmatrix} = \begin{bmatrix} 0.615 & 0 \\ 1.562 & 1.414 \end{bmatrix} \begin{bmatrix} M \\ N \end{bmatrix} \quad .$$

By using this relation, Virk, Mickley and Smith (1970) have shown that an ultimate velocity profile, corresponding to the maximum drag reduction asymptote, should have an equation,

$$U^+ = 11.7 \ln y^+ - 17.0 \quad .$$

Collecting experimental data from various sources, Virk (1971) showed that the mean velocity profiles of polymer solutions were bounded by the ultimate asymptote and the newtonian profile. The enclosed region is called the polymeric regime.

Figure 1.1 shows the mean velocity profiles measured in poly-acrylamide solution by Seyer and Metzner (1969) and by Rudd (1972). Seyer and Metzner used bubble tracer photographic method; Rudd used LDA. The velocity profile of Seyer and Metzner appeared to lie around the Virk's asymptotic profile, that of Rudd showing three regions. One was the thickened viscous sublayer, extending to $y^+ = 20$. The intermediate layer extended along the asymptotic profile until the layer having a slope equal to that of the newtonian profile appeared. The last in the core region extended to the centre-line of the pipe.

According to Virk (1975) and Virk et al (1967), the intermediate layer has a constant slope independent of the level of drag reduction, equal to that of the asymptotic profile, and they called it the elastic sublayer. Its thickness was dependent on the drag reduction percentage, showing two extreme cases: at zero drag reduction, it disappeared, leaving the newtonian profile intersecting with the viscous sublayer at $y^+ = 11.6$. At maximum drag reduction, the core layer disappeared and the elastic sublayer extended to the centre-line of the pipe from $y^+ = 11.6$.

Recent LDA results however do not agree with Virk's

elastic sublayer model. Figure 1.2 shows mean velocity results by McComb and Rabie (1979), showing a particular feature that this model cannot include.

The velocity profile did show that there were three distinct regions in the flow of polymer solution undergoing drag reduction. The intermediate layer however did not show a constant slope but its slope appeared to vary with drag reduction percentage. Such a result agreed with that of Reischman and Tiederman (1975) which appeared to have a slope invariant with Reynolds number and drag reduction. However, they themselves were doubtful of the universality of the velocity profiles in the intermediate region and suggested making more systematic measurements to clarify this effect.

Notwithstanding these disagreements about the intermediate layer, all of these investigators have concluded that it was the active region in reducing turbulent friction in the flow.

Using an injection technique, McComb and Rabie (1979) were able to demonstrate that only when the polymer molecules were present in the near wall region did the mean velocity profile become changed and drag reduction appear.

Not only this, the turbulent structure had been changed according to the level of the drag reduction. Figure 1.3 is the turbulent intensity distribution of the polymer solution given by McComb and Rabie, showing that the streamwise fluctuating velocity was enhanced by the polymer solution. It tended to the newtonian distribution as the

drag reduction decreased.

Figure 1.4 shows their auto-correlation curves of the streamwise velocity fluctuations. It can be seen that the auto-correlation increased with increasing drag reduction, indicating an increase in the integral scale compared with the newtonian result. A trend to the newtonian curve can be seen as the drag reduction decreases. The increase in integral scale agreed with the result of Hanratty et al (1977).

In McComb and Rabie's work, the bursting rate was shown to be suppressed by the polymer additive compared with the water result, showing the inhibition of the turbulent production rate. Mizushina and Usui's results also showed such a suppression.

Proposed Mechanisms of Drag Reduction

The earliest mechanism of drag reduction was proposed by Toms himself (1948). After his discovery of the drag reduction phenomenon, his discussion with Oldroyd led him repeat the experiment in a pipe of different size. He noticed that the flow of the same polymer solution in the larger pipe had smaller drag reduction, thus concluding that the drag reduction was due to a wall effect. Based on this, he hypothesized that the flow contained a shear-thinning wall layer which, by virtue of low viscosity, would give lower frictional coefficient than the pure solvent.

However, it has been shown that the dilute polymer solutions which were also effective drag-reducing agents

were not shear-thinning (Hoyt and Fabula, 1964). Walsh even found that the drag-reducing polymethacrylic acid was in fact shear-thickening. Thus, the shear-thinning hypothesis suggested by Toms was not quite acceptable.

Trying to explain the Toms effect and assuming it as a wall effect, Oldroyd (1949) hypothesized that the tube wall might induce a preferred orientation of the polymer molecules close to the wall in such a way that an abnormally mobile laminar sublayer could arise, causing drag reduction. However, there was no evidence to show the existence of such a mobile layer in the turbulent flow of the dilute polymer solution.

El'perin and Smol'sku (1965) have suggested a theory that the absorption of the polymer molecules on the pipe wall might lead to an effective slip phenomenon, causing drag reduction. El'perin et al (1967) further proposed that the absorbed layer would in some way lower the viscosity near the wall, create a slippage effect, dampen turbulence pulsations, and prevent the initiation of vorticity at the wall.

Davies and Ponter (1964) observed that the drag-reduction effect persisted for some time after the flowing polymer solution was switched to pure solvent, supporting the wall absorption theory. However, Little (1969) showed that the persistence of drag -reduction effect he had demonstrated in 1967 was in fact due to the back-diffusion of the polymer solution which had been trapped in the pressure gauge piping before switching. Peyser et al (1971)

showed that the surface composition of the disk rotating in the drag-reducing polymer solutions did not seem to change the level of drag reduction. In other words, drag reduction did not depend on the surface composition of the disc; this could imply that the wall absorption explanation is unlikely.

In recent years, it has become evident that drag reduction in polymer solution is due to some sorts of direct 'interactions' between the turbulent motions and the polymer molecules. The basic difficulty in this regard however is the small size of the individual polymer molecules compared with the smallest turbulent eddies (Kolmogorov eddies). In order to cope with this difficulty, Lumley (1969) has suggested two possibilities: either molecular aggregates are formed in the flowing dilute polymer solution or the molecules are expanded individually by the flow during drag reduction. Because of the diluteness of the drag reducing polymer solution, the formation of the aggregates on the flowing solution is quite hard to imagine. However, in more concentrated solution, they have been observed in shear flows. Yet, no observation has been made to find their existence in turbulent flow.

It is also rather difficult to imagine the process of polymer extension in turbulent flow. Turbulent flow is highly rotational so the orientation of the non-extended molecule is changing with time. In fact, no experimental observation of the extension of polymers in turbulent flow has been reported (Berman, 1977; Lumley 1977; and Hinch,

1977).

Hinch has presented an interesting theoretical result showing that the rate of strain has to be strong enough to 'threshold' the distortions of the polymer molecules, implying that the interaction must be between the molecules and the strong straining motions in the flow. Modern research in the turbulent boundary layer showed that such strong straining motions are possible in the near wall region, accompanying the bursts. Seyer and Metzner (1969) have indicated the possibility that the polymer might have interacted with the near wall double-roller eddies (found by Bakewell and Lumley, 1967), inhibiting their capacity to transfer momentum, thus causing drag reduction.

Several rheological models could be used to form the constitutive equations of the polymer solution. Batchelor (1971) has presented a rigid-rod model, showing that in a pure straining flow, the effective viscosity of the suspension of the elongated rods is given by

$$\mu_e = 3\mu\left(1 + \frac{4}{9}\, c\, \frac{L^2/D^2}{\ln \frac{\pi}{c}}\right) ,$$

where L/D is the length to diameter ratio, c the volumetric concentration of particles, μ the viscosity of the suspending fluid alone.

For elastic particles (like polymer molecules), the problem is less simple because the aspect ratio (L/D) is itself time-dependent. Since it is more realistic, Hinch has used a modified elastic dumb-bell model to tackle the problem. Using this model, he could show that the exten-

sional viscosity of the polymer solution could be as high as 6×10^3.

Macroscopically, some rheologists like to consider the polymer solution as a viscoelastic fluid. Seyer and Metzner (1969) for instance have utilized the convected Maxwell model to portray the response of polymeric solutions to deformation, the expression was written,

$$\tau_{ij} + \theta \frac{\delta \tau_{ij}}{\delta t} = 2\mu d_{ij} \quad ,$$

where τ_{ij} is the deviatoric (bulk pressure part is ignored) shear tensor, θ being the relaxation time. $\delta/\delta t$ is the Oldroyd time derivative defined as,

$$\frac{\delta \tau_{ij}}{\delta t} = \frac{\partial \tau_{ij}}{\partial t} + u_m \frac{\partial \tau_{ij}}{\partial x_m} - \tau_{mj} \frac{\partial u_i}{\partial x_m} - \tau_{im} \frac{\partial u_j}{\partial x_m} \quad ,$$

and the deformation rate tensor is

$$d_{ij} = \frac{1}{2} \left(\frac{\partial u_i}{\partial x_j} + \frac{\partial u_j}{\partial x_i} \right) \quad .$$

In steady extensional flows, they showed that the extensional resistance to the flow is given by

$$\mu_e = \frac{4\mu \Gamma_e}{1 - (2\theta \Gamma_e)^2}$$

where Γ_e is the rate of stretching of the flow. If the extensional flows do not persist for long (e.g. the flow in a double-roller eddy or in a burst), Metzner (1977) suggested a time-dependent resistance to deformation which is given by

$$\mu_e = \mu \left[\frac{2}{1 - 2\theta \Gamma_e} \left\{ 1 - \exp - \left\{ \frac{(1 - 2\theta \Gamma_e)t}{\theta} \right\} \right\} + \frac{1 - \exp - \left\{ \frac{(1 + \theta \Gamma_e)t}{\theta} \right\}}{1 + \theta \Gamma_e} \right] .$$

This is for the special case in which an unstressed element of fluid is subjected to an extension at a constant rate Γ_e for time t.

These formulae indicate that the extensional resistance to deformation is very high if the stretching rate Γ_e is large, provided that the condition $2\theta\Gamma_e < 1$ is satisfied.

Nevertheless, Little et al (1975) did not seem to be satisfied with the mathematical simplicity of using the convected maxwell model; it did not provide a good description for polymer solutions because the responses of the solvent and the polymer did not combine as a simple sum. Consequently, they proposed a two-element model which was developed by Oldroyd (1950). As the mathematics is very complicated, we are not going to reproduce the equations here. Despite the complication, they reached the same conclusion as Seyer and Metzner, that extensional flow must be given serious consideration as an explanation of drag reduction.

All these theoretical results pointed to the conclusion that the presence of polymer additive in strong flow (strong enough to threshold the extension of the polymer molecules) caused a high resistance to stretching deformation. Experimental support can be found in the excellant review of Jeffrey and Acrivos (1976). Batchelor (1971) has discussed the experimental result of Weinberger (1970) in favour of his own theory.

So far we have discussed only on the side of the

rheology. About the extensional flow structure in the turbulent boundary layer, we cannot say much but present the following facts.

Kim, Kline and Reynolds (1971) and Wallace, Eckelmann and Brodkey (1972) showed that the bursting process is related to turbulence production, that it consists of a sequence of deterministic events, and that the dominant features of the process are the outward 'ejection' of low-speed fluid and the inward 'sweep' of the fluid to the wall. The time period between bursts is the longest time scale in the flow field, its reciprocal being a measure of the turbulence production rate. That is, the more frequent the occurrence of burst the higher the rate of turbulence production.

Several methods can be used to measure the bursting rate, one of which is the short-time auto-correlation method. To measure the bursting period, one needs to measure the distance (in time) between two peaks of the quasi-sinusoidal auto-correlation curve.

The time period between bursts has been proved to be scaled by the outer parameters of the flow (Laufer & Badri Narayanan, 1971). They found that $\bar{U}_o T_B/R$ was a constant, where $\bar{U}_o$ was the maximum velocity and R was the length scale of the flow.

Mizushina and Usui showed that the bursting period increase with increasing polymer concentration. McComb and Rabie indicated that the bursting period was substantially enhanced by the polymer additive. Donohue and Tiederman

(1971) showed a suppression of the activity in the turbulent structure with polymer additives. McComb and Rabie demonstrated clearly that the presence of polymer in the near wall region is the necessary condition for the observation of drag-reducing effects. They found that even the change in turbulence characteristics in the core region depended on the concentration of the polymer in the near wall region. McComb and Rabie (1978) showed the evidence of interaction between the wall injected polymer solution and the turbulent burst. Donohue, Tiederman and Reischman (1972) showed that the polymer additives affected the production of turbulence energy directly.

According to Offen and Kline (1975) and Willmarth (1975), vortex stretching plays a main part in the bursting process. Thus, it may be possible that polymer molecules 'interact' with this stretching motion but this is only a conjecture.

So far, we have mentioned the possible mechanisms only for polymer solution; for fibre suspension comparatively fewer proposals can be seen in the literature.

Seyer and Metzner have suggested that the high extensional resistance to deformation of dilute polymer solution leads to a reduction in the momentum transfer from the wall to the core of the pipe. In newtonian fluid, the momentum transfer was thought to be due to the double-roller eddies which was first recognized by Townsend (1956) and their existence was confirmed by the experiment of Bakewell (1966). Kale and Metzner (1976) showed that fibres could also reduce

the momentum transfer as the polymer did, suggesting that they interacted with the double-roller eddies near the wall as well.

Assuming zero Reynolds number of the fibre, McComb (1973) has indicated that fibres will take a preferential orientation spending most of their time closely aligned with the flow direction. Considering the flow in the x_1 direction, he reported that small eddies will tend to deform the fibres preferentially in the (x_1, x_2) plane and (x_1, x_3) planes, and to dilate them in the x_1 direction. Taking account of deformations, he pointed out that these effects would give rise to an anisotropic viscosity.

He was able to derive a constitutive equation for the suspension and obtained equations of motion in wave-number space for the fluid. The algebraic procedure in formulating those equations were out of the scope of the present work, so we shall only elucidate the results which were implied in them.

He noted in his equations that a two-dimensional turbulence field is created at high wave-number. Since energy tends to flow from large $\underline{k}$ (wave-number vector) to small $\underline{k}$ in a two-dimensional turbulence field (Batchelor, 1969), we can imagine that a two-dimensional field is created at all values of $\underline{k}$. That is to say, the scale of the small eddies are growing until they are restricted by the solid boundary of the flow. This will then change the overall structure of the turbulence, especially important at the low wave-number range. He predicted therefore that

with the fibre, one may see an enhancement of $\langle u_2^2 \rangle$ and $\langle u_3^2 \rangle$ with a corresponding decrease in $\langle u_1^2 \rangle$. In other words, the mechanism involved the transfer of energy to transverse and radial fluctuating velocity from the streamwise component.

As we have mentioned previously, Daily and Bugliarello (1961) showed that the streamwise fluctuating velocity in a pipe flow was suppressed by the fibre additives, while Bobkowicz and Gauvin (1967) showed that the radial component of the turbulent fluctuations in a pipe flow was enhanced, depending on the aspect ratio of fibre. These results supported McComb's hypothesis.

In McComb's paper, the mechanism of transfer of the energy between components appeared to be by means of the creation of the two-dimensional turbulence field. Bobkowicz and Gauvin suggested that the increase in radial fluctuation was due to the vibration of the aligned fibres.

Aims of present work

The major objective is to examine the effect of the most effective asbestos fibre (TB fibre) on the structure of turbulence in the pipe, hoping that the description of the modified turbulent flow of the fibre suspension could shed some light on the understanding of the mechanism of drag reduction. Another objective is to look at the results we obtained in the fibre suspensions and see whether or not they behave like those results other investigators obtained in the polymer solutions. One further objective, which arose in the later stage of our project, is to examine

the change in the behaviour of the turbulent flow of the fibre-polymer mixture compared with those of the fibre or newtonian fluid alone, knowing that this could give us more information to consider the behaviour of the transition between two mechanisms.

Chapter 2 Experimental Rig

A blow-down rig has been used, figure 2.1 showing the flow diagram of the experimental set-up. The header tank was used to prepare and contain the working fluids - fibre suspension or fibre-polymer mixture. The tank dimensions were 123 x 60 x 157 cm^3, as shown in figure 2.2. Alongside the header tank, a side-glass tube was fixed beside a meter ruler on the tank, a flexible tubing connecting it with a small outlet hole at the bottom of the tank. Together with a stop watch, this formed a flow meter.

The prepared fluid in the header tank could be allowed to flow under gravity into the pressure vessel by opening valve V1 while V5 was closed and V6 open.

The pressure vessel was used to press the fluid through the working pipe back to the header tank by opening V2 and by compressing the air inside the vessel. The pressure in the vessel was kept at 20 psi by using an adjustable pressure regulator to maintain a steady flow and its magnitude could be monitored with the pressure gauge.

The working pipe, made of perspex, was 380 cm long with an internal bore diameter 1.95 cm. It was transparent, allowing the use of LDA for velocity measurements. Pressure tappings, 3 mm in diameter, were located at 60 cm intervals. The test section was located 154 diameters from the inlet to ensure fully developed flow. The diameter of the pressure tappings was large enough to prevent clogging of fibres.

The 'liquid-in-glass' manometer was used to measure the pressure drop, using liquid of specific gravity 1.58 at

$20^{o}C$. The room temperature in the laboratory was maintained at around $16^{o}C \pm 2^{o}C$ throughout the project, ensuring a constant specific gravity of the manometer fluid.

The Y-joint was used to make use of the by-pass system which was designed chiefly for emptying the working fluid in the pressure vessel back to the header tank. If the fluid was not emptied after a run, the remaining fluid would mix with the previously degraded fluid, obscuring the study of the effect of degradation.

The flow regulator was used to control the flow rate and V4 was used to start the flow.

A thermometer was used to measure the temperature of the flowing fluid before it returned to the header tank at the outlet of the flow system. The kinematic viscosity of the fluid can be found from a table by the use of the measured temperature of the fluid. Throughout our experiment, we have used the kinematic viscosity of water as that of the suspensions or fibre-polymer mixture. According to Einstein's formula, the increase in viscosity of 300 ppm (by weight) fibre suspension (or 125 ppm by volume) is about $\frac{5}{2}\phi = 0.00031$ or 0.03%. On the other hand, the density of the fluid does not change very much (0.03%); therefore, the kinematic viscosity of the suspension is assumed not to be very different from that of water.

The valve V6 was used to discharge the air in the pressure tank to the atmosphere after each run, equalizing the pressure inside and outside, to let the fluid return to the vessel and be used again.

A stirrer was fixed on the header tank as shown in figure 2.2, used for mixing the working fluid in the tank. Great care was taken to prepare the working fluid, we attempting to minimize the possibility of mechanical damage of the fibre suspension which was susceptible to degradation.

Calibrations

The side-glass tube alongside the header tank was used as a flow meter measuring flow rate in the pipe. The header tank, apparently uniform in cross-section with an area of 0.738 m^2, had a valve V7 to drain; V7 should be closed for measuring the flow rate.

When the liquid level rises 1 cm in the tank during an experiment in Δt seconds, one obtains 0.00738 m^3 of liquid: the flow rate must be

$$Q = \frac{0.00738}{\Delta t} \ m^3/sec \ .$$

Since the cross-sectional area of the working pipe is 0.0002986 m^2, the mean flow velocity is equal to

$$V = \frac{Q}{A} = \frac{24.7}{\Delta t} \ m/sec \ .$$

More generally, suppose the liquid level increases from H_1 to H_2 during the experiment in ΔT sec., it is quite easy to derive that

$$V = 24.7 \times \frac{H_2 - H_1}{\Delta T} \ (m/sec) \ .$$

The formula was used to calculate the mean flow velocity of the flow in the working section. $H_2 - H_1$ was measured in cm by using the meter ruler beside the side-glass tube.

For pressure drop measurement, it is also quite easy

to show that the pressure drop,

$$P = 56.92\ (h_2 - h_1) \quad \text{(Newton/m}^2\text{)}$$

where $h_2 - h_1$ is the difference in height in cm between manometer fluid levels on both side of the manometer.

Performance of the flow rig

To test the performance of the rig, friction factor versus Reynolds number was measured for the newtonian fluids - water or Aerosol OT solution , and compared with the Blasius formula,

$$f = \frac{0.316}{Re^{0.25}} \quad ,$$

which has been verified by Nikuradse (1933).

The friction factor, f, is given by

$$f = \frac{P}{L} \times \frac{D}{\rho V^2}$$

where L, D and ρ are, respectively, the length between the pressure tappings, diameter of pipe and density of water, assumed to be constant. The Reynolds number, Re, is given by

$$Re = \frac{VD}{\nu}$$

where ν $(=\mu/\rho)$ is the kinematic viscosity, depending on temperature.

Figure 2.3 shows data for water (solid circles) and 0.5% Aerosol OT solution (hollow circles). They agreed very well with the Blasius line, giving less than 1% error, implying the following points:

1. The pipe was smooth.

2. The turbulent flow was fully developed in the

working section.

3. The Aerosol OT solution was not drag-reducing, remaining newtonian, agreeing with the results of Ellis (1970), Hoyt (1972), Lee et al (1974) and Moyls and Sabersky (1978) who showed that the addition of the Aerosol OT had no significant effect on friction.

Preparation of working fluid

To prepare the fibre suspension, 0.5% Aerosol OT solution was used as necessary. TBA Industrial Products Ltd., the supplier of the 2% chrysotile asbestos dispersion, suggested that it be diluted with 0.1% surfactant solution. However, we found that Lee et al (1974) and Hoyt (1972) had suggested using 0.8% Aerosol OT solution for dispersing the same kind of fibre. We decided to use 0.5% surfactant solution, which gave a good drag reduction percentage in a preliminary experiment with the fibre suspension.

All the working fluids - fibre suspensions and fibre-polymer mixture - were prepared in the header tank.

At first we used 0.1 m^3 of 0.5% Aerosol OT solution to dilute the supplied dispersion in a plastic bucket, mixing it with a piece of wooden rod from time to time for about one hour, ensuring well dispersed suspension. Then we poured the mixed suspension in the header tank with a smaller bucket, rather slowly and gently. In the tank suitable volume of 0.5% Aerosol OT solution had already been prepared and after mixing with the poured suspension, we got a 300 ppm suspension. The volume of the suspension

needed to be prepared according to the Reynolds number used, the higher the Reynolds number the more the quantity of fluid.

We mixed the fluid for about 20 minutes and allowed the fluid to remain in the tank overnight, ensuring a well dispersed working suspension. The following day, we stirred the suspension again gently for about 10 minutes, and allowed the fluid to flow under gravity into the pressure vessel.

To prepare the fibre-polymer mixture, the procedure was somewhat similar to that described above, the only difference being that 150 ppm polymer solution was prepared in the bucket first and then mixed with the 0.5% Aerosol OT solution in the tank. After that the supplied fibre dispersion was added directly into the tank and stirred to mix.

Chapter 3 The Laser Doppler Anemometer

Introduction

The Laser Doppler Anemometer (LDA) is based on the Doppler effect and has been used by a number of investigators studying drag reducing turbulent flow of polymer solutions.

Rudd (1972) measured the turbulent velocity of a polymer solution in a 1.27 x 1.27 cm^2 square duct. The LDA was used in the real fringe mode, with a resolution of 10 μm and an ability to make measurements down to about 50 μm as he claimed. The flow was circulated by a peristaltic pump in order to reduce the degradation of the polymer solution to a minimum. His results showed that the streamwise fluctuating velocity was enhanced and that the transverse component was suppressed, compared to water. The mean velocity profile was shown to be flatter than that of water alone, displaying a thickened viscous sublayer. His measurements were possibly subjected to the following influences: firstly, the secondary flow in the square duct might affect the turbulent structure of the flow, and secondly, the peristaltic pump might induce a periodic disturbance.

Logan (1972) measured the streamwise and transverse turbulent fluctuating velocities as well as the Reynolds stress in a polymer solution in a 1.27 x 1.27 cm^2 square duct, using a constant-head tank to obtain the flow. His LDA was different from that of Rudd's; it was used in the reference beam mode, enabling him to measure the Reynolds stress. His results, however, agreed broadly with the intensity results of Rudd. The Reynolds stress was found

to be lower than that in water alone. Yet, his results were possibly influenced by the secondary flow in the square channel, also.

Recognizing the influence of the secondary flow effect, Reischman and Tiederman (1975) have used an LDA to study the flow of a polymer solution in a 2-dimensional rectangular channel. Its aspect ratio was 11 with the channel width 2.6 cm. The channel was 178 cm long, with a test section 140 cm downstream from the entrance. Their LDA was in a real fringe mode, arranged in such a way that the scattered light was collected from a cone incident beam - a side-scatter arrangement. 'Individual realizations' were used to find an estimate of the mean velocity and the streamwise turbulent intensity. Their results were quite different from those of Rudd's and Logan's, showing no thickened viscous sublayer in the mean velocity profiles and a less marked change in streamwise intensity.

Chung and Graebel (1972) measured the streamwise instantaneous fluctuations of dilute polymer solutions in a pipe of internal diameter 1.2 cm. The pipe was made of brass, but with a plexiglass test section for the use of the LDA which was set up in the real fringe mode. Their measurements were limited to the pipe core only, due to the large probe volume of their LDA. Their results showed a suppression of the streamwise intensity and a flatter mean velocity profile compared with the water result.

Mizushina and Usui (1977) measured the turbulent fluctuating velocity in a polymer solution in a pipe of

internal diameter 2.5 cm by the LDA, of resolution 0.8 mm, in the reference beam mode. They obtained results for the streamwise turbulent intensity and the bursting rate, showing both to be suppressed. Their mean velocity at maximum drag reduction lay somewhat beyond Virk's asymptotic profile, while still maintaining a newtonian slope in the core region. Their results might not be reliable, owing to the poor spatial resolution (0.8 mm) of the LDA. Using LDA, McComb and Rabie (1979) measured the instantaneous turbulent velocity in a 2.54 cm pipe. The LDA system was used in the real fringe mode, with a resolution of 0.13 mm. The polymer solutions were injected either at the centre-line or at the wall, upstream of the test section. Drag reduction varied along the pipe downstream from the injector, and their measurements were made at different positions downstream from it.

Their results showed that the mean velocity profiles were in the polymeric regime, tending to the newtonian result as drag reduction decreased. The turbulent intensity and the auto-correlation increased with increasing drag reduction. The bursting rate was suppressed. The energy spectrum were essentially unchanged, except showing a suppression of small scale eddies and a shift of the spectral curve towards lower value of wave-number.

Development of the LDA

Concentrating upon the historical development of the LDA, we shall particularly emphasize the relevant aspects of the technique about our own LDA systems.

Yeh and Cummins (1964) were the first to use an LDA to measure the local velocity in a laminar flow of water with a 5 mW He-Ne laser, using monodispersed polystyrene spheres of diameter 0.557 μm as the scattering particles. It was used in the reference beam mode. Their results agreed with theoretical profile of laminar flow.

Foreman, George and Lewise (1965) first tried to measure the local velocity in a gas by an LDA with a 5 mW He-Ne laser in the reference beam mode, using smoke to seed the flow. Their tube was 5 mm in diameter, made of glass. In a laminar flow, at the centre-line, they obtained results demonstrating that LDA was able to measure velocity in a gas flow.

Foreman et al (1966) have applied the same LDA to measuring velocities in the NASA high speed wind tunnel, again using smoke as scattering particles. They showed that the LDA was able to measure velocity up to 305 meter per second in the NASA tunnel, noting that it should be capable of measuring gas velocity as high as 1830 meter per second as well. They pointed out furthermore that its capability of measuring high velocity could be improved by using a microwave phototube as a photodetector or by shifting the frequency of the reference beam with a light frequency shifter.

They have measured velocity in a 2.2-cm pipe flow of water, giving results comparable to the theoretical laminar profile. A tracking filter, based on the phase-locked loop FM demodulator, has been used to process the Doppler signal.

They attempted to measure the velocity fluctuations, but the results were not reported in their paper.

Goldstein and Hagen (1967) used an LDA to measure the turbulent intensity. The LDA was used in the reference beam mode. They used polystyrene particles of diameter 0.557 μm as seedings. Using spectrum analysis to examine the Doppler signal, they found the Doppler spectrum broadened; the broadening of the spectrum allowing them to calculate the turbulent intensity. Nevertheless, in their investigation, spectra of appreciable width were also observed with the laminar flow, in which case, it should have been zero owing to the constant velocity. They said that the width was due to the uncertainty in the direction of the wave vector of the converging beams. It was, in effect, determined by the optical properties of the LDA only, and thus constant for a given LDA. Therefore, the method of determining the variance of the turbulent fluctuations should involve subtracting the square of the ambiguity broadening from the variance of the spectrum obtained with the turbulent flow.

Pike et al (1968) considered the same problem independently, using their LDA in the reference beam mode with milk as seedings. The Doppler frequency spectra obtained in a laminar flow were shown to be broadened. They compared this with the Doppler radar ambiguity, attributing the broadening effect to the finite size of the probe volume, calling it the Doppler ambiguity. This is sometimes called the finite transit time effect.

In their analysis of an LDA, Adrian and Goldstein (1971) indicated that both ways of considering the 'ambiguity broadening' are equivalent owing to the intimate relationship between the probe volume size and the uncertainty of the wave vector of the beams.

Independently, Edwards et al (1971) indicated that the wave vector ambiguity and the Doppler radar ambiguity are in fact equivalent. They are related through the laws of Fourier transforms and cannot be treated independently. Angus, Edwards and Dunning (1971) explained this in terms of the uncertainty principle in the theory of Fourier transform, saying: "constraining a field to a very small region of $\underline{x}$ (physical space), means a large uncertainty in the $\underline{x}$ component of the wave vector $\underline{k}_x$ and vice versa".

In their paper, Edwards et al (1971) pointed out that not only finite transit time effect contributed to the ambiguity broadening of the Doppler spectrum, but there were also other influential factors which were shown to be:

(1) diffusion broadening caused by the random Brownian motion of the scattering particles,

(2) spatial variations in the velocity within the probe volume, and

(3) interaction effects between the diffusive motions of the scattering particles and the finite size of the probe volume.

Some more factors were indicated by George and Lumley (1973). They were:

(1) the turbulence contribution through the broadening

due to variations in velocity across the scattering volume, and

(2) the Laser source broadening.

Measurements of turbulence spectrum by LDA are subjected to the influence of ambiguity broadenings as well. Greated (1969) measured spectra of grid generated turbulence in polymer solutions and in water by LDA. He found anomalous results even when measured in water. This may be because he did not account properly for the Doppler ambiguity (George and Lumley (1973)).

Chung and Graebel (1972) presented LDA results of turbulence spectra. A range of $-\frac{5}{3}$ slope was displayed in most of the measured spectra. It seems that their results were not affected noticeably by the Doppler ambiguity, possibly because their probe volume was large. As George and Lumley (1973) pointed out, the Doppler ambiguity was seen to arise primarily from the effect of finite transit time of particles through the probe volume and velocity fluctuations within the volume. Wang (1973) showed that the effect of the finite transit time for the scattering particles to cross the probe volume was equivalent to a white noise with an amplitude inversely proportional to the average transit time or the beam diameter. Hence, increasing the probe volume size will reduce this effect but make the spatial resolution of the LDA poorer; thus, reducing the maximum measurable frequency of the turbulent velocity. George and Lumley (1973) suggested that in all but the most unusual circumstances, the size of the probe volume should

be determined for minimum ambiguity. The spectral values obtained should then be corrected by subtracting the Doppler ambiguity which has been proved to be independent of the frequency. Finally, the corrected values should be multiplied by the theoretical inverse transfer function (George and Lumley, 1973 p. 332) to determine the true spectrum (see also Wang (1973)).

In summary, LDA has been used successfully to measure the laminar and the turbulent flows of liquid or gas. It has been found suitable for measuring speeds up to 305 meter per second and even higher, and has been proved accurate enough to measure the fluid velocity in laminar flow. In the measurement of turbulent intensity however, it is difficult to eliminate the ambiguity broadening which is attributed to the finite life time of the Doppler signal. The Doppler ambiguity imposes limitations to the measurement of the turbulent spectrum, too.

So far, we have not considered the various LDA configurations.

The optical arrangements can be classified into two categories:

(1) The reference beam mode. The first LDA was set up in this mode (Yeh and Cummins (1964)). The principle of its operation is described briefly as follows (see also the Appendix). A laser beam is directed to the flow. Light scattered by particles flowing with the fluid is received by a photo-detector. According to the Doppler principle, the frequency of the scattered light changed proportionally

to the velocity of the scatterer. The shift in frequency can be measured by mixing the scattered light beam with the unshifted reference beam. The photodetector signal then contains a beat frequency equal to the Doppler shift frequency. Abbiss, Chubb and Pike (1974) noted that if the average number of scattering particles present at any instant in the scattering volume is significantly larger than unity, this mode is preferable. This optical mode is susceptible to mechanical disturbance, and the aligning procedure is quite complicated relative to aligning the real fringe mode.

(2) The real fringe mode. This mode was first suggested by Rudd (1969). He analysed the LDA system of Goldstein and Kreid (1967) and the system of Yeh and Cummins (1964) by using an optical filter model. Instead of interpreting the frequency shift in terms of the Doppler effect, he interpreted the observed signals in terms of a particle crossing a set of fringes, real in Goldstein and Kreid's case and virtual in Yeh and Cummins' case. Brayton et al (1973) indicated that the real fringe system is easier to align and less sensitive to mechanical disturbance. The best signal-to-noise ratio is obtained when the intensities of the two intersecting laser beams are equal.

Whether or not the interference fringe model is equivalent to the Doppler shift model is still open to controversy. In their analysis, Adrian and Goldstein (1971) noted that the interference fringe model and the Doppler shift model are not equivalent ways of looking at the same

thing as evidenced by the simultaneous appearance of heterodyne current and fringe current in their equation for total photocurrent.

Instead of considering a particle crossing a set of fringe, Wang (1971) thought of the mixing of light scattered by a similar particle but from both incident light beams. His analysis (Wang 1972) led him to conclude that the best SNR was obtained when the intensities of both incident beams were equal. Since the beat signal obtained was independent of the direction of observation, he suggested that light scattered from the probe volume might be collected through an arbitrary large solid angle to increase SNR. Meanwhile, Lading (1971) indicated that the best SNR was reached when the photodetector was placed at the focus of the collecting lens. He also indicated that the beat frequency was independent of the direction of detection. Wang and Snyder (1974) verified experimentally that when the concentration of the scattering particles was low, the real fringe mode gave considerably better SNR than did the reference beam mode.

As we have mentioned previously, Foreman et al (1966) suggested that using the frequency shifting technique would improve the capability of LDA. Stevenson (1970) first used a rotating radial diffraction grating in LDA measurements, pointing out the following advantages:

(1) it would allow one to discriminate the direction of velocity;

(2) it would simplify the problems encountered in

measuring low velocities;

(3) it would allow one to match the heterodyne frequency to the characteristics of the signal processing equipment.

Logan (1972) employed a rotating radial diffraction grating to measure the streamwise and transverse intensity components as well as the Reynolds stress. He used the LDA in the reference beam mode with the zero-order beam as the reference beam.

Denham, Briard and Patrick (1975) employed an ultrasonic cell (described by Cummin et al, 1963) to measure the mean velocity and the turbulent intensity in a turbulent flow in a pipe of bore diameter 2.54 cm. Their results were not reported in the paper however, but they claimed that, by using their modified LDA with the ultrasonic cell, their results in the newtonian fluid showed good agreement with the hot-wire results of Laufer (1954).

When they were measuring the fluctuation of the velocity very near to zero, a difficulty arose, for the Doppler signal obtained appeared to be dominated by a strong unwanted noise at the shifted frequency. In other words, the spectrum of this signal contained an unwanted component superimposed on the normal spectrum. They explained that this could be due to either the influence of the transmitted radio signal (8MHz) from the power-supply, and/or the mixing of the reference beam with light scattered from the walls of the cell.

Because of the influence of the unwanted noise, a

tracking filter could not be used normally. They suggested using a spectrum analyser to measure the intensity of the fluctuation.

Our LDA for the streamwise velocity measurement

For the streamwise velocity measurement, we have used the LDA in the real fringe mode. This is described in the following paragraphs; its principles are described in the Appendix. The following list are the components of the streamwise LDA.

Table 3-I Components of LDA Used in Present Work

Component	Model
Laser	Spectral Physics, Model 120, He-Ne
Beam splitter	Malvern
Photo-multiplier	DISA 55L12
PM tube Power Supply	DISA 55L15
Tracking Filter	Model HF & LF, Communications and Electronics Ltd
Digital Voltmeter	DISA 55D31
Rms meter	DISA 55D35
Signal Conditioner	DISA 55D26
Tape Recorder	RACAL 4D

The LDA is composed of a 5 mW laser, a beam splitter, 2 lenses and a photo-multiplier. A tracking filter was used to convert the Doppler frequency signals to the varying voltage output, enabling us to measure the turbulent fluctuating velocity.

Figure 3.1a is a schematic diagram of the LDA system.

Table 3-I lists the components of the LDA. The laser has a Gaussian intensity profile of wavelenth 6328 Å. Its diameter at $1/e^2$ points is 0.65 mm according to the manufacturer's manual. The beam splitter can be mounted on the head of the Spectral Physics laser. The parallelness and separation of the split beams can be adjusted. The intensity of one of them can be varied, too. We have kept their separation equal to 1.84 cm and their intensities equal. The biconvex focussing lens has a focal length 5 cm, with a diameter 6.3 cm. The collecting lens is mounted on the front of the photomultiplier tube, with a focal length 12 cm. The photomultiplier has a frequency response of 25 Mhz at 2 KV.

The tracking filter is composed of three separated units: (1) the main part of the circuit, (2) the plug-in filter unit, and (3) the wide-band preamplifier. It can be used as a spectrum analyser. In doing so, the tracker must be in a "sweep" condition. It is an autodyne frequency tracker with a tracking rate proportional to the band-width of the plug-in filter and to the integrator time constant. However, experience tells that if one wants to measure high frequency fluctuations the integrator time constant must be short. This will increase the likelihood of 'dropping out' - losing lock - of the tracker unless the band-width of the plug-in filter is increased correspondingly.

The Digital Voltmeter has a selection of several ranges from the smallest 0 - 0.3 V to the largest 0 - 200 V with an internal time constant selector. We have selected

the range 0 - 10 V for our experiments; therefore the DVM can resolve a voltage up to 0.01 volt. The Rms meter also has an internal time constant selector and it can resolve up to 1 mV in the range we used during our experiments. The signal conditioner consists of an amplifier, and the high and low-pass filters. The tape recorder has 4 channels and a channel particularly for audio recording. Three channels are FM and the remaining one is an AM channel. Each FM channel has a frequency response up to 20 Khz at a speed of 60 inches per second. The advantage of using the FM channels is their high fidelity compared with the AM channel. On the other hand, the advantage of using the AM channel is its high frequency response, 300 Khz at the speed of 60 inches per second.

All the optical components and the PM tube were mounted on a bench resting on a number of rollers which were in turn mounted on a steel plate. Eight screw feet, supporting the steel plate on the table, were used to level the plate. The optical bench was adjusted to make the paths of light lie in a horizontal plane containing the axis of the pipe. In doing so, firstly we mounted the laser on the bench and adjusted the orientation and the level of the laser until the beam was horizontal and normal to the pipe axis. For convenience, the beam had been put directly above the axis of the optical bench in order to use the traveller units more effectively.

The beam splitter was then mounted on the laser. The split beams were aligned by adjusting the splitter until

they were parallel to each other with a separation 1.84 cm. Automatically, two beams should lie in the horizontal plane containing the pipe axis. The collimated beams were focussed by the lens of focal length 5 cm. The lens were mounted on the bench. It could be adjusted vertically and horizontally to set its optical axis parallel to and midway between the collimated beams. The beams should intersect at the focus of the lens.

Without the pipe in position, we obtained the angle of the intersection of the beams by measuring the base of an isosceles triangle formed by joining the following three points: the point of intersection, and two points where the two diverging beams struck the wall of the laboratory. This method was found to be quite accurate as the triangle was large. The angle was found to be 10.43^{o}. This angle of intersection gave an ellipsoidal probe volume of dimensions 0.06 mm x 0.34 mm x 0.06 mm, the longest dimension (0.34 mm) being in the radial direction of the pipe. Then, the pipe was fixed on the table. The focussing lens was then moving back and forth along the optical bench until its position made the focus (probe volume) on the internal wall of the pipe. This was done by gradually moving the lens traveller to make the two flare dots coincide.

A micrometer was fixed subsequently. It was mounted on an angle-support which was fixed on the steel plate. The head of the micrometer was adjusted to attach on the surface of the block moving with the optical bench. The micrometer reading defining the internal wall of the pipe

was recorded. Then we proceeded to traverse the probe volume to the other side of the internal wall and the micrometer reading was recorded. This reading along with the previous one gave the diameter of the pipe to be 19.3 mm. Compared to the actual diameter (19.5 mm) of the pipe (measured by callipers), the difference was 1%.

The PM tube was mounted on the bench, on the other side of the pipe, with the collecting lens of focal length 12 cm mounted on its front. The lens brought the beams focussing into the pin hole of the PM tube. This completed the alignment of the LDA. In order to reduce the background noise, when we were actually measuring the velocity, we prevented the beams from striking directly on the PM tube by using masks, as suggested by Durrani and Greated (1975).

Signals were detected by the PM tube and were fed, in turn, to the wide-band preamplifier and then to the tracker. The voltage output of the tracker was proportional to the input frequency of the Doppler signal. The calibration of the tracker was done according to the instructions of the suppliers. After calibration, we obtained the formula:-

$$\text{'Khz'} = 333.33\ \text{'VOLT'}$$

where 'Khz' was the Doppler frequency in Khz and 'VOLT' was the voltage output in volt. Combining this with the formula

$$\text{'}\frac{U}{\text{Khz}}\text{'} = \frac{\lambda}{2 \sin \frac{\theta}{2}} = 0.174 \ (\text{cm/sec/Khz})$$

where U was the velocity of the scattering particle, λ

the wavelength of laser light and θ the angle of the intersection of the beams, we obtained

$$U\ (\mathrm{cm/sec}) = 58\ {}'\mathrm{VOLT}'\ .$$

The output signals from the tracker were recorded, through the signal conditioner, on magnetic tapes by the tape recorder.

The principle of the tracker is stated briefly as follows. The instantaneous Doppler signal is split into two orthogonal components feeding in two separated but identical branches. The orthogonal components are generated by mixing the instantaneous signal with 90^{o} phase shifted outputs of the Voltage-Controlled Oscillator which in turn controlled by the voltage output of the tracker. Each of the branches contains a low-pass filter, and a differentiator. Both branches are linked so as to perform the operation to give

$$V_o(t) = Z_1(t)\dot{Z}_2(t) - \dot{Z}_1(t)Z_2(t)\ ,$$

where $Z_1(t)$ and $Z_2(t)$ are outputs from the low-pass filters of branches 1 and 2 respectively, and $V_o(t)$ is the output signal. The dot represents a differentiation with respect to t. This output signal is led back into the VCO input completing a feedback loop. In terms of instantaneous frequency of the Doppler signal the analogue output is found to be

$$V_o(t) = \frac{Z_1^2(t) + Z_2^2(t)}{1 + K[Z_1^2(t) + Z_2^2(t)]}\omega_i(t) \simeq \frac{\omega_i(t)}{K}$$

for large K, where $\omega_i(t)$ is the instantaneous frequency and K, the oscillator control constant. Therefore the

output signal faithfully follows the instantaneous input Doppler signal.

Experimental procedure and the newtonian result

We shall now introduce the experimental procedure and present the results for newtonian fluid. The experimental rig has been introduced in the previous chapter. Milk has been used to seed the flow of water.

Doing the experiment, we considered a number of parameters to be measured (see sheet 1, next page). The sheet was used to record experimental data systematically. During the experiment, we followed the procedure and recorded the appropriate readings. Each sheet was for one run only. After that, calculations were made according to the formulae given, by use of a pocket calculator. Reynolds number, friction factor and shear velocity were parameters used to specify the flow. On the table, y (in mm) denotes the micrometer reading, representing the location of the probe volume. VOLT (in V) and Rms (in mV) are the mean and root-mean-square values of the fluctuating tracker output respectively. The parameters y^+, U^+, y/R and u^+ are obtained according to the following formulae:

$$y^+ = 1.33\ u^*(y_w - y)/(10\nu)\ ,$$

where y_w (mm) is the micrometer reading representing the internal pipe wall and ν the kinematic viscosity (cm^2/sec) at the temperature Temp (in ^oC)

$$U^+ = 58\ VOLT/u^*\ ,$$

$$y/R = 1.33\ (y_w - y)/19.5\ ,$$

Experiment: _____ Date: _____

Fluid: _____/ Conc. = _____(ppm) Temp. = _____(^{o}C)

Flow rate: H_1 = _____(cm) , H_2 = _____(cm) ,

ΔT = _____(sec)

Pressure drop: h_1 = _____(cm) , h_2 = _____(cm) ,

Calculations:

$V = 24.7\ (H_2 - H_1)/\Delta T$ = _____(m/s),

$Re = 195\ V/\nu$ = _____ ,

$P = 56.92\ (h_2 - h_1)$ = _____ (N/m^2)

$f = 0.065\ P/(1000\ V^2)$ = _____,

$u^* = 0.28\ P$ = _____(cm/s)

Tape = _____ Speed = _____

y	VOLT	Rms	Footage Counter		Ch.	y^+	U^+	y/R	u/u^*

Sheet 1

and

$$u/u^* = 58\ Rms/u^* \quad .$$

Mean velocity profiles and turbulent intensity distributions were measured at different Reynolds numbers between 10,000 and 50,000, in water. The mean velocity profiles are shown in Figure 3.2, showing good agreement with the equation verified by Nikurase and Reichardt (Schlichting, 1955). When $y^+ \simeq 250$ at low Reynolds number, the data start to separate from the line showing a wake region behaviour (Ramu and Tullis (1976), Rabie (1978)). Figure 3.3 shows that the streamwise turbulent intensity lay between the conventional results of Laufer (1954) and the more recent result of Lawn (1971). Our results also agreed with the LDA results in a 2.54 cm pipe of Rabie (1978) which agreed with Lawn's quite well.

The LDA for the transverse velocity measurement

Figure 3.4a is the schematic diagram of the optical system for the transverse measurement. Figure 3.4b is the data acquisition system; the power spectrum of the Doppler signal was to be found. The half width of the resultant spectrum was computed to give the turbulent intensity in the transverse direction.

In the figure, the Laser is a Spectral Physics (Model 120) 5 mW He-Ne laser, as introduced in the previous section. Its characteristics are exactly the same as that used in the streamwise measurements.

55L01 Optical Unit is a DISA beam splitter, composed of a biprism, an adjustable surface mirror and two glass

wedge plates (with wedge angles of 3^{o}). All the components are in one housing. The principle of the splitter was described in the manual given by DISA. With this optical unit, beam separation can be varied between 18 mm and 54 mm, the presence of the wedge plates providing a means of adjustment for perfect beam-intersection. A lens can be mounted on the housing to form one unit. Its focal length can be selected as 13 cm, 30 cm or 60 cm. The Flow Direction Adapter is used and mounted on the beam splitter forming one unit. It contains two optical Bragg cells parallel to each other and fixed in position allowing a beam separation of 5 cm. The angle of incidence of the laser beams with respect to the Bragg cells may be varied by adjusting the angular position of the cells through the holes above the BNC connectors using the Allen screw driver provided.

The following information about the operation of the Bragg cell is provided by the DISA manual for the Flow Adapter. The Bragg cells consist of a block of acoustic-optic material. Along one side of each of these blocks is bonded a series of piezo-electric transducers. By applying RF-voltage across the transducers a train of plane acoustic waves is created in the material moving through the cell with the velocity of sound. The waves are absorbed by a damping material on arrival to the other side of the block. The acoustic wave fronts in the cell constitute a moving, thick optical grating, which diffracts the light passing through the cell. The diffracted light is shifted in frequency by the frequency of the sound waves. Both Bragg

cells operate at a high frequency, but with a fixed difference of f_o. Thus the two beams leaving the cells have a frequency difference of f_o.

The Bragg cells are driven by two identical RF printed circuits and a common 12 V power supply.

For proper alignment, two conditions must be fulfilled: (1) The two Bragg cells must be adjusted to the correct angle, and (2) the two laser beams must intersect in their common focal volume (the probe volume).

In figure 3.4a the direction of the mean flow is perpendicular to the plane of the figure which contains the light paths of the LDA. When the converging beams intersect at a point inside the pipe, the intersecting angle will be changed nonlinearly as a function of displacement of the probe volume. This nonlinear relationship imposes difficulties in determining the half angle and the location of the probe volume from the wall. Nevertheless, we solved this problem and a detailed description of the solution will be introduced later.

The converging lens chosen has a focal length of 30 cm, mounted on the front of the Bragg cell housing. The collecting lens has a focal length 13 cm, mounted on a lens carrier.

The circuit of the home-made photodiode consisted of three transistors and a photo-diode, with frequency response about 500 Khz; it required a D.C. power supply 9 volts. The signal with frequency above 500 Khz appeared to be attenuated and even disappeared when the frequency reached

about 800 Khz. For satisfactory operation of the photo-diode detector, we have selected a frequency shift of 250 Khz by setting the selector available in the DISA flow adapter. Moreover, we knew that the AM channel of the recorder could record a signal of frequency only up to a maximum of 300 Khz at a speed of 60 inches per second. Our choice of the 250 Khz frequency shift was thus inevitable.

The alignment of the optical system was not an easy task. The procedure was to make the plane containing the light paths, with the pipe axis normal to it. Like the streamwise system, all the optical components were mounted on a triangular optical bench resting on a steel plate which in turn was supported by eight screw feet. At first, laser and the beam splitter were fixed on the bench. The laser beam was split by the beam splitter into two. The orientation of the laser had then to be adjusted to make one of the beam lie in the vertical plane mentioned above. The glass wedge plates were then rotated to obtain the beams parallel to each other. If the beam splitter stood perpendicular to the horizontal plane (as shown in figure 3.4a), the two collimated beams should automatically be horizontal and in the same vertical plane. Then, the separation of the beams was adjusted by moving the surface mirror. A separation of 5 cm was required. Then the sliding block on which all the optical components were mounted in the beam splitter housing, was moved up and down to adjust each beam to lie at 2.5 cm from the optical axis

of the splitter. Finally the housing as a shole was shifted vertically up or down so as to ensure that its optical axis intersected the pipe axis. This could be done by two ways: (1) shifting the steel plate, or (2) adjusting the vertical sliding knobs of the carriers supporting the laser and the optical unit.

Afterward, we carefully dismantled the front cover of the beam splitter and then fixed the Bragg cell flow adapter on it (instructions were given by DISA in the manual for the Bragg cell), mounted the front cover of the beam splitter on the front of the Bragg cell unit, and then fixed the combined unit on the optical bench again. With the light beams emerging from the Bragg cells, we adjusted the Bragg angles by using the provided Allen screw driver until two positive frequency shift beams appeared to be brightest.

The 30 cm lens was then mounted on the front of the flow adapter, converging the beams to form a probe volume in the pipe.

In order to make sure of the formation of the fringe pattern, an objective was used to projected an enlarged fringe pattern on the wall. The fringe pattern was formed by the interference of the two intersecting zero-order beams. The intersection of the two first-order beams did not give a visible fringe pattern since the pattern was moving. The alignment of the optical units on the illuminating side was thus completed.

On the collecting side, the lens and the photo-diode

detector were mounted on the bench, the lens being used to collect the scattered light from the scattering volume to the detector.

As has been mentioned above, the displacement of the probe volume and the angle of intersection of the beams are related to one another non-linearly due to the spherical nature of the pipe wall surfaces. One of the converging beams, entering into the external surface of the pipe with a certain angle to the normal, is deflected according to Snell's law and then deflected again by the internal interface. The other beam undergoes the same fate, forming a light path similar to the mirror image of the path of the first. The two beams meet at a point in the pipe, forming an angle, $2\theta'$, different from that measured in air. The location of the intersecting point (location of the probe volume) is specified by the distance, s', from the internal wall of the pipe, s' being given by the formula (derived in the Appendix):

$$s' = (s - r + R) \frac{\cos\ (\theta' - \frac{\delta'}{2})\ \sin\ \theta}{\cos\ (\theta - \frac{\delta'}{2})\ \sin\ \theta'}$$

where r and R are the outer and inner radii of the pipe, respectively. s, θ, δ' and θ' are variables relating to one another implicitly. s' and θ' are the two parameters required.

In the Appendix, we show that they change nonlinearly with x which is the displacement of the optical system in air. Since the relationship between variables is not explicit, we cannot write down a formula between s' and x

or θ' and x explicitly; they are related by six equations altogether. We have used a graphical method to obtain a curve relating θ' and s', s' being calculated by the use of the lens formulae; this is also introduced in the Appendix. The curve relating θ' and s' is shown in figure 3.5. It was calibrated once for all the experimental work.

Experimental procedure for measuring transverse component

The flow parameters should be recorded in the same way as in the streamwise measurement. We measured $x = y_w - y$, with y and y_w being the micrometer readings when the probe volume was at the measuring point and on the outer surface of the pipe, respectively, we then calculated s' by using the following formula,

$$s' = \cfrac{1}{0.013 - \cfrac{1}{2.62 - \cfrac{1.33}{0.0394 - \frac{1}{x}}}}$$

The Doppler signal with beat frequency fluctuating around 250 Khz was fed through the signal conditioner to the AM channel of the recorder at speed 60 inches per second. This procedure had to be repeated to complete the measurements at different points across the pipe.

The recorded signals were then played back at a speed of $3\frac{3}{4}$ inches per second to reduce the frequencies of the output signals by a factor of 16. In our case, the corresponding play-back frequency of interest was around 15.6 Khz.

The signals were then fed to the first channel of the Analog to Digital converter (MIDAS), digitized at the

sampling rate of 40,000 samples per second. The digitized data were stored in the PDP8/m and the extended memory (FABRI-TEK Model 8/E Add-On Memory System) with a capacity of 24K (24,576) 12-bit words and subsequently transferred to EMAS. Spectrum analysis was done by running a program (MASTO) on EMAS.

Figure 3.6 shows a typical spectrum with a spike superimposed on the spectral curve. The spike seems to be unwanted noise, probably arising from the mixing of the scattered light from both beams by the wall of the pipe. Denham, Briad and Patrick (1975) came across the same problem when they were applying their instrument to the measurements of water flow. They used one ultrasonic cell as a frequency shifter with the shifting frequency 8 Mhz. They found a 'spike-like' noise dominating the signal and imposing difficulty in measuring fluctuating velocities with zero mean. They attributed the unwanted signal to the mixing of the reference beam with light scattered by the walls of the ultrasonic cell. We agree with this explanation, yet think that light scattered by the pipe walls contribute more to this spurious noise.

A tracking filter could not be used in such case, for the dominating component would prevent the tracker from tracking the fluctuating velocity. This was the reason why we chose spectrum analysis.

The turbulent intensity was computed from the half width of the Doppler spectrum. Using this method, we have obtained results of turbulent intensity distribution shown

in figure 3.7, showing that they scattered around the results of Laufer (1954). The scatter was rather large, especially in the region near the centre line. It can be explained as follows: in this region, the particle mean velocity was relatively high while the transverse turbulent intensity was relatively low. This may cause a relatively small signal-to-noise ratio.

In the near wall region, the data at Reynolds numbers from 12,000 to 28,000 showed a good collapse, suggesting that the performance of the LDA was well, at least in this region. We have used this system to measure the transverse intensity in the drag reducing flow.

It had an angle of intersection equal to 9.52^{o} in air. In the pipe, the angle was becoming smaller as the probe volume was moving towards the wall. The size of the probe volume was also varying due to the variation of the intersection angle. It is also possible that the shape of the probe volume was distorted due to spherical aberration.

The Digital Sampling System

Our digital sampling system consisted of an Analog-to-Digital converter, a PDP8/m mini-computer, an extended memory unit, a teletype and a MODEM. This system has been introduced by Dickson (1978). His research report has full details of specification of various units and the operating procedures in using it.

The A-D converter is one of the two facilities of MIDAS - Multiple Input Data Acquisition System, with sixteen input channels connected to the PDP8/m mini-computer. An

external trigger source is necessary to operate MIDAS as a A-D converter. We used a function generator for this purpose. The trigger pulses should have a low voltage level in the range 0 V and +0.6 V and a high level between +2.4 V and +5.0 V. In using only one channel, the highest sampling rate MIDAS can achieve is 110 Khz. This will be reduced if more channels were used simultaneously.

The relationship between the input analog signal and the output digital data was:

Input Voltage	Digital Data	
(Volts)	(Octal)	(Decimal)
-10 V	7777	4095
0	3777	2047
+10 V	0	0

Digitization is carried out to 12-bit precision, therefore, the root-mean-square quantizing error is 2.82 mV (Allan, 1976).

The PDP8/m mini-computer is produced by the Digital Equipment Corporation (DEC). It is a general purpose computer, using 12-bit word to represent one data, with storage size 8K (8192) bytes. An extended core memory system (FABRI-TEK Model 8/E Add-On Memory System) is connected to the PDP8, increasing the total memory size to 32K 12-bit words.

The teletype was connected to the PDP8 as a peripheral Input/Output unit. It contained a binary paper tape reader to load paper-tape programmes. The binary tape was prepared by the following procedure: the user should edit

a nmonic source program by using the EMAS Editor of ERCC - Edinburgh Regional Computing Centre and assemble the program by using the PAL8 routine available in EMAS. The assembled program can then be typed on a binary paper tape.

The relevant PDP8 program we used to transfer data is named TRANS6FD with an initializing address (400_8). After starting the program, one can communicate with the large computer machine in ERCC through a MODEM and a telephone line by using the teletype.

To transfer data, a program (ENTER) has to be run in EMAS, sending a 'request' to PDP8, asking for information. One should in response push Control G keys to shift the communication link from EMAS - teletype to EMAS - PDP8. Consequently, TRANS6FD 'talks' with ENTER, with data being sent and received.

Six fields of data are transferred in one run, spending 58 seconds of CPU time. Problems often arose in transferring data because of the maximum CPU time limit 30 sec set by EMAS during busy periods. In this case, the ENTER often stopped itself without completing the copying all the six fields of data. These problems disappeared when working at night or early in the morning.

To sample the turbulent signal of the highest characteristic frequency 5 Khz, a sampling rate of 10 Khz was used in order to meet the requirement of the sampling theorem. A signal conditioner was used as a band-pass filter, with the cut-off frequency selected at 5 Khz, to filter the turbulent signal before digitizing.

To sample the Doppler signals for the transverse measurements, we were supposed to use a sampling rate of 500 Khz, for the maximum characteristic frequency of them was 250 Khz as mentioned before. However, it was not permissible to do so because MIDAS could only sample data at a maximum rate of 110 Khz (Dickson, 1978). This problem was overcome by replaying the AM channel tape at a lower speed to get a reduction of frequency components. We chose a reduction factor 16, reducing the frequency 250 Khz to 15.625 Khz, thus deciding to use a sampling rate 40 Khz.

Digital Spectral Analysis

Prior to the spectral analysis, the data format of the received file (from PDP8) had to be changed to suit the program JAKPAC. The input data to JAKPAC had to be stored in a sequential file and of format short integer. Improper transformation of the data format would create spurious results.

A program MODIF was used for this purpose. It has been compiled and stored as a routine in order to simplify the procedure of performing Fourier analysis.

JAKPAC is in fact a sub-program containing several routines to accomplish Fourier analysis. One of them is the FFT algorithm (fast-fourier-transform) called to do discrete Fourier transform of the input data in an efficient way. Others are smoothing routines. The frequency smoothing routines are used to reduce leakage. We have chosen the Hanning smooth routine which provides higher leakage suppression (Allan, 1976).

JAKPAC was developed by Allan. A separate program, MASTER, was used by him to simplify the operations, making the system more flexible. Eight parameters could be controlled in the MASTER program. Each of these had to be assigned a suitable value before running MASTER; they were:

L : the Record Length

SKIP : data skipping

SF : sampling rate

P : number of data points is equal to 2^P

SMCODE : smoothing code, 2 for Hanning smoothing

REDFACT : A fixed frequency average is performed using 'REDFACT' points per spectral estimate.

SEG : number of segments

MOV : number of points over which the final moving average is performed

The assigned values for these parameters were as shown in the list of MASTER program in figure 3.8.

Test of the Digital System

A sinusoidal wave has been digitized by MIDAS with sampling rate higher than twice its frequency and stored in PDP8/m. After transferring the data to EMAS, MASTER was run to get a spectrum shown in figure 3.9. It was a spike at the frequency of the input wave, ensuring that the digital system was perfectly suitable for harmonic analysis.

Using this digital system, we have also obtained results for the newtonian fluid as shown in figures 4.10

and 4.11. At higher Reynolds numbers, the spectra agreed quite well with that of Lawn (1971). At lower Reynolds number, however, the agreement was not so good, probably due to the strong viscous effect at low Reynolds number.

For the spectral analysis of the Doppler signal for the transverse measurements, convincing spectra could be obtained by using the digital system, but only for low speed flows. A typical spectrum for the turbulent flow was shown in figure 3.6. In the figure, a spurious spike superimposed on the normal spectrum is displayed. This has been explained previously. The half-width of the normal spectrum centred at 250 Khz is the measure of the transverse intensity. The distribution of the transverse intensity across the pipe has been introduced previously (Fig. 3.7). The results were agreeable.

Chapter 4 Results and Discussion

Seeding

Doppler signals have been examined to determine the influence of the fibres on the signal. We had in mind that this would shed some light on the problem of finding out how much the fibres contributed to the Doppler signal. The examination was done by feeding the band-pass filtered photocurrent to a storage oscilloscope. The signal traces were then photographed with a Polaroid camera.

The effect of the concentration of milk on the Doppler signal is shown in figure 4.1. It reveals that 200 ppm milk gives more bursts than 100 ppm does. Without milk, we can see no burst but the background noise.

Also shown in figure 4.1 is the signal trace for 0.5% Aerosol OT solution without any other seeding. We cannot see a dominant isolated burst in this case as we did for the milk. Instead, the trace appears to arise from the modulation of overlapping bursts, implying that comparatively more scattering particles are present in the Aerosol OT solution. The nature of these particles is not known exactly. However, we have evidence to show that these scatterers are faithful tracers like the milk. This was shown by comparing the velocity signals from the Aerosol OT solution with those from pure water using milk as seeding (Figs. from 4.8 to 4.12). We shall discuss these later.

Figure 4.2 compares the signal traces for the 300 ppm fibre suspension with different milk concentrations. Their appearances on the oscilloscope screen are very similar,

even for the case when 150 ppm polymer was present. This, taken with the previous points, implies that the LDA signal was already dominated by particles of surfactant and that the addition of milk particles probably had no significant effect.

Figure 4.3 shows the mean velocity profiles measured by LDA in the fibre system with different concentrations of milk, namely, 0, 100 and 200 ppm. The solid symbols are for the first passes of the suspensions. The hollow symbols are for the second passes. They were plotted on a semi-logarithmic diagram in reduced form. Both sets of data collapse very well, showing no influence of milk on the mean velocity measurements. The discrepancy for the case of no milk at the second pass may be due to the lower drag reduction of this run.

As for the streamwise intensity distributions shown in figure 4.4, the discrepancies cannot be ignored. Nevertheless, as we look closer into the figure, we should notice a familiar effect observed in a polymer drag reducing system. Clearly, for the second passes, the turbulent intensity level is proportional to drag reduction. So, the discrepancies may be due to a drag reduction effect. In other words, they are not the effect associated with the milk addition.

For the cases of 0 and 100 ppm milk at the first passes, the data collapse rather well. There is a discrepancy, however, between these and that of the 200 ppm milk, as shown in the figure. Similarly, it may be attributed to

either the drag reduction effect or the lower Reynolds number of the run. The presence of milk does not alter the observations.

The energy spectra of the turbulent motions are shown in figure 4.5 for the first passes. These are plotted on a log-log diagram in a normalized form according to Lawn (1971). The three spectra collapse quite well. Only at high wave-number range, does the spectrum of the case of no milk appear to be white. This will be discussed in more details later in the chapter. The spectra of the third passes, figure 4.6, collapse very well, showing no milk influence on these measurements.

Comparing the Doppler signal traces of the fibre suspension with those of the Aerosol OT solution alone (Figs 1 and 2), we see no special difference in their features. We thus assume that the fibres do not contribute much to the Doppler signal.

This may be seen to be reasonable as follows: for the individual fibres in the turbulent flow, we consider two possible extreme cases. Firstly, suppose a fibre is stretched and aligns in the flow direction. Because of its extreme thinness (0.05 μm diameter), the scattering efficiency of it is very small. It is 0.05 according to the data tabulated by Wickramasingle (1971). It is much smaller than the value for a spherical particle of milk (Qsca = 4). However, the fibre has a larger cross-sectional area exposed in the probe volume than the milk has. So, it is likely that the light energy scattered by such a

cylindrical particle of fibre is still large. Nevertheless, if we imagine an elongated rigid fibre of this size moving across the probe volume with its axis perpendicular to the fringe planes, it is possible that its motion across the fringe will not give distinguishable flashes. Most of the scattering light will contribute only to the DC part of the signal.

Secondly, suppose a fibre is squeezed and becomes a tight ball. Its diameter should be about 2 μm. It is the appropriate size for light scattering. If such balls do exist in the flow, the question will arise: do these balls faithfully follow the flow? Using Tchen's equation (Hinze, 1959), we have worked out that they are able to follow the flow up to a frequency over 10 KHz. This frequency is twice the cut-off frequency we used in the spectral analysis of the turbulent signal.

Figure 4.7 shows the spectra of the photo-current measured in the laminar flows of the fibre suspension and its surfactant solution alone. They were obtained in a preliminary experiment using LDA, high pass filter, tape recorder and the computer system. We had used a header tank to get a laminar flow in a small capillary tube of 5 mm in diameter. Using the LDA, we obtained and recorded the photo-current for the clear water, the Aerosol OT solution and the fibre suspension successively. No signal was detected in the clear water case. The spectra are shown in figure 4.7 for the surfactant solution and the fibre suspension. One can see that they are quite similar,

indicating that the fibre additive does not contribute much to the signal in this frequency range. For the fibre suspension, the signal has only one Doppler peak, showing that no second component of different velocity is present in the photo-current. That is to say, in this frequency range, particles associated with the surfactant agent are the dominant scatterers. It is consistent with our former conclusion from the photo-current traces.

Discussion of the Results for the Aerosol OT Solution

We have shown that the particle of the surfactant were dominant light scatterers for LDA measurements in the 300 ppm fibre suspension. We also have mentioned that these scatterers were faithful tracers like the milk. Evidence is shown in figures 4.8 to 4.12, demonstrating that these particles were indeed giving results comparable to those of water. They are representative of the results we have obtained in the Aerosol OT solution.

Shown in figure 4.8 are the mean velocity profiles of the Aerosol OT solution at two different Reynolds numbers, namely, 1.5×10^4 and 4.0×10^4. The continuous curves (the curved and straight lines) represent the universal mean velocity profile in newtonian fluid. They are given by the equations $U^+ = y^+$ and $U^+ = 2.5 \text{ Ln } y^+ + 5.5$, respectively. For the latter, we have shown in the previous chapter that mean velocity measurements in water agreed with the equation. The mean velocity in the surfactant solution lay around this newtonian line, showing no hydrodynamic effect (e.g. drag reduction) of the surfactant

solution nor particle effect (e.g. relative velocity between particle and fluid) of the scatterers. Moreover, in the figure, the good collapse of the data for two different Reynolds numbers shows the Reynolds number similarity in the system. As in figure 4.9, the distributions of the streamwise fluctuating velocity in the solution across the pipe show the Reynolds number similarity as well, though of lower intensity than in water.

The decrease in intensities might possibly be due to either the particle effect or the hydrodynamic effect. However, from the Reynolds number similarity, the former seems less likely. If particle effect comes into influence, at least one of the particle characteristics should be included in normalizing the measurement. The hydrodynamic effect is also quite unlikely for we see no drag reduction in such system, the mean velocity profiles agreeing well with the newtonian results.

Furthermore, in figures 4.10 and 4.11, turbulence spectra in the surfactant solution were compared with those in water alone. They showed general agreement with each other. At higher Reynolds number, they even agreed with the result of Lawn (1971), especially in the inertial subrange. Shown in figure 4.12 are the auto-correlations of the solution and its solvent alone. They agreed with each other rather well. Along with the turbulent spectra, these showed that the particles followed not only the mean flow but also the turbulent motion.

In conclusion, there was no observation of non-

newtonian behaviour in the 0.5% Aerosol OT solution. The particles associated with it were satisfactory tracers of turbulent flow.

Results in Drag-reducing Flows

The results obtained in the 300 ppm fibre suspensions were obtained as follows: all these suspensions contained 0.5% Aerosol OT surfactant. Four Reynolds numbers were studied, namely, 9×10^3, 1.4×10^4, 3.2×10^4 and 5.3×10^4. Each of them included a certain number of passes.

All measurements were made in the experimental rig which was introduced in detail in chapter two. The diameter of the pipe was 1.95 cm. A liquid-in-glass manometer was used to measure the pressure drop. The uncertainty of reading the displacement of the manometer fluid was $\pm \frac{1}{2}$ mm. The rectangular reservoir and a stop watch were used to measure the bulk flow rate. The total error was found to be less than $\pm$ 0.5%, depending on the length of the period of the pass. The sources of error mainly arose from the uncertainty of reading the side-glass meter.

An experimental 'pass' consisted of one run of the whole amount of working suspension through the apparatus at a fixed Reynolds number. Further 'passes' were further runs of the same fluid at the same Reynolds number. During each pass, LDA measurements were made and the velocity signals were recorded for digital analysis. The measuring instruments have been introduced in the previous chapters. Experimental results were always taken in steady conditions, avoiding the beginning and end of each pass. We shall

divide our results into three main groups.

Gross Flow

The studies involved pressure drop versus flow rate measurements. Presentations of results of these measurements on a friction factor versus Reynolds number diagram will introduce the phenomenon of drag reduction.

Figure 4.13 is a friction factor versus Reynolds number diagram, containing experimental points obtained in different runs of the suspensions. The continuous lines are the usual correlations for flows of water in laminar and turbulent regimes, given by the equations $f = 16/Re$ and $f = 0.316/Re^{0.25}$, respectively. Virk's maximum drag reduction asymptote for polymers is also drawn in the figure for reference.

As shown in the figure, the first two passes for the Reynolds numbers of 9.0×10^3 and 1.4×10^4 had friction factors lower than or equal to the limiting level given by Virk's asymptotic line. In later runs, the friction factor increased with increasing run number, showing degradation of the fibre suspension. For the other two Reynolds numbers (3.2×10^4 and 5.3×10^4), there was no such particular behaviour for runs 1 and 2. Instead, the suspension underwent a degradation with increasing run number from Pass 1.

The first passes at the lower two Reynolds numbers seemed to undergo a reverse action against degradation. The friction factors of the second passes in these two cases were lower than those of the first. This could be due

probably to the further mixing of the fluid during the first passes. It can be seen that the friction factor of Pass 2 at Reynolds number of 1.4×10^4 had a value substantially lower than Virk's limiting value.

Table 4-I summarizes the drag reduction percentage of each run for the four Reynolds numbers concerned. It includes results obtained in the polymer-fibre system. The mixture contained 300 ppm fibre dispersion and 150 ppm polymer (AP 30). The results generally showed a decline in drag-reducing effectiveness with increasing pass number, except for the polymer-fibre mixed system which does not show degradation for the first eight runs.

For fibre, at Reynolds number 9.0×10^3, the drag reduction did not decrease monotonically however. Instead, it went up and down with the pass number. Nonetheless, a general trend of declining drag-reducing effectiveness was observed. The drag reduction seemed to settle at a mean value 20%. The fluctuation of these data may be attributed to the fact that some fluid of the previous run remaining in the pressure vessel would have mixed with the present sample. This unwanted mixing has been minimized with the installation of the by-pass pipe.

A smoother decline in drag-reducing effectiveness was observed in the experiments for the Reynolds numbers of 1.4×10^4, 3.2×10^4 and 5.3×10^4, as shown in table 4-I. It can be seen that, in each case, the drag reduction was settling at a certain asymptotic value.

Returning to figure 4.13, we see that a curve joining

Table 4-I Drag Reduction (%) of 300 ppm Fibre Suspension

Pass \ Re	9×10^3	1.4×10^4		3.2×10^4	5.3×10^4
	fibre	fibre	polymer + fibre	fibre	fibre
1	63	69	50	71	54
2	63	76	58	62	52
3	58	56	61	58	47
4	44	55	58	58	46
5	32	51	59	56	49
6	43	48	62	51	43
7	34	48	59	50	43
8	26	44	60	50	41
9	30	44	51	47	40
10	22	42	45	46	40
11	-	42	43	-	-
12	23	39	41	-	-
13	25	38	40	-	-
14	17	-	-	-	-
15	20	-	-	-	-
16	18	-	-	-	-

Note: The concentration of the fibre suspensions is 300 ppm, the mixed system containing further 150 ppm polymer (AP 30).

the experimental points of the first passes exhibits a minimum and a tendency to the newtonian line. This is also true for the later passes. One may speculate that the drag-reducing effectiveness of the fibre might disappear completely if the Reynolds number were to be increased still higher. Passing the same amount of a fibre suspension (300 ppm) at different Reynolds numbers, Moyls and Sabersky (1978) observed the same behaviour.

In summary, we have obtained drag reduction higher than the limiting level calculated by Virk's asymptote. Asbestos fibre suspensions that we used were degradable drag-reducing fluid but the fibre-polymer mixture was not so apparant. The rate of degradation was dependent on Reynolds number. It appeared to have an asymptotic value for the drag reduction for each Reynolds number.

Turbulent Velocity Profiles

The turbulent fluctuating velocity has two statistical parameters, namely, the mean velocity and the fluctuating intensity (r.m.s.). The mean velocity U^+ (scaled with u^*) is plotted against the distance from the pipe wall y^+ (scaled with ν/u^*) on a semi-logarithmic diagram. The r.m.s. velocity u (divided by the friction velocity u^*) is plotted against distance from the pipe wall y (divided by the pipe radius R).

In the mean velocity diagrams, the newtonian profile for water consists of the viscous sublayer and the logarithmic core region, given by the equations of $U^+ = y^+$ and $U^+ = 2.5 \ln y^+ + 5.5$, respectively. The ultimate profile

is given by $U^+ = 11.7 \ln y^+ - 17.0$. This is the transformation of the maximum drag reduction asymptote, $1/\sqrt{f} = 9.52 \text{ Log } Re\sqrt{f} - 19.38$. For the newtonian profile, we have discussed it in the previous chapter.

In the r.m.s. velocity diagrams, water results are drawn for reference. They were almost independent of Reynolds number when normalized as suggested, ref. Laufer (1955) and Townsend (1956). Only for the results at Reynolds number of 9.0×10^3, did the intensity distribution tend to higher values.

The resolution of the probe volume can be expressed as $\sigma_y u^*/\nu$; the dimensionless expression of the probe volume size is simply used to represent the uncertainty in determining y^+ ($= yu^*/\nu$) in the mean velocity diagrams at different passes. For instance, all data points for Pass 2 of Reynolds number 9.0×10^3 have $\pm$ 3.2 uncertainty of measuring y^+ due to the probe volume size in the radial direction. We have not considered the uncertainty of the micrometer reading, for this is very little compared with that mentioned above. Being dependent on drag reduction, they are listed in table 4-II for each particular pass.

Figure 4.14 shows mean velocity profiles for the Reynolds number of 9.0×10^3. The amount of drag reduction appears as a parameter. It can be seen that the first two passes gave a drag reduction of 63% and that the corresponding mean velocity profiles lay beyond the Virk's asymptote for polymer solutions. In contrast, the results for later passes in the degraded suspensions were inside its limit

Table 4-II The Resolution of the Probe Volume $\sigma_y u^*/\nu$

Pass \ Re	9.0×10^3	1.4×10^4	3.2×10^4	5.3×10^4
1	6.4	10.6	20.5	36.8
2	6.4	9.3	20.9	37.6
3	6.8	12.3	20.4	38.6
4	8.1	12.1	21.2	39.3
5	9.2	13.0	22.2	38.1
6	8.7	13.5	22.7	40.5
7	9.2	13.3	23.5	41.0
8	9.2	13.2	23.5	41.4
9	8.9	13.2	24.6	39.0
10	9.1	13.7	24.3	-
11	-	13.8	-	-
12	9.1	-	-	-
13	9.2	-	-	-
14	9.4	-	-	-
15	9.2	-	-	-
16	9.4	-	-	-

(i.e. in the polymeric regime). Like results for polymers, they showed a trend to the newtonian results, as the amount of drag reduction decreased.

Figure 4.15 shows the r.m.s. velocity distributions for the same Reynolds number. Passes 1 and 2 showed a marked suppression of the streamwise fluctuating velocity, compared with the results for water. However, in later passes the intensity over most of the cross-section was increased above the newtonian result. Again, results in later passes were similar to those previously found in polymer solutions (Virk, 1975), showing a trend to the newtonian result with decreasing drag reduction.

Figure 4.16 shows the mean velocity profiles for the Reynolds number of 1.4×10^4. It can be seen that the results were almost similar to those at Reynolds number of 9.0×10^3. The percentage drag reduction of passes 1 and 2 were 69% and 76%, respectively. The corresponding profiles lay beyond the Virk's asymptote. In later passes, they lay in the polymeric regime, showing a trend to the newtonian result, like polymer results.

The corresponding intensity distributions are shown in figure 4.17. For clarity, only Passes 1 and 3 were plotted in the diagram. Pass 1 (and also Pass 2) showed a suppression of the streamwise turbulent intensity near the wall, compared to the newtonian values. The intensity was above the newtonian result in the central region however. The result of Pass 3 showed an increase of intensity above the water result. It behaves in the same way as in the results

for the Reynolds number of 9.0×10^3. A trend of decrease in intensity with decreasing drag reduction was also observed in later runs, but not shown in the figure.

Clearer results were obtained for this Reynolds number a year later with fibre suspensions containing 0, 100 and 200 ppm milk. These results were in fact used to determine the effect of milk on the optical signal; they have been already described. Figures 4.18 and 4.20 show the mean velocity profiles obtained with 100 ppm milk and without milk, respectively. Figures 4.19 and 4.21 are the corresponding intensity profiles. We have shown that milk did not affect the observation.

It is shown both in figures 4.18 and 4.20 that the mean velocity profiles in the first passes were partially beyond the Virk's asymptote. Later passes showed a polymeric trend again. As shown in figures 4.19 and 4.21, the turbulent intensity distributions of the first passes were of the same appearance as that in figure 4.17. However, in the central region, the intensity distributions were not plateau-like but declining with increasing y/R. These two figures show clearly that, after an enhancement of the turbulent intensity level, a polymeric trend appears in the later passes. It seems that we were observing a transition between two mechanisms (McComb and Chan, 1979). Such 'transitional behaviour' can also be observed in polymer-fibre system (McComb and Chan, 1980). Figure 4.22 shows the mean velocity profiles in this system at Reynolds number of 1.4×10^4. The concentration of the fibre was 300 ppm

in 0.5% Aerosol OT surfactant solution. Mixed with the suspension was 150 ppm polymer (AP 30).

It can be seen, along with table 4-I, that drag reduction was increasing in the first three passes. In later passes up to Pass 8, the drag reduction seemed not to be changed, showing that the mixed system was not susceptible to degradation. However, as shown in table 4-I, the fluid became degradable from Pass 9 onwards.

Figures 4.22 and 4.23 show that all the experimental points taken before the occurrence of degradation clustered together. It is true also for passes 4 to 7. The mean velocity data formed a straight line in the U^+ vs y^+ diagram, having a slope greater than that of the Virk's asymptote, however still lying in the polymer regime. The r.m.s. velocity data in figure 4.23 showed a marked suppression of the streamwise fluctuating velocity, compared with the results of water alone.

The experimental points measured in Pass 13, several runs after the occurrence of degradation, displayed a very different behaviour. The turbulent intensity in this pass increased over the water results, and the mean velocity profile tilt down towards the newtonian line.

Therefore, it is quite convincing that a transition between two mechanisms does exist. When the fibre is at maximum effectiveness, it behaves quite differently from polymers which produce comparable amounts of drag reduction. In particular, it makes the streamwise turbulence unusually low, even lower than those of the water alone. After degra-

dation, when the fibre is (presumably) smaller it seems to behave rather like a polymer of the same effectiveness. In particular, it enhances the streamwise turbulence.

One might be tempted to conclude that the undegraded fibres reduce drag by suppressing turbulence and making the flow 'more laminar'; such a conclusion would be wrong. Figure 4.24 shows that the absolute spanwise turbulent intensity (in cm/sec) for the undegraded suspension was greater than that for water alone, over a considerable portion across the pipe. In Pass 5, the spanwise intensity near the wall appeared to be less than that for water alone. Rudd (1972) has previously reported reduced spanwise intensities in polymer solutions near the wall.

Thus far, we have not mentioned velocity results for the Reynolds numbers of 3.2×10^4 and 5.3×10^4. They are shown in figures 4.25 to 4.28. Figure 4.25 shows the mean velocity profiles for the Reynolds number of 3.2×10^4. It can be seen that Pass 1 had a mean velocity profile close to the Virk's asymptote. As shown in the figure, the profiles of later runs showed a trend to newtonian result, as the drag reduction decreased.

The corresponding turbulent intensity distributions for this Reynolds number are shown in figure 4.26. We can see that the turbulent intensities of Pass 1 were substantially enhanced compared with results for water, showing a polymer-like effect. A polymeric trend was observed in later passes. In particular, the turbulent intensity decreased with decreasing drag reduction, approaching to

the newtonian result.

The mean velocity profile of Pass 1 at Reynolds number of 5.3×10^4 lay in the polymer regime, as shown in figure 4.27. The corresponding turbulent intensity was shown to be higher than that for water alone (Fig. 4.28). Again, later passes showed a trend towards the newtonian result, like the results for polymers.

Turbulence

One dimensional turbulent spectra of the streamwise fluctuating velocity have been obtained with the digital system introduced in the previous chapter. Taylor's hypothesis has been employed to transform the frequency spectrum to the wave-number spectrum; following Lawn (1971), we could normalize the spectrum by using the relation,

$$E_1 = \frac{E_1(f)}{u_1^2} \cdot \frac{\bar{U}}{2R} \quad ,$$

where $E_1(f)$ is the spectrum output of the FFT master program.

The spectra for newtonian fluids have been described previously in this chapter. For higher Reynolds numbers, figure 4.11 showed that the normalized spectra appeared to agree with the results of Lawn (1971). For lower Reynolds numbers, however, they showed discrepancies and the inertial subrange had disappeared. The disappearance may possibly be due to the overlapping of the dissipation range and the inertial subrange.

We describe the normalized spectra of the drag-reducing flow as follows. For the Reynolds number 1.4×10^4, we have two cases, namely, no milk and 100 ppm milk. In figure

4.29, we compare the spectra measured at the centre-line of the flow of 300 ppm fibre suspension containing 100 ppm milk. The solid line was the result for water or for the Aerosol OT solution, at the same Reynolds number of 1.4×10^4. The amount of drag reduction appears as a parameter.

In the figure, it can be seen that the drag reductions for Passes 1, 2 and 3 were 69, 58 and 46%, respectively. The spectrum for Pass 1 had a larger value in the high wave-number range, compared with the newtonian result. The low wave-number spectrum was quite close to the newtonian one. In between, there appeared to have a range where the spectrum appeared to have a reduced level compared with the water spectrum. This was bounded in the range between $k_1 \times R =$ 1 and 10, approximately as shown in the figure.

For Pass 2, the reduced level spectral range expanded wider to higher wave-number; while the high wave-number spectrum remained larger than the newtonian result as in Pass 1, a -1 slope appeared in the low wave-number spectrum.

For Pass 3, when the drag reduction dropped down to 46%, the 'reduced level' range still appeared and the high wave-number spectrum agreed with the newtonian result. Like Pass 2, Pass 3 showed a -1 slope spectrum at low wave-number.

Figure 4.30 is for the case of no milk. As shown in the figure, the drag reductions for Passes 1, 2 and 3 were 74, 54 and 51%, respectively. For Pass 1, the spectrum was lower at low wave-number but higher at high wave-number, than the newtonian result. A 'reduced level' range appeared in the range roughly between $k_1 \times R = 1$ and 10. In the

highest wave-number range, the spectrum appeared to be white.

It is somewhat different from Pass 1 of the "100 ppm milk" case. The difference can be seen more clearly in figure 4.5; we see that the "no milk" spectrum in the low wave-number range was lower than that of the "100 ppm milk" case. It could be the result of drag reduction, for the percentage drag reduction of Pass 1 of figure 4.30 was different from that of pass 1 of figure 4.29. (For the '200 ppm milk' case of figure 4.5, we have mentioned that the Reynolds number effect might also play a part in this pass; the Reynolds number was indeed lower than the nominal 1.4×10^4. This explained why, in figure 4.5, the cases of '0 ppm milk' and '200 ppm milk' agreed so well in the lower wave-number range, even although their drag reduction levels were different.)

As for the white spectrum it is also unlikely to be due to the absence of milk for, as shown in figure 4.31, no such spectrum appeared in the result obtained at $y/R = 0.3$ measured in the same flow. The white spectrum could be due to either the optical ambiguity noise of the LDA or the drag reduction of the flow system. In any case, it does not affect our following observation.

In figure 4.5, it can be seen that the spectra were of the same appearance in the range, $3 \leqslant k_1 \times R \leqslant 70$. More important in this regard is the fact that, after the 'reduced level' range, the spectrum for the "no milk" case remained unaffected for a considerable wave-number range before the white spectrum arose. Thus, we conclude that

the 'reduced level' spectrum was the 'true' spectrum of the turbulence modified by the fibre additive, as it appeared.

Returning to figure 4.30, we see that Passes 2 and 3 agreed with each other. They collapsed with the newtonian spectrum at high wave-number but appeared to have a 'reduced level' in the wave-number range as shown. The low-wave-number spectra appeared to have a -1 slope in the diagram.

This feature can also be found in the results measured near the wall in these Passes as well as in Pass 1. Figure 4.31 compares the spectra measured at the centre in Pass 3 with those near the wall in Pass 1. They generally showed the same feature. It can be seen in the figure that the 'reduced level' in both cases lay in the same wave-number range.

Thus far, we have seen two different features of the spectra: one was the 'Pass-1' type for the undegraded fibre suspension, the other one being the type for the degraded fibre suspension.

The spectra in the fibre-polymer mixed system for the undegraded passes were of the same 'Pass-1' type feature. As shown in figure 4.32, the data for Passes 2, 3 and 4 collapsed rather well, showing that the 'Pass-1' type feature was not changed throughout the runs.

Figure 4.33 compares the 'Pass-1' type spectrum of 300 ppm fibre suspension with that of the 300 ppm fibre plus 150 ppm polymer mixture. The spectra appeared almost the same, suggesting that such appearance might have come from the undegraded fibres only but not from the additional

polymer; the polymer might partially act as a stabilizer for the undegraded fibre suspension (McComb and Chan, 1980).

The behaviour of the degraded suspension can be represented by the spectra of Passes 2 and 3 in figure 4.30. For higher Reynolds numbers, all spectra for the suspensions were of similar appearance. Figure 4.34 and 4.35 show the spectra measured at the centre for different passes for the Reynolds numbers 3.2×10^4 and 5.3×10^4, respectively. They showed general agreement between passes, indicating no drag reduction effect except the reduced level on the spectra in the degraded suspension.

We compare the degraded passes for the Reynolds numbers of 1.4×10^4, 3.2×10^4 and 5.3×10^4 in figure 4.36. We notice that the 'reduced level' spectra collapsed with each other reasonably well, suggesting a Reynolds number independence. Again, it indicates that the 'reduced level' was the 'true' spectrum of the modified turbulence.

We have already shown that for the passes of the undegraded fibre suspension, the spectra near the wall (y/R = 0.3) were similar to those for the degraded suspension, as shown in figure 4.31. Yet, for the undegraded fibre-polymer mixture, there was a difference, as shown in figure 4.37. We see that the high wave-number spectrum was higher for the mixed system than that for the fibre suspension alone. A good agreement was found in the -1 slope and 'reduced level' range, nevertheless.

Figure 4.38 compares the spectra measured at two locations across the pipe (y/R = 1 and y/R = 0.1) in the

fibre-polymer mixture. The Reynolds number was 1.4×10^4, as shown in the figure. We see that all the spectra plotted in this figure were apparently of 'Pass-1' type appearance, except that those obtained near the wall have shifted towards higher wave-number. This did not seem to depend on Pass number, so long as the fibre + polymer mixture remained undegraded. This particular feature has not been observed in the fibre suspension alone. The fact that the spectrum, particularly the 'reduced level', shifts to higher wave-number as the wall is approached leads to the following hypothesis: the 'reduced level' of the turbulent spectrum is due to the interaction between fibres and turbulent eddies of comparable sizes. If this is true, we can measure the length scale of the fibres by computing the median of the 'reduced level' wave-number range. This could be done according to the following equation:

$$(\tilde{k}_1)_m = \frac{(\tilde{k}_1)_s + (\tilde{k}_1)_e}{2} \quad ,$$

where $\tilde{k}_1 = k_1 \times R$ and the suffixes m, s and e denote median, starting and ending respectively. The length scale of the eddies could be given by $1/(k_1)_m$. Therefore, $1/(k_1)_m$ could be used as a measure of average fibre length.

By using such a method, we have estimated the average fibre length scales for different passes, as shown in table 4-III. It can be seen that the length of the fibre in the mixture at the centre line was 2.8 mm while near the wall ($y/R = 0.3$) it was at most 1.8 mm. The length at the centre line was 3.4 mm (or at least 2.8 mm for other 'Pass 1' cases)

Table 4-III Estimate of Fibre Length Scales by Using Spectral Method

a) 300 ppm fibre suspension + 100 ppm milk

Re x 10^{-4}	Pass	Length Scales (mm)	
		near wall	centre line
1.4	1	1.6	3.4
	3	1.4	1.4
3.2	1	1.8	1.6
	2	1.4	1.2
5.3	1	1.3	1.3
	4	1.0	1.2

b) 300 ppm fibre suspension + 100 ppm milk + 150 ppm polymer solution

Re x 10^{-4}	Pass	Length Scales (mm)	
		near wall	centre line
1.4	1	1.0	2.8
	2	1.8	2.8
	5	1.8	2.8

in Pass 1 of fibre suspension at the Reynolds number of 1.4×10^4; it was 1.4 mm at the centre line for Pass 3, showing a change in fibre length from Pass 1 to Pass 3. On the other hand, the change was not so important near the wall though the fibre length appeared to be much shorter than 3.4 mm for Pass 1.

Thus, it is concluded that whether the flow behaved a 'Pass-1' type or not was dependent on the length of fibres present at the centre line region. We conclude that the active region in the Pass 1 at the Reynolds number of 1.4×10^4 was at the centre line region. The same could possibly apply to the passes of the undegraded fibre + polymer mixture.

Returning to figure 4.38, we notice that the spectral curves near the wall underwent a marked shift towards higher wave-number compared to that in the core region, implying a much smaller turbulent dissipation scale near the wall.

In view of the 'reduced level' and the various appearances of the spectral curves, we did not calcuate the kolmogorov scale of the streamwise fluctuating velocity by using the 'inertial subrange method' suggested by Lawn (1971). We did attempt to do so. However, the result showed that the kolmogorov wave-number appeared to be too close to the 'inertial subrange', indicating that such method may not be suitable to applying in the flow of fibre suspension.

One noteworthy point is that of the sizes of fibres in the undegradable fibre-polymer mixture. The size of the fibres has been estimated to be about 1 mm very near the

wall (y/R = 0.1) and 2.8 mm at the centre; in between (y/R = 0.3) they were 1.8 mm long as shown in table 4-III. Nevertheless, what made these fibres of specific lengths remain in position while there were possibilities for them to be mixed together by turbulent eddies? In view of the non-degradability of the mixed system, and accepting the fact that fibres were being carried from wall to core and vice versa in the turbulent flow, we conclude that decrease in size of the fibre near the wall was reversible in the mixed system. However, the conclusion is highly speculative.

Correlation and Integral Scale

In this section we present the correlation results of the streamwise fluctuating velocity. The auto-correlation of the turbulent velocity signal was obtained by using an auto-correlator. We used a sufficiently long average time (30 sec) in order to get a smooth curve which in turn was plotted on graph paper using an X-Y recorder.

The auto-correlation coefficient was obtained by dividing the correlation by the zero-time-lag value which was the variance of the signal. The correlation coefficient was then plotted against $t\bar{U}/R$, $\bar{U}$ being the local mean velocity, $\bar{U}(y)$, and R the radius of the pipe. Assuming frozen pattern of the turbulence and according to Taylor's hypothesis, therefore, we were in effect measuring the (spatial) longitudinal correlation of the turbulent flow.

Figure 4.39 shows correlation coefficients of the turbulent velocity measured at the centre-line of the pipe for Passes 1, 2 and 3 of the 300 ppm fibre suspension at

the Reynolds number 1.4×10^4. For comparison, the newtonian result (for water) at the same measuring location and Reynolds number was drawn as a solid curve in the figure.

It can be seen in figure 4.39 that Pass 1 showed a steep fall in the correlation curve for small $t\bar{U}/R$. However, it showed a moderate increase of correlation compared with the newtonian curve for larger value; the correlation decreased with increasing $t\bar{U}/R$ but did not appear to reach zero even when $t\bar{U}/R = 30$.

For Passes 2 and 3, the correlation were substantially increased compared with the newtonian result. We no longer can see the steep fall in the correlation curve for these passes but a gradual decrease in correlation with $t\bar{U}/R$. Also, we can observe a trend to the newtonian curve as the drag reduction decreases.

Figure 4.40 shows the correlation results obtained at the centre-line for Passes 2, 3 and 4 of the fibre-polymer mixture at the Reynolds number 1.4×10^4. The data appeared to cluster together, showing that the correlation was not changing throughout the runs. The correlation curves appeared like that of Pass 1 in the case for 300 ppm fibre, as shown in figure 4.41. In the figure, the correlation curve for the second pass of the fibre-polymer mixture was compared with the first pass of the 300 ppm fibre suspension; they showed good agreement, suggesting that these curves were representative of the longitudinal correlation of the turbulence at the core region in Pass 1 before the transition.

The correlation measured at $y/R = 0.3$ in the flow of

'Pass 1' type showed an increase compared with the water result, like those in figure 4.42. It can be seen that the correlation decreased gradually with $t\bar{U}/R$ in Pass 1 of the fibre suspension whereas it fell steeply at small $t\bar{U}/R$ in the Passes of the fibre-polymer mixture. The difference between them for small value of $t\bar{U}/R$ apparently corresponded to that of the spectra at high wave-number shown in figure 4.37.

Figure 4.43 compares the foregoing correlation curve for the fibre suspension with that measured at the centre-line in the degraded suspension. It showed some differences but qualitatively they contained the same feature, namely, an increase in correlation compared with the newtonian result.

For the degraded suspension, the correlation appeared to be proportional to drag reduction. Returning to figure 4.39, we see that the correlation curve for Pass 2 was notably high compared with both Pass 1 and the water result. In later passes, the correlation decreased as the drag reduction decreased. Such behaviour has been observed in the polymer solution by McComb and Rabie (1979).

Figures 4.44 and 4.45 show the correlations for different passes at Reynolds numbers of 3.2×10^4 and 5.3×10^4, respectively. At constant Reynolds number, the correlation showed a trend to the newtonian result with decreasing drag reduction. The polymer-like trend was similar to that revealed previously in the results of mean velocity profiles and intensity profiles at these Reynolds

numbers. Thus, we once again observe an obvious transitional behaviour of the fibre suspension due to degradation.

The turbulence integral scale can be defined as

$$L_{11} = \int_0^\infty R_{11}(r)\, dr \quad ,$$

where r is the separation between two measuring points in the turbulent field in the streamwise direction. This length is to a certain extent a measure of the longest connection, or correlation distance, between the velocities at two points of the flow field. In principle, streamwise velocity components at two points separated r apart in the flow field must be measured to obtain $R_{11}(r)$.

In our case, however, we have measured the streamwise velocity component at one point in the field only. As we pointed out previously, the auto-correlation coefficient of the streamwise velocity component can be related to the longitudinal correlation coefficient if Taylor's hypothesis is assumed to be valid. Therefore, we can still estimate L_{11} through the relationship written as:

$$L_{11} = \bar{U} \times T_E$$

where $\bar{U}$ is the local mean velocity, $\bar{U}(y)$, and T_E is given by:

$$T_E = \int_0^\infty R_E(t)\, dt \quad ,$$

where $R_E(t)$ is the Eulerian correlation coefficient. T_E is considered to be a rough measure of the longest connection in the turbulent behaviour of the streamwise fluctuating velocity.

Figure 4.46 shows a typical auto-correlation curve, correlation being plotted against time lag. As shown in

the figure, the correlation at zero time lag is equal to the variance of the fluctuating velocity signal. Although the averaging time taken for the auto-correlation curves was fairly long, some of the curves appeared to have a negative value at large value of the time lag. Fortunately, the proportion of the 'negative' area to the shaded area, A, is not large, namely, 8% at most. In view of the large amplitude of change in the integral time scale due to fibre, simply using the shaded area 'A' for computing T_E would be sufficient for estimating the integral scale, and the estimate of T_E is according to the following formula:

$$T_E = \frac{A}{u^2} \quad .$$

Figure 4.47 shows the integral length scale for newtonian fluids (water and Aerosol OT solution) plotted against y/R. It can be seen that the results were comparable to the hot-wire results of Sabot et al (1977).

Table 4-IV shows the integral scales of the turbulence of the drag-reducing fluids. (a) applies to the 300 ppm fibre suspension, (b) to the mixture. For the Reynolds number 3.2×10^4 in (a), it can be seen that the integral scales (length and Eulerian time) were substantially enhanced at the centre-line and that a decrease with decreasing drag reduction was observed, like that in polymer solutions (McComb and Rabie, 1979); near the wall the same trend can be seen. Similarly, for the Reynolds number 5.3×10^4, such behaviour is shown in (a).

In (a) for the Reynolds number 1.4×10^4, it can be seen that although the drag reduction percentage of Pass 1

Table 4-IV Integral Scales of the Turbulence

a) 300 ppm fibre suspension

Re x 10^{-4}	Pass	DR(%)	Length scale (mm)		Time scale (m sec)	
			near wall	centre line	near wall	centre line
1.4	1	69	15	7	18	5
	2	58	19	18	25	16
	3	46	18	17	19	15
3.2	1	71	40	80	25	32
	2	62	40	40	24	18
	3	58	30	10	19	14
5.3	1	54	20	20	7	5
	2	52	20	10	6	3
	4	46	20	10	6	2

b) 300 ppm fibre suspension + 150 ppm polymer solution

Re x 10^{-4}	Pass	DR(%)	Length scale (mm)		Time scale (m sec)	
			near wall	centre line	near wall	centre line
1.4	2	58	16	9	17	7
	3	61	16	8	18	6
	4	58	13	7	16	5

c) Earlier experiments for Reynolds number of 1.4 x 10^4

Re x 10^{-4}	Pass	DR(%)	Length scale (mm)		Time scale (m sec)	
			near wall	centre line	near wall	centre line
1.4	1	69	10	0.3	6	0.2
	2	76	10	2	6	1.3
	3	56	20	20	15	16
	6	48	20	10	18	11

(69%) was larger than those of Pass 2 (58%) and 3 (46%), the length scales at the centre-line of Pass 1 were much smaller than those of the later passes. For Passes 2 and 3, the suspension behaved like polymer solution, showing enhancement of streamwise length and time scales compared with water results at centre (T_E = 1.9 ms, L_{11} = 5 mm) and a declining trend of the scales as drag reduction decreased.

It is somewhat different for Pass 1 at Reynolds number 1.4×10^4, however, in that the length scale did not show substantial enhancement like those at Pass 1 of 3.2×10^4. It can be concluded therefore that the turbulent behaviour of Pass 1 at 1.4×10^4 was different from that in the Passes showing 'polymer-like' behaviour.

The integral scales in the undegraded fibre-polymer solution were of the same magnitude as shown in table 4-IV (b). They were smaller than those in water alone, as shown in (c), for the earlier experiment for the Reynolds number 1.4×10^4.

In summary, we have shown that in the undegraded system, the integral scales of turbulence did not seem to be increased, and, indeed, sometimes decreased. In degraded suspensions, the amount of increase depended upon the drag reduction level at constant Reynolds number.

Bursting Period

The bursting process has been visualized and investigators (like Kim, Kline and Reynolds, 1971) have shown that it is associated with the production of turbulence energy and with the transfer of it through the wave-number

space to smaller eddies to dissipate it. Thus, the bursting rate has been used as a relative measure of the turbulence production rate. The reciprocal of this is called the bursting period.

There are several methods to measure the bursting period, one of them being the 'short-time' averaged auto-correlation technique, first described by Kim, Kline and Reynolds (1971). They showed that the mean interval between bursts could be obtained by measuring the time between peaks of the resulting auto-correlations.

Strickland and Simpson (1975) have shown that auto-correlations taken over a 'short' period of time display distinct peaks, the location of which appeared to be essentially independent of the sampling time for short times. Because of the variation in the bursting period obtained in this way, they suggested using 26 samples to get a satisfactory estimate of the mean value. Mizushina and Usui (1977), however, used 20 samples only, having found that the average value of 20 samples did not differ from that of 100 samples.

Using the same technique ('short-time' auto-correlation), we have used about 30 or more samples to obtain the estimate of the mean bursting period, $\bar{T}_B$. This number of samples was just below our obtainable limit: we have studied a restricted volume of flowing suspensions. On the other hand, we have results obtained only in the wall region. However, it could not be a problem for we knew that the bursting period is the same across the whole boundary

layer.[+]

Figure 4.48 shows some typical traces of the 'short-time' auto-correlation, taken in the fibre suspension or in water at the Reynolds number about 3.0×10^4: note the change in scale of the time axis. Traces at other Reynolds numbers have the same appearance. We see immediately in the figure that the bursting period increased with increasing drag reduction, implying a suppression of bursting events in the fibre suspension.

Table 4-V shows the bursting period for different passes at different Reynolds numbers. The experiment for Reynolds number 1.4×10^4 was carried out at the earlier stage, and we have shown that Passes 1 and 2 were of the 'Pass-1' type behaviour. It can be seen in the table that the bursting period increased with and was proportional to the drag reduction, indicating that whether or not the suspension was degraded, the suppression of bursting events was responsible for the drag reduction.

Also shown in table 4-V are the bursting periods for Reynolds numbers 3.2×10^4 and 5.3×10^4. It can be seen

[+] Hinze (1975) showed that the average bursting period was almost constant across the whole boundary layer. Mizushina and Usui (1977) found that the mean bursting period obtained in the wall region $10 \leqslant y^+ \leqslant 100$ had a constant value across the whole region for a given Reynolds number. Sabot and Comte-Bellot (1976) showed that in the region $0.1 \leqslant y/R \leqslant 0.5$, $\bar{T}_B$ was constant. McComb and Rabie (1979), using the 'short-time' auto-correlation technique, verified that $\bar{T}_B$ was the same over the cross-section of the pipe.

Table 4-V The Bursting Period

Re x 10^{-4}	Pass	DR(%)	$\bar{T}_B$(sec)	$\frac{u^{*2}\bar{T}_B}{\nu}$	$\frac{\bar{U}_o\bar{T}_B}{R}$
1.4	1	69	0.35	257	57
	2	76	0.44	250	68
	3	56	0.32	317	46
	water	0	0.06	140	8
3.2	1	71	0.44	1134	110
	2	62	0.34	1160	77
	3	58	0.26	844	54
	water	0	0.03	300	9
5.3	1	54	0.10	1030	40
	2	52	0.08	880	31
	4	46	0.08	915	31
	water	0	0.02	350	8

that the bursting period was substantially enhanced over the water results and proportional to the drag reduction.

Discussion

Two different behaviours have been observed in the flow of 300 ppm fibre suspension. The flow behaviour of the 'undegraded' fluid was completely different from that of the 'degraded' suspensions, the latter being like the result of polymer solutions. A simple fact has been revealed, i.e. the transition between two flow behaviours due to the degradation of the asbestos fibres we used.

Prior to the discussion, the meaning of the terms 'degraded' and 'undegraded' fibre suspensions is explained. The degraded suspension is the fluid that produces 'polymer-like' results and the 'undegraded' (or fresh) fibre suspension is that which produces 'Pass-1' type results. This kind of degradation effects the transition and implies a structural change of the turbulent flow; so we call it structural degradation. After this, the 'degraded' suspension is still degradable, with results behaving somewhat like polymer solutions'; we simply call it degradation.

Distinguishing between the two behaviours, we discuss firstly the 'polymer-like' behaviour of the 'degraded' suspension, which is defined as a behaviour of the flow that can be observed if the fibres were replaced by the polymer, giving a comparable drag reduction. It does not mean however that the fibre should behave like polymer molecules in reducing friction though this is also possible.

'Polymer-like' result

After the structural degradation, our results showed that the mean velocity profiles (U^+ versus y^+) had slope less than that of the ultimate asymptotic profile, the slope being dependent on the amount of drag reduction. The mean profiles appeared to be bounded by Virk's ultimate and the newtonian profiles. On the other hand, the turbulent intensity (u/u^*) was greater than that of the water alone, its magnitude being proportional to the level of drag reduction. The high wave-number spectrum did not have special change compared with the newtonian result. A 'reduced level' was observed in the medium wave-number range and a -1 slope appeared in the low wave-number spectrum even although it was measured at the centre-line of the pipe. The correlation and the integral scales of the streamwise velocity component were enhanced and proportional to the drag reduction; and depending on it, the bursting rate was suppressed, showing a reduction of turbulence production rate.

The picture was similar to that observed in the drag-reducing flow of the polymer solutions. (We have discussed this in chapter 1.) The exception is that the 'reduced level' seems to be unique in the fibre suspension. This could mean that the length scale of fibres is still much larger than that of the polymer molecules although they produce results of the same behaviour.

Most of our mean velocity profiles showed two separate layers, namely, the turbulent core region and the intermediate layer. Including the viscous sublayer which we expected to exist, there are three layers altogether.

In the turbulent core region, like that observed in polymer solutions (McComb and Rabie, 1979; Reischman and Tiederman, 1975; Rudd, 1972), the mean velocity profile of the suspension showed a shift upward from the newtonian line; and its slope did not change with drag reduction. The profiles in the intermediate layer had slope varying with drag reduction, showing a trend to the newtonian profiles as drag reduction decreased.

The intermediate layer can be considered as a thickened buffer zone like that in the flow of polymer solutions. McComb and Rabie (1979) used LDA to get mean velocity profiles showing such a thickened layer. They called it the polymer interactive layer, implying that the polymer molecules interact with the flow in the region to reduce friction. Reischman and Tiederman (1975), however, called it the thickened buffer layer although they had already recognized it as an interactive region. McComb and Rabie showed that it was indeed the area of importance and change in the drag-reducing flows of polymer solutions.

Their experimental profiles in the interactive layer showed that the slope of a profile was proportional to the drag reduction percentage, similar to our results for 'degraded' suspension. Thus questions arise: do the fibres interact with the flow in the intermediate layer to reduce friction? If so, do they interact with the bursts near the wall and how?

It seems quite reasonable to accept this in view of the broad similarity between our results for 'degraded'

fibre and those of the polymer. In polymer solutions, it has been shown that only when polymer additives were present at the near wall region did the whole structure of the flow change significantly. Our results showed that the whole structure of the flow of the fibre suspension has changed, the change being so similar to the polymeric result that the cause of it might have also originated from the near wall region.

The fibres did suppress the bursts near the wall of the pipe as we have shown in the previous section. However, how they suppress them is an open question.

In view of the aforementioned similarity of results and knowing that the size of a polymer molecule is much smaller than a fibre, we propose that in polymer solution, polymer molecules may have formed an agglomeration to interact with the burst near the wall. This point of view has already been proposed by investigators such as Moyls and Sabersky (1978) and Rabie (1978).

'Fibre-like' result

Secondly, we discuss the 'Pass-1' type behaviour in the flow of fibre suspension. This has been observed in the flows at lower Reynolds numbers of 9.0×10^3 and 1.4×10^4; for the latter, we have repeated the velocity measurement several times in the same rig with the LDA containing a different tracking filter (DISA 55N20) and similar kind of fibre suspension at concentration of 300 ppm, finding that observations coincide very well. We were especially encouraged when we observed the same behaviour in the

undegraded fibre-polymer mixture which appeared to be undegradable.

The 'Pass-1' type behaviour is described as follows: drag reduction percentage was the maximum obtainable with the fluid; the amount appeared not to be limited by the Virk's maximum drag reduction asymptote; the mean velocity profiles also appeared not to be restricted by the ultimate asymptotic profile and their slopes appeared to be greater than the latter; the streamwise turbulent intensities were suppressed compared with the newtonian result; the spanwise component was shown to be enhanced; the spectra for the streamwise component showed a shape with a 'kink' in the medium wave-number range, with a higher energy level at higher wave-number; the correlations were suppressed markedly at small $t\bar{U}/R$, and integral scales were of a similar order of length as the newtonian result, even sometimes smaller; the bursting rate was suppressed, implying a suppression of turbulence production.

This picture was obviously different from that of the 'polymer-like' case in later runs, as described previously. We were rather sure that this behaviour was due to a mechanism different from that which governs the drag reduction in degraded fibre suspension (giving polymer-like behaviour).

McComb (1973) has deduced theoretically that long fibres in a turbulent 'simple' shear flow will suppress the streamwise fluctuating velocity, indicating that they will create a process to transfer the energy of the stream-

wise component to other two components, implying that the spanwise and radial fluctuating components are enhanced. Bobkowicz and Gauvin (1967) have shown that the radial component of the turbulent fluctuation in a pipe flow was enhanced, proportional to the aspect ratio of the fibre.

McComb's theoretical argument depended on the assumption that the fibres should align in the streamwise direction, therefore assuming a simple shear flow in which a fibre should spend most of the time aligning with the flow.

In turbulent pipe flow, near the wall, this assumption is hardly satisfied because the region is highly rotational; in the core region, however, it is quite possible, for the flow is more irrotational there (Lumley, 1973).

We have previously concluded that the 'Pass-1' type behaviour was observed only when the 'undegraded' longer fibres were present at the centre-line region. Comparing with table 4-IV for the integral scales and the correlation curves, we find that the suppression of the correlation and the smallness of the integral scales were associated with the presence of these fibres.

Thus, McComb's assumption can be satisfied in the core region, and if his theory is applicable to the drag reduction of 'undegraded' fibre suspension, the process should take place at the centre-line area.

So, the mechanisms underlying the drag reduction of the 'degraded' and 'undegraded' fibre suspensions are entirely different. A question arises: what causes the transition? The transition is due to degradation of fibre

suspension (note: we have called it structural degradation). Its nature has yet to be found; we have some samples of the fibre suspension and fibre-polymer mixture taken before each pass of the fluid stuff at the Reynolds number 1.4 x 10^4. They will be examined in an electron microscope at TBA Ltd. The results should be presented later but not in this thesis. Surely, they will shed some light on the nature of the degradation of fibres; hopefully, the understanding in this regard will help us know more about the drag reduction of polymer solution.

Conclusion

The detailed analysis was limited to the effect of the TB asbestos fibre additives on the streamwise fluctuating velocity in the pipe flow. For the Reynolds number of 1.4 x 10^4, the intensity of the spanwise component was also measured.

The analysis showed that the flow of the suspension had two different behaviours, one like the flow of the fibre suspension in the experiments of Bobkowicz and Gauvin (1967) and Daily and Bugliarello (1961), the other like that commonly observed in polymer solutions.

A transitional behaviour was observed; the degradation of fibre suspension seemed to be the factor causing this transition. Polymer solution appeared to be the agent suppressing the degradation of the fibre suspension.

We have not tried to propose a mechanism underlying the drag reduction of fibre suspension nor attempted to speculate the nature of the degradation causing transition.

However, we have suggested that, before the transition, fibres were active in the core region causing drag reduction, and afterwards, they were active in the near wall region behaving like polymer molecules.

In the future, it is worth while to measure the turbulent spectra of the spanwise and radial fluctuating velocities in the asbestos fibre suspension. This could show us information about the 'reduced level' in the streamwise spectrum. We also suggest that one could do some similar experiments by injecting fibre suspension, following Rabie (1978)'s work in injecting polymer solution. This could show us if an undegraded suspension is active in the core and whether the transition is accompanied with a change of active region from the core to the wall.

REFERENCES

Abbiss, J.B., Chubb, T.W. and Pike, E.R. (1974) Opts. Laser Tech. Dec., 249.

Adrian, R.J. and Goldstein, R.J. (1971) J. Phys. E. 4, 505.

Allan, J. (1976) Mech. Eng. Dept. Research Report, University of Edinburgh.

Angus, J.C., Edwards, R.V. and Dunning Jr., J.W. (1971) AIChE J. 17, 1509.

Bakewell Jr., H.P. (1966) PhD thesis, Pennsylvania State Uni.

Bakewell Jr., H.P. and Lumley, J.L. (1967) Phys. Fluids, 10, 1880.

Batchelor, G.K. (1969) Phys. Fluids, 12, II-233.

Batchelor, G.K. (1971) J. Fluid Mech. 46, 813.

Berman, N.S. and George, W.K. (1974) Phys. Fluids, 17, 250.

Berman, N.S. (1977) Phys. Fluids 20, S168.

Bobkowicz, A.J. and Gauvin, W.H. (1967) Chem. Eng. Sci. 22, 229.

Brayton, D.B., Kalb, H.T. and Crosswy, F.L. (1973) Appl. Opts. 12, 1145.

Chung, J.S. and Graebel, W.P. (1972) Phys. Fluids, 15, 546.

Cummins, H.Z., Knable, N. (1963) Proc. IEEE 51, 1246.

Daily, J.W. and Bugliarello, G. (1961) Tappi. 44, 497.

Davies, G.A. and Ponter, A.B. (1966) Nature 212, 66.

Denham, M.K., Briard, P. and Patrick, M.A. (1975) J. Phys. E. 8, 681.

Dickson, K. (1978) Mech. Eng. Dept. Research Report, University of Edinburgh.

Donohue, G.L. and Tiederman, W.G. (1971) ASME/ESL Film

Lib. N.Y.

Donohue, G.L., Tiederman, W.G. and Reischman, M.M. (1972) J. Fluid Mech. 56, 559.

Edwards, R.V., Angus, J.C., French, M.J. and Dunning Jr., J.W. (1971) J. Appl. Phys. 42, 837.

Ellis, H.D. (1970) Nature 226, 352.

El'perin, I.T. and Smol'skii, B.M. (1965) (Ref. to Little et al 1975).

El'perin, I.T., Smol'skii, B.M. and Leventhal, L.I. (1967) Int. Chem. Eng. 7, 276.

Foreman, J.W., George, E.W. and Lewis, R.D. (1965) Appl. Phys. Lett. 7, 77.

Foreman, J.W., Lewis, R.D. and Thornton, J.R. (1966) Proc. I.E.E.E. 424.

George, W.K. and Lumley, J.L. (1973) J. Fluid Mech. 60, 321.

Goldstein, R.J. and Kreid, D.K. (1967) Trans. ASME, Appl. Mech. Dec., 813.

Goldstein, R.J. and Hagen, W.F. (1967) Phys. Fluids 10, 1349.

Greated, C.A. (1969) Nature 224, 1196.

Hanratty, T.J., Chorn, L.G. and Hatziavramidis, D.T. (1977) Phys. Fluids 20, S112.

Hinch, E.J. (1977) Phys. Fluids 20, S22.

Hinze, J.O. (1959) "Turbulence" McGraw-Hill Inc.

Hinze, J.O. (1975) "Turbulence" 2nd Ed. McGraw-Hill Inc.

Hoyt, J.W. and Fabula, A.G. (1964) Proc. 5th Symp. Naval Hydr. Bergen, Norway ACR-112, 947.

Hoyt, J.W. (1972) Fleet Eng. Dept., NUC TP 299.

Jeffrey, D.J. and Acrivos, A. (1976) AIChE J. 22, 417.

Kale, D.D. and Metzner, A.B. (1974) AIChE J. 20, 1218.

Kale, D.D. and Metzner, A.B. (1976) AIChE J. 22, 669.

Kim, H.T., Kline, S.J. and Reynolds, W.C. (1971) J. Fluid Mech. 50, 133.

Lading, L. (1971) Appl. Optics J. 10, 1943.

Laufer, J. (1954) NACA Report 1174.

Laufer, J. and Badri Narayanan, M.E. (1971) Phys. Fluids 14, 182.

Lawn, C.J. (1971) J. Fluid Mech. 48, 477.

Lee, W.K., Vaseleski, R.C. and Metzner, A.B. (1974) AIChE J. 20, 128.

Little, R.C. (1969) I & E C Fundamentals 8, 520.

Little, R.C., et al (1975) I & E C Fundamentals 14, 283.

Logan, S.E. (1972) AIAA J. 10, 962.

Lumley, J.L. (1969) Ann. Rev. Fluid Mech. 1, 367.

Lumley, J.L. (1973) Macromol. Rev. 1, 263.

Lumley, J.L. (1977) Phys. Fluids 20, S64.

McComb, W.D. (1973) Nature, 241, 117.

McComb, W.D. and Rabie, L.H. (1978) Nature 273, 653.

McComb, W.D. and Rabie, L.H. (1979) Part I, II and III, to be published.

McComb, W.D. and Chan, K.T.J. (1979) Nature, 280, 45.

McComb, W.D. and Chan, K.T.J. (1980) to be published in Nature.

Metzner, A.B. (1977) Phys. Fluids 20, S145.

Mih, W. and Parker J. (1967) Tappi. 50, 237.

Mizushina, T. and Usui, H. (1977) Phys. Fluids 20, S100.

Moyls, A.L. and Sabersky, R.H. (1978) Int. J. Heat Mass

Transfer, 21, 7.

Offen, G.R. and Kline, S.J. (1975) J. Fluid Mech. 70, 209.

Oldroyd, J.G. (1949) Proc. 1st Int. Congr. on Rheol. II, 130.

Oldroyd, J.G. (1950) Proc. Roy. Soc. London Ser. A 20, 523.

Peyser, P., Little, R.C. and Singleterry, C.R. (1971) N.R.L. Report 7227.

Peyser, P. (1973) J. Appl. Poly. Sci. 17, 421.

Pike, E.R., Jackson, D.A., Bourke, P.J. and Page, D.I. (1968) J. Phys. E. 1, 727.

Rabie, L.H. (1978) PhD thesis Mech. Eng. Dept. University of Edinburgh.

Ramu, K.L. and Tullis, J.P. (1976) J. Hydronautics 10, 55.

Reischman, M.M. and Tiederman W.G. (1975) J. Fluid Mech. 70, 369.

Rudd, M.J. (1969) J. Phys. E. 2, 55.

Rudd, M.J. (1972) J. Fluid Mech. 51, 673.

Savins, J.G. (1961) J. Inst. Petroleum 47, 329.

Sabot, J., Saleh, I. and Comte-Bellot, G. (1977) Phys. Fluids, 20, S150.

Schlichting, H. (1955) "Boundary Layer Theory," London: Pergamon Press Ltd.

Seyer, F.A. and Metzner, A.B. (1969) AIChE J. 15, 426.

Sharma, R.S., Seshadri, V. and Malhotra, R.C. Chem. Eng. Sci. 34, 703.

Stevenson, W.H. (1970) Appl. Opt. 9, 649.

Strickland, J.H. and Simpson, R.L. (1975) Phys. Fluids 18, 306.

Toms, B.A. (1948) Proc. Int. Congr. Rheol., 2, 135.

Townsend, A.A. (1956) "The Structure of Turbulent Shear Flow," Cambridge University Press.

Vaseleski, R.C. and Metzner A.B. (1974) AIChE J. 20, 301.

Virk, P.S., Merrill, E.W., Mickley, H.S., Smith, K.A. and Mollo-Christensen, E.L. (1967) J. Fluid Mech. 30, 305.

Virk, P.S., Mickley, H.S. and Smith, K.A. (1970) Trans. ASME, June, 488.

Virk, P.S. (1971) J. Fluid Mech. 45, 225.

Wallace, J.M., Eckelmann, H. and Brodkey, R.S. (1972) J. Fluid Mech. 54, 39.

Walsh, M. (1967) PhD thesis C.I.T.

Wang, C.P. (1971) Appl. Phys. Lett. 18, 522.

Wang, C.P. (1972) Appl. Phys. Lett. 20, 339.

Wang, C.P. (1973) Appl. Phys. Lett. 22, 154.

Wang, C.P. and Snyder, D. (1974) Appl. Opt. 13.

Weinberger C.B. (1970) PhD thesis, Uni. of Michigan.

Wickramasingle, (1971) "Light Scattering Functions for Small Particles with Applications in Astronomy".

Willmarth, W.W. and Bogar, T.J. (1977) Phys. Fluids, 20, S9.

Yeh, Y. and Cummins, H.E. (1964) Appl. Phys. Lett. 4, 176.

FIGURE CAPTIONS

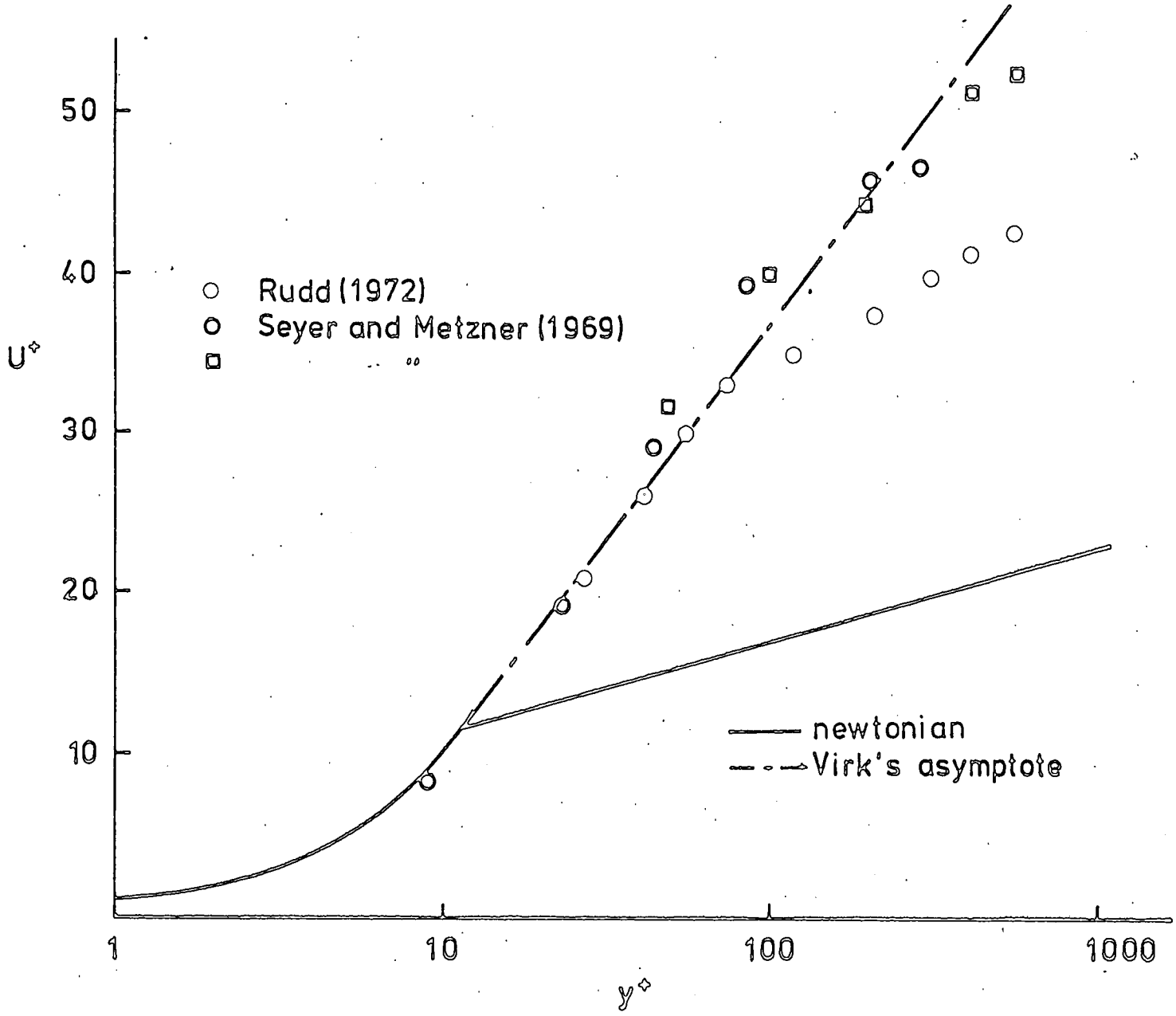

Fig 1.1 Mean Velocity Profiles in Polymer Solutions

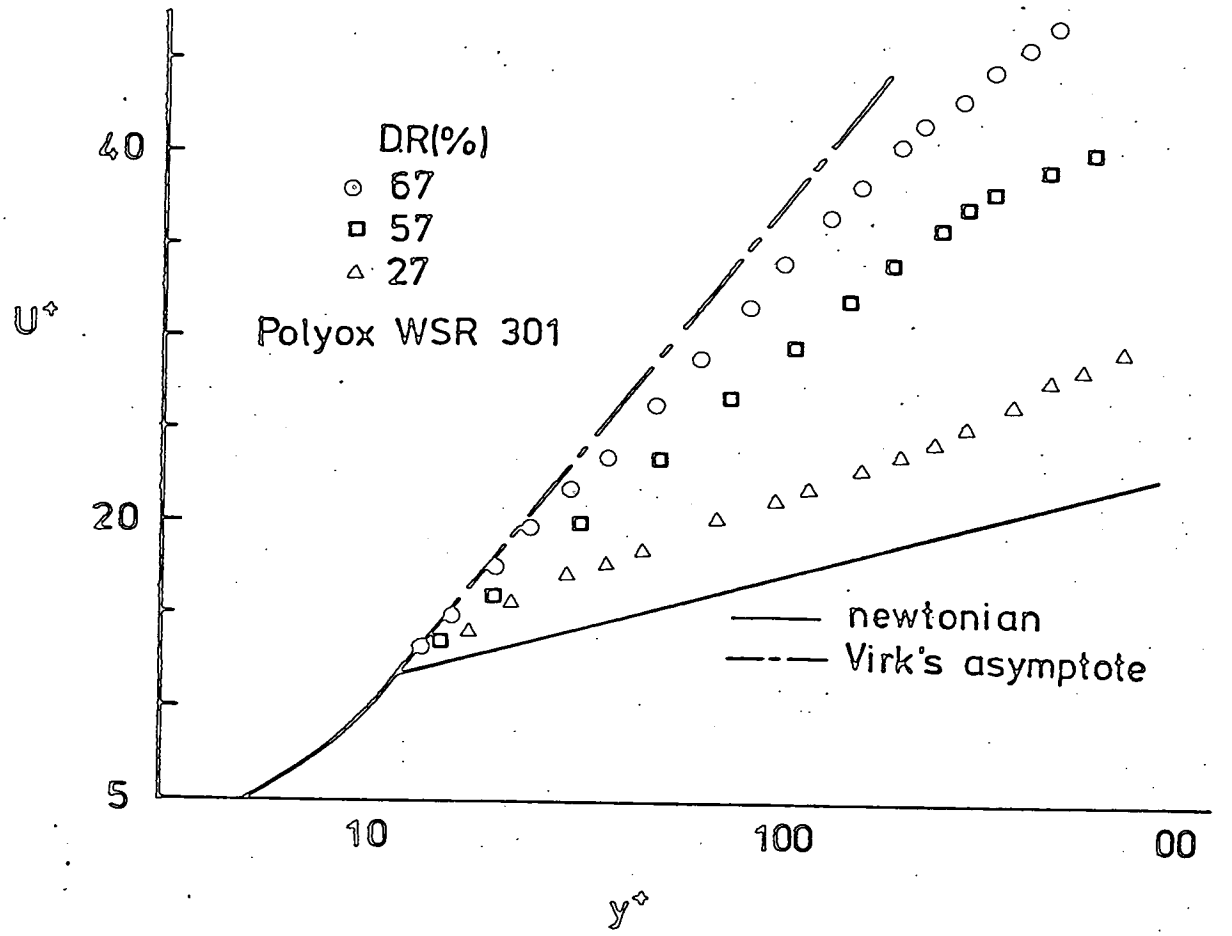

Fig 1.2 Mean Velocity Profiles in Polymer Solution (McComb and Rabie, 1979)

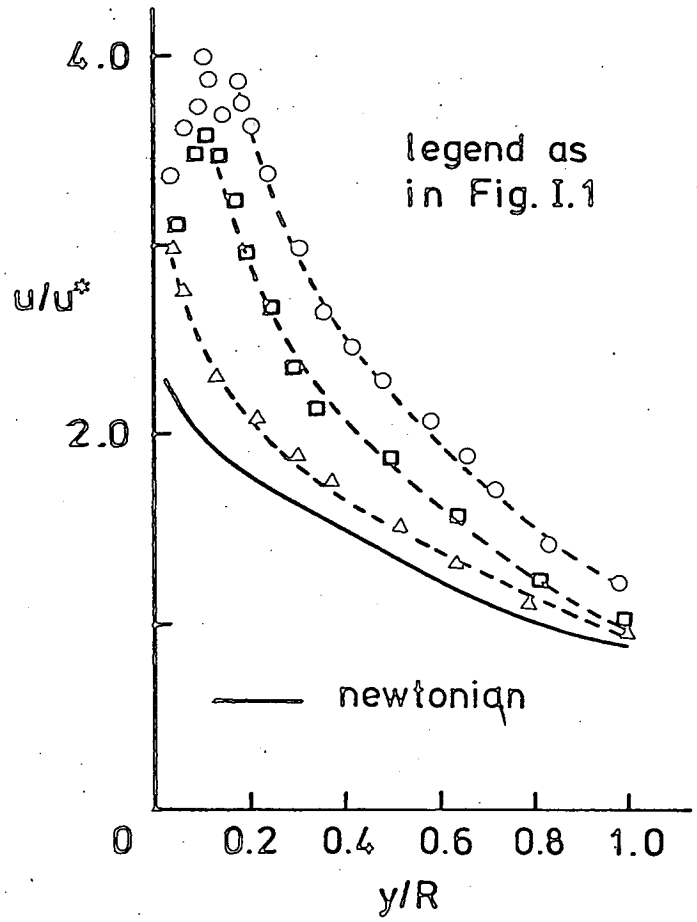

Fig 1.3 Turbulent Intensities in Polymer solution (McComb and Rabie, 1979)

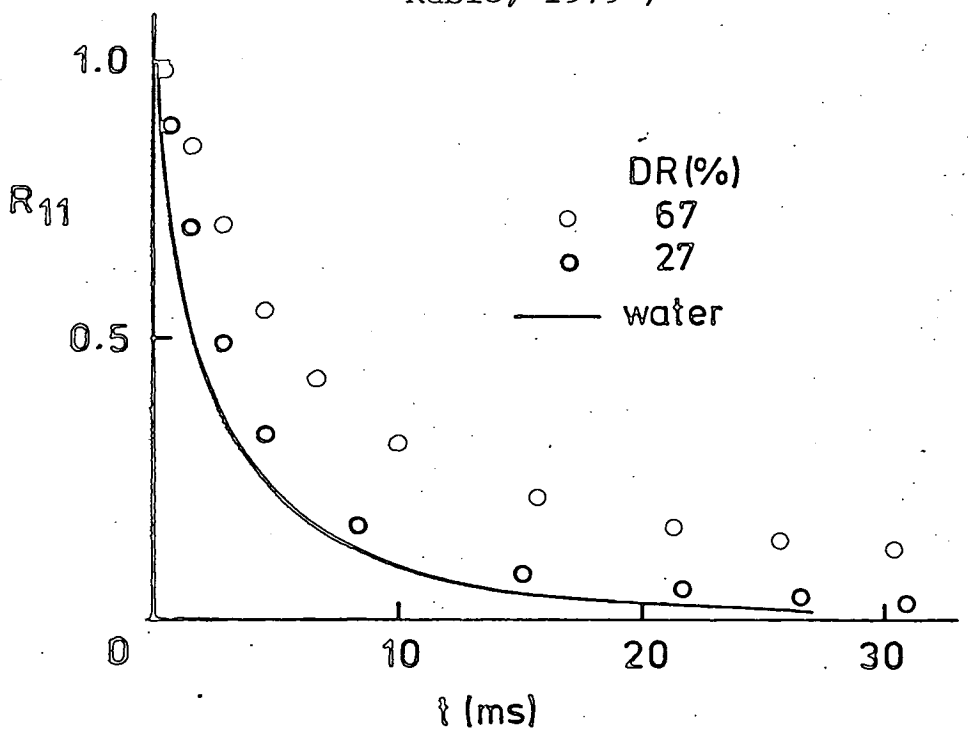

Fig 1.4 Auto-correlations in Polymer Solution (McComb and Rabie, 1979)

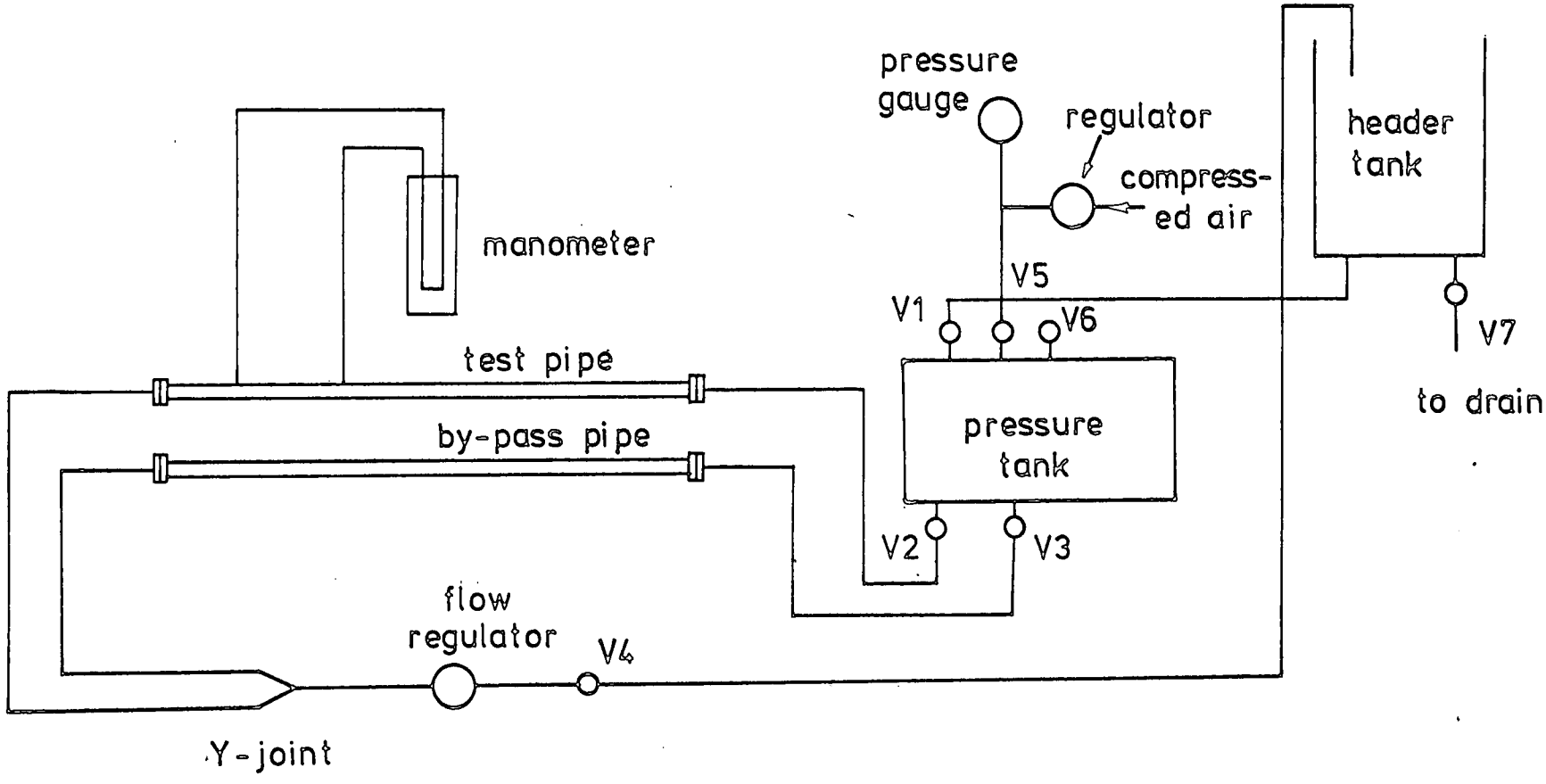

Fig 2.1 Flow Diagram of The Experimental Set-up

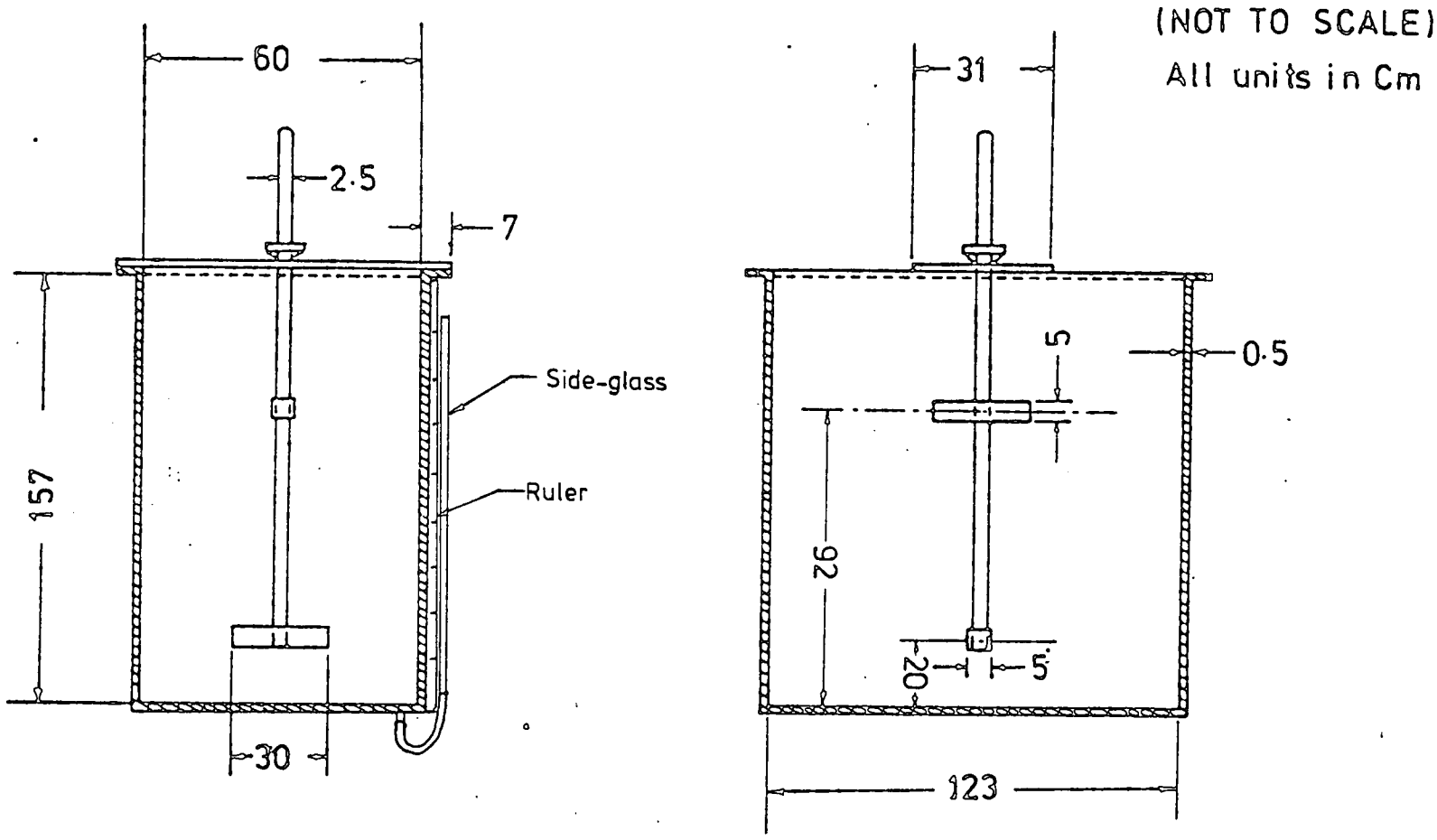

Fig 2.2 Header Tank with The Manual Stirrer

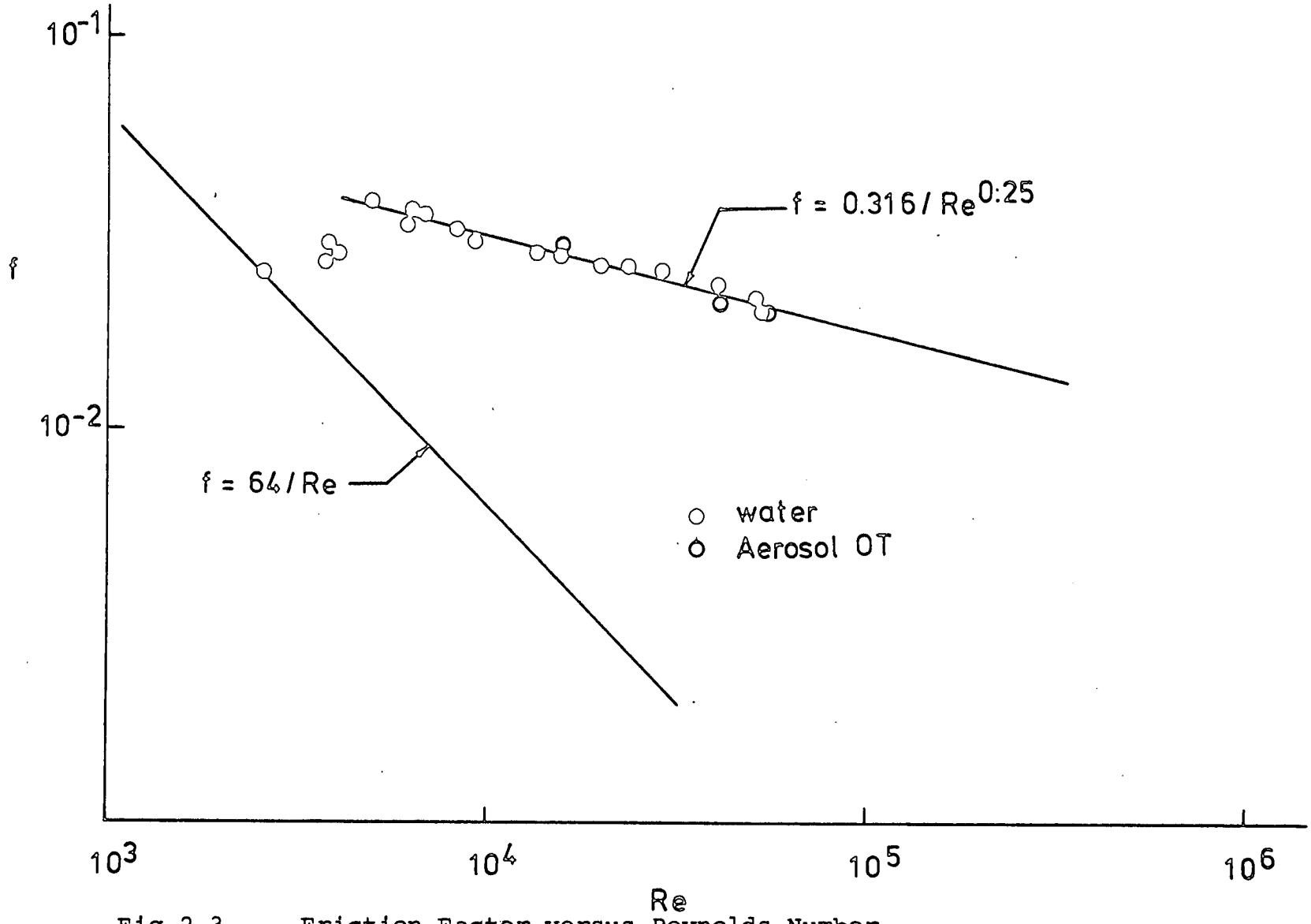

Fig 2.3 Friction Factor versus Reynolds Number

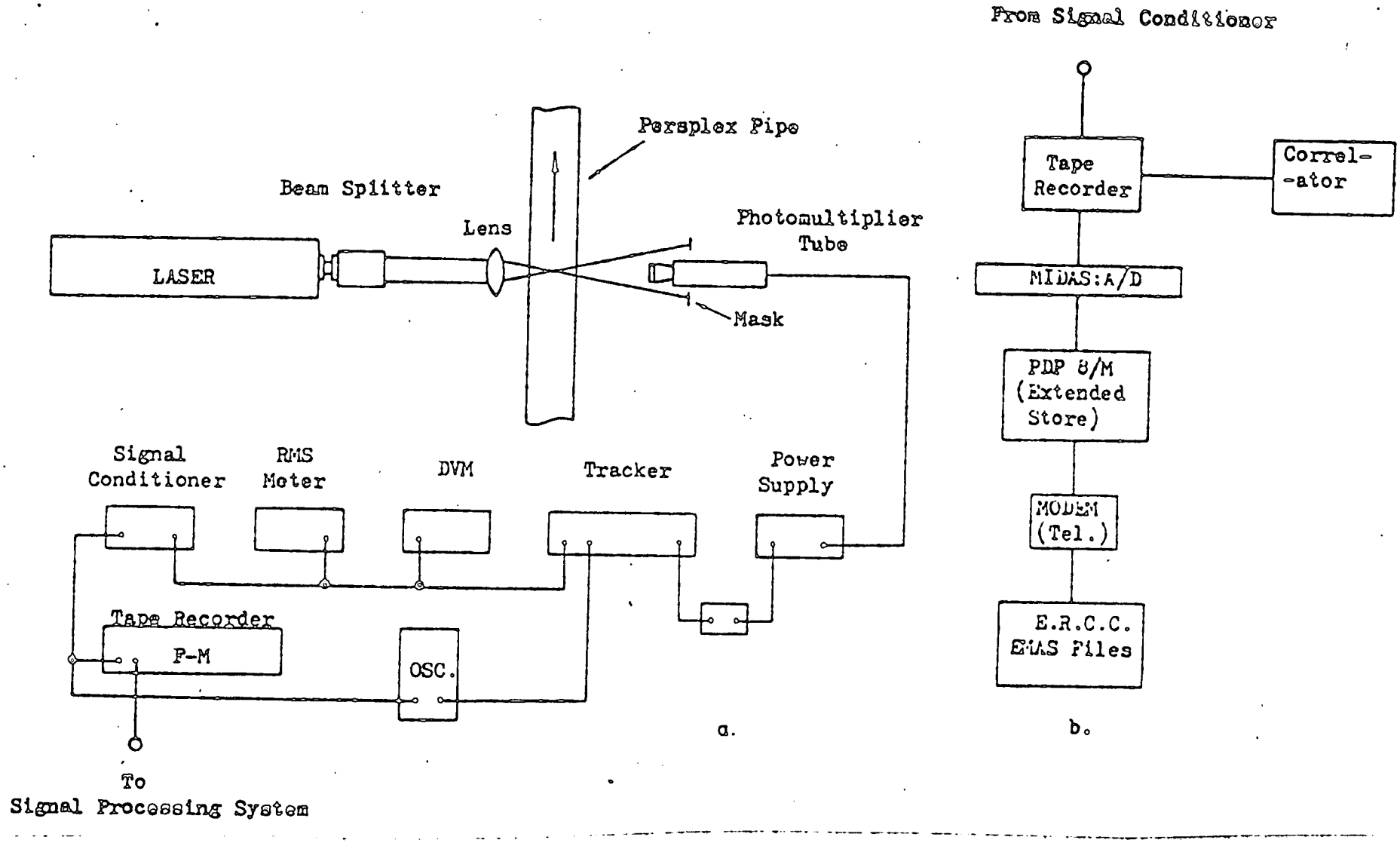

Fig 3.1 a) Schematic Diagram of The LDA, b) Data Acquisition System

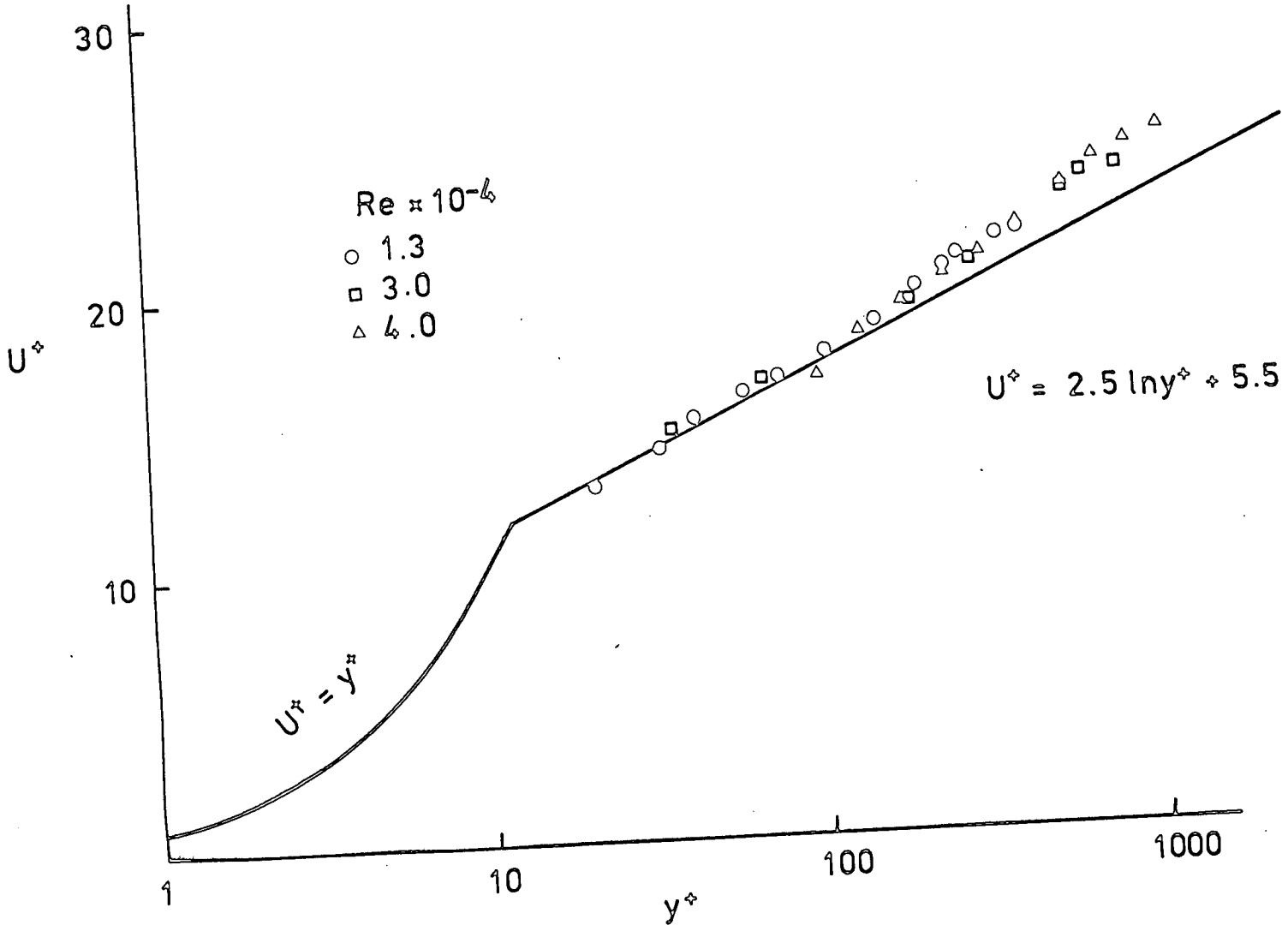

Fig 3.2 The Mean Velocity Profiles

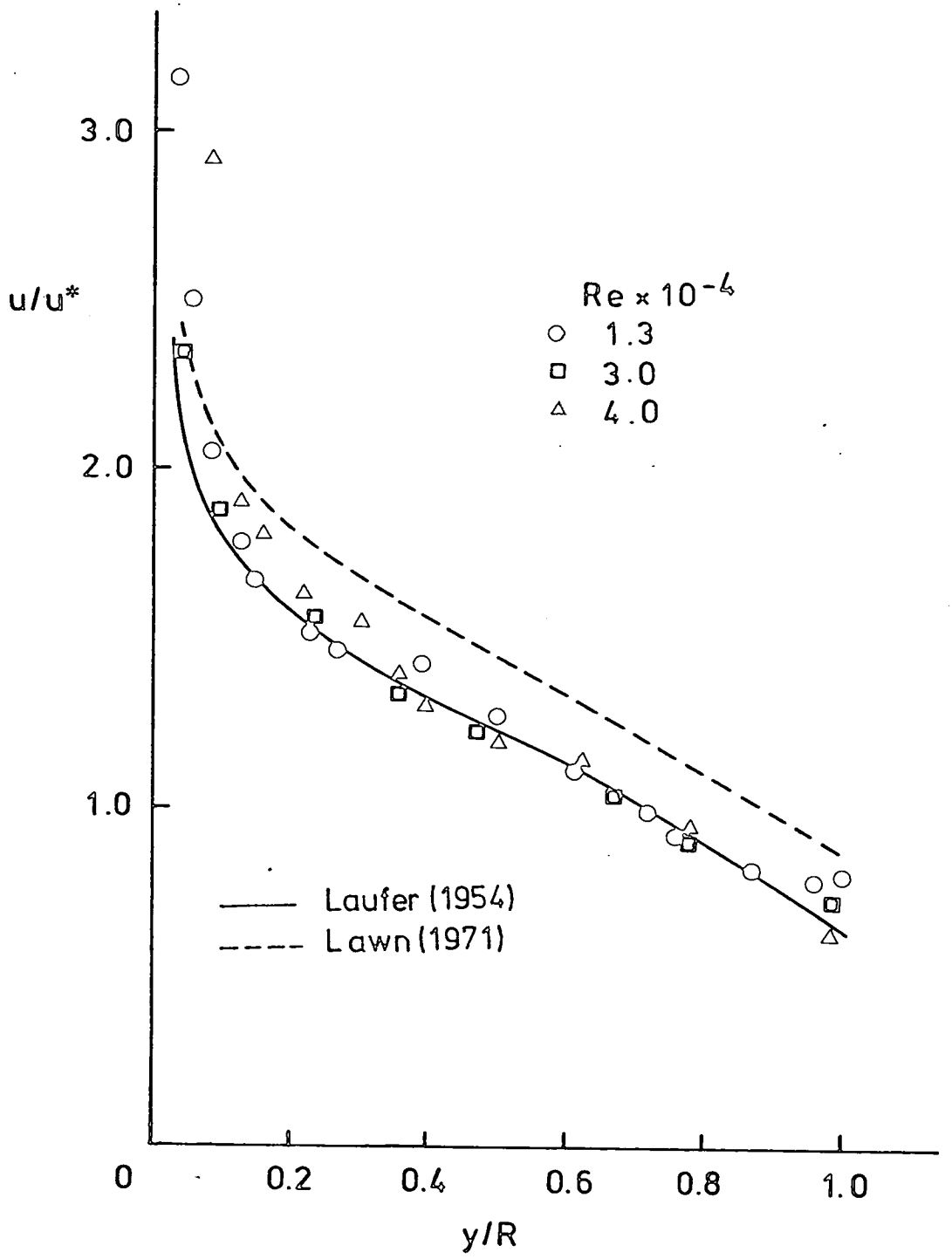

Fig 3.3 Turbulent Intensity Distribution

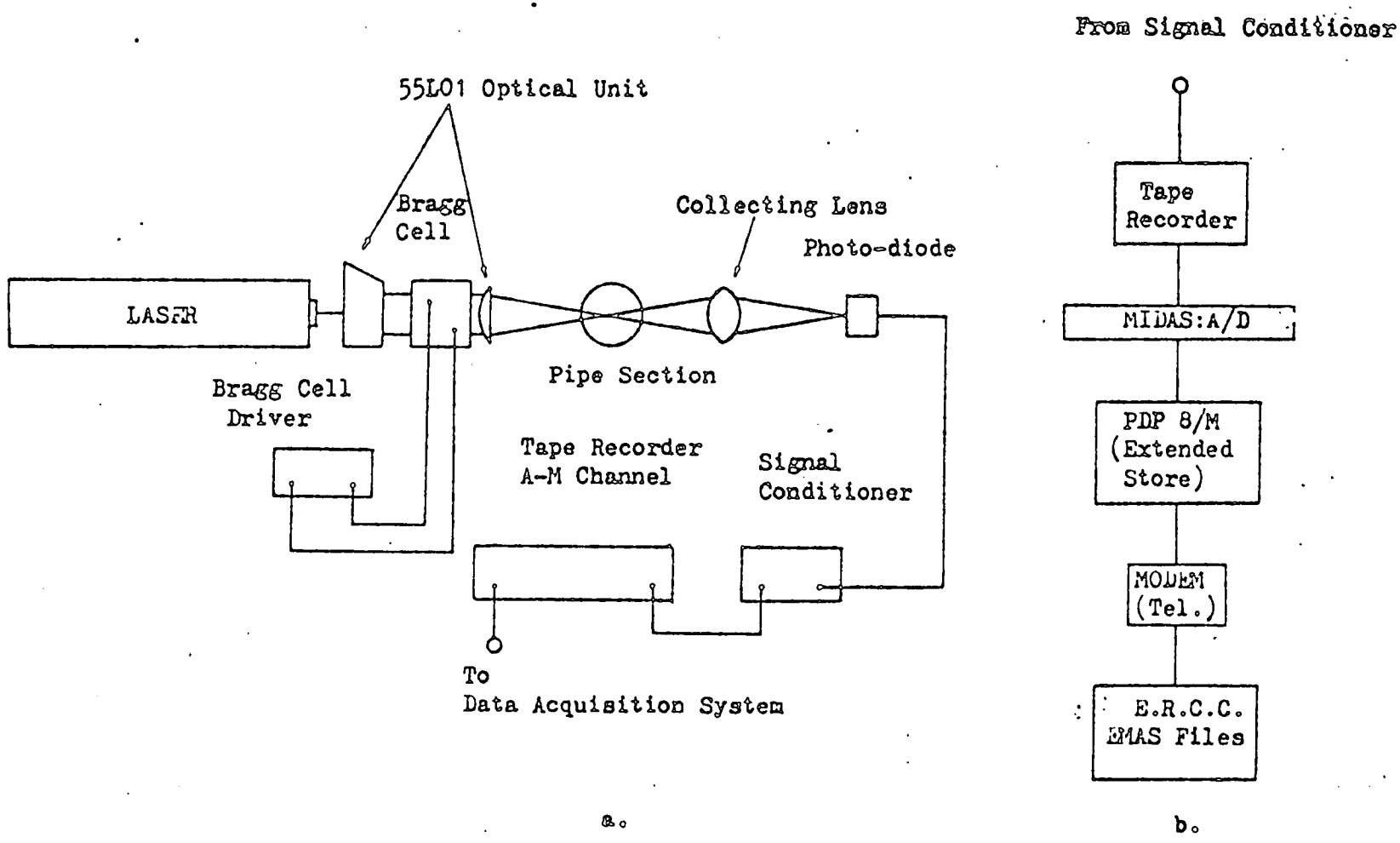

Fig 3.4 a) Schematic Diagram of the LDA for Transverse Measurement

b) Data Acquisition System

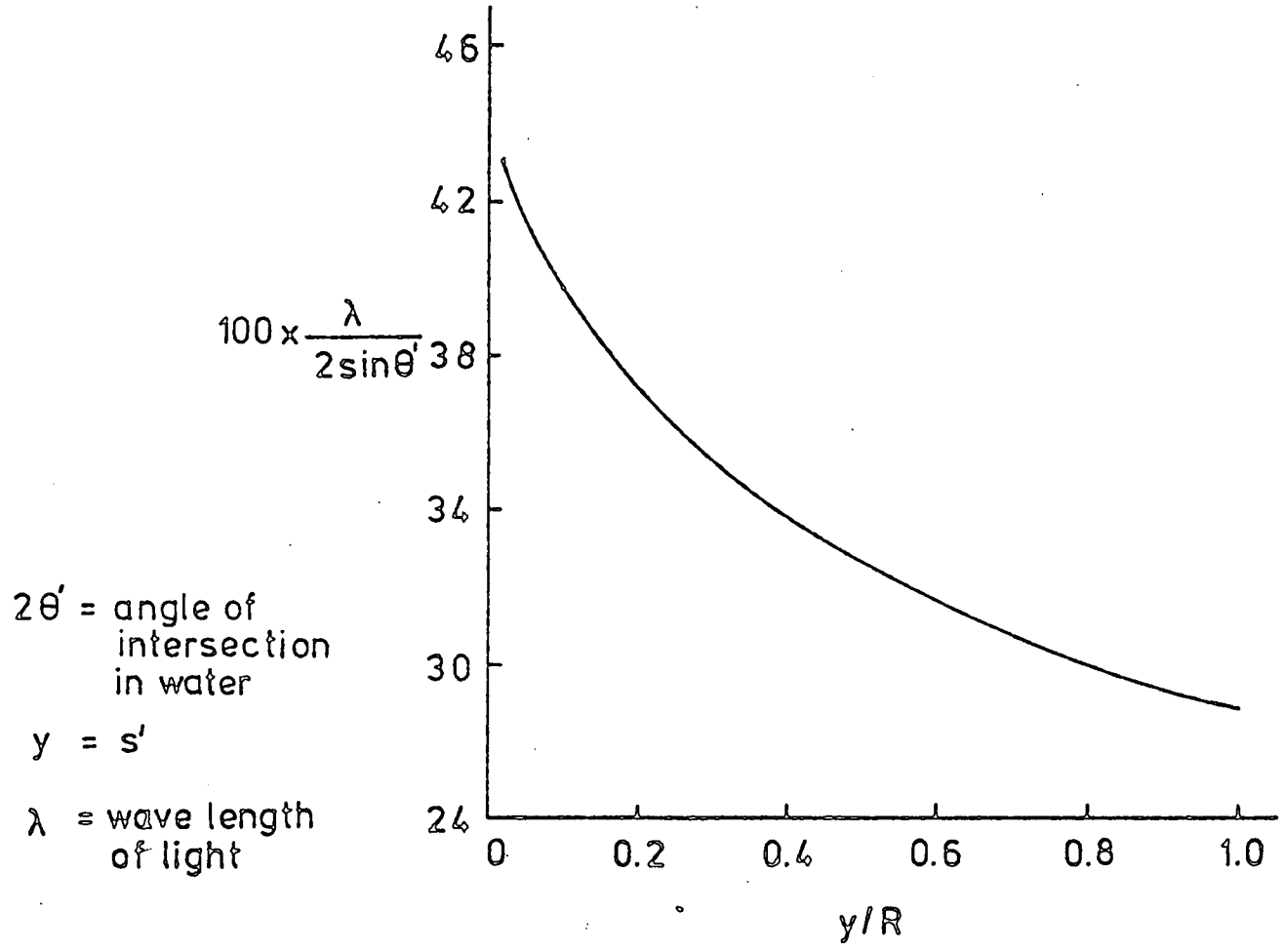

Fig 3.5 Calibration Curve relating θ' to s'

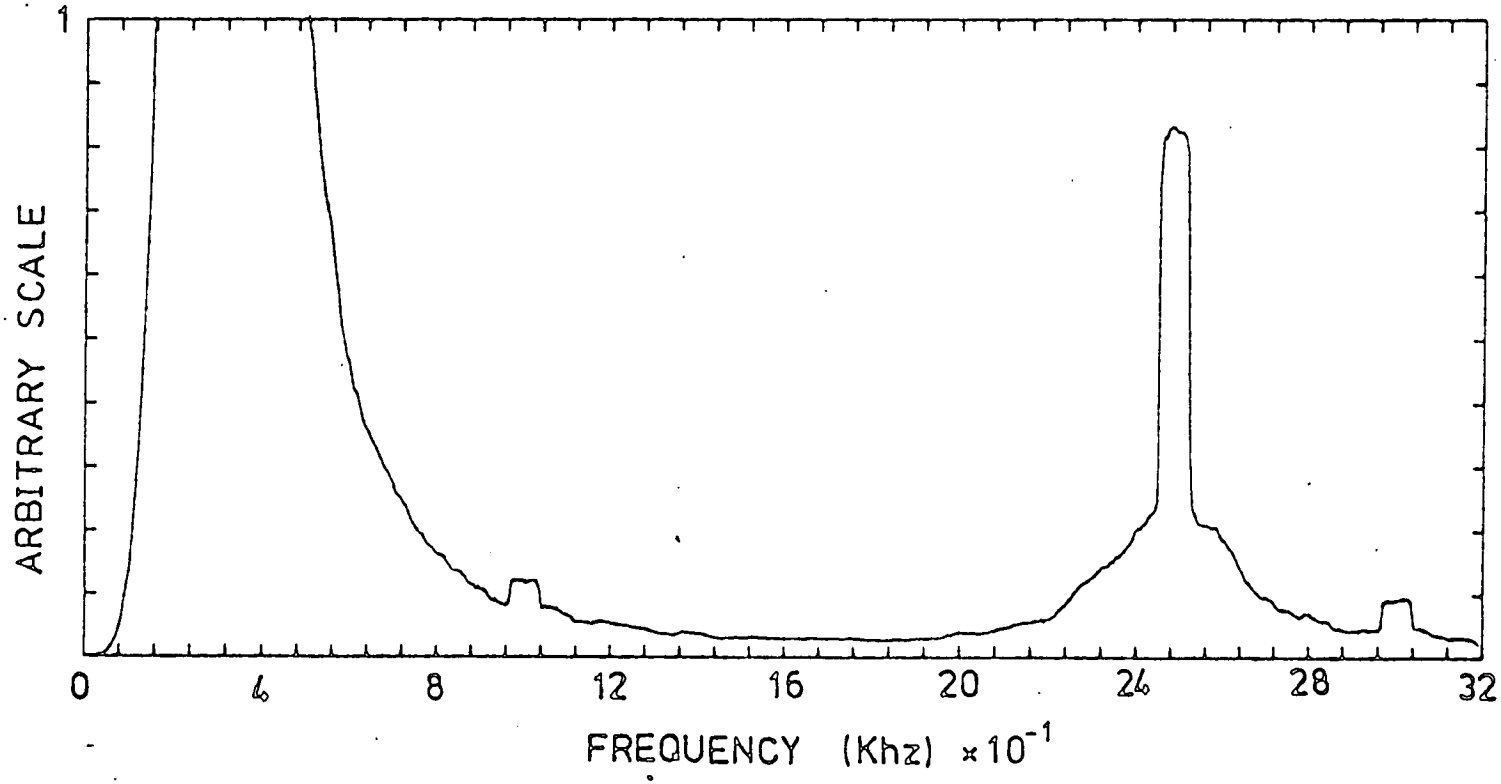

Fig 3.6 Typical Spectrum of the Doppler Signal for Transverse Measurements

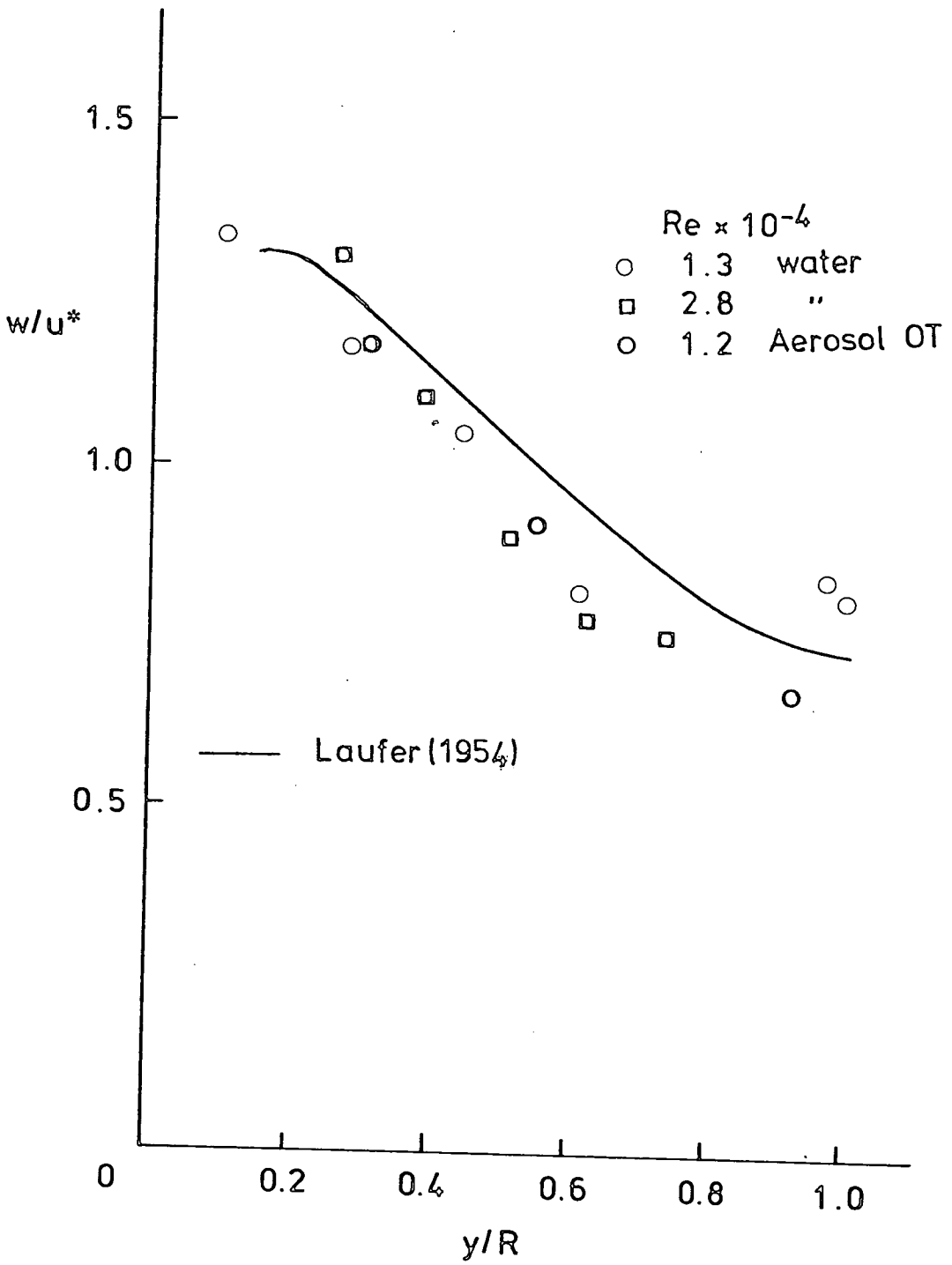

Fig 3.7 Transverse Turbulent Intensity Distribution

```
%BEGIN
%EXTERNALROUTINESPEC SPECT (%INTEGERNAME L %INTEGER N,P,SKIP %C
 %LONGREAL OFFSET ,SCALE %LONGREALNAME F ,KNOUGHT %INTEGER MARKER,S)
%EXTERNALROUTINESPEC MODI(%INTEGER SEGNO,POWER,LECOR,INST)
%EXTERNALROUTINESPEC SEGAV (%INTEGER INSQ,ASTREAM,BSTREAM, %C
LENGTH,SEGMENTS,MOVAV %LONGREAL DK,KNOUGHT)
%EXTERNALROUTINESPEC DEFINE (%STRING (63) S)
%STRING (63) INST,SQTEMP, OUTA,OUTB
%INTEGER SKIP,SEG,MOV,L,SNCODE,REDFACT,P
%LONGREAL KNOUGHT,SF,SCALE,OFFSET
SQTEMP='SQTEMP'
!***** SET CONTROL PARAMS NEXT LINE*****
SKIP=0;SEG=3; MOV=11;L=1024;P=13;SNCODE=2;REDFACT=8 ;SF=40000
READSTRING(INST) ;READSTRING(OUTA) ;READSTRING(OUTB)
READ(SCALE) ;READ(OFFSET)
DEFINE('ST66,',INST)
DEFINE('SQSS,',SQTEMP)
DEFINE('ST22,',OUTA)
DEFINE('ST33,',OUTB)
MODI(SEG,P,L,66)
SPECT(L,SEG,P,SKIP,OFFSET,SCALE,SF,KNOUGHT,SNCODE,REDFACT)
SEGAV(55,22,33,L,SEG,MOV,KNOUGHT,SF)
%ENDOFPROGRAM
```

Fig 3.8 MASTER Program

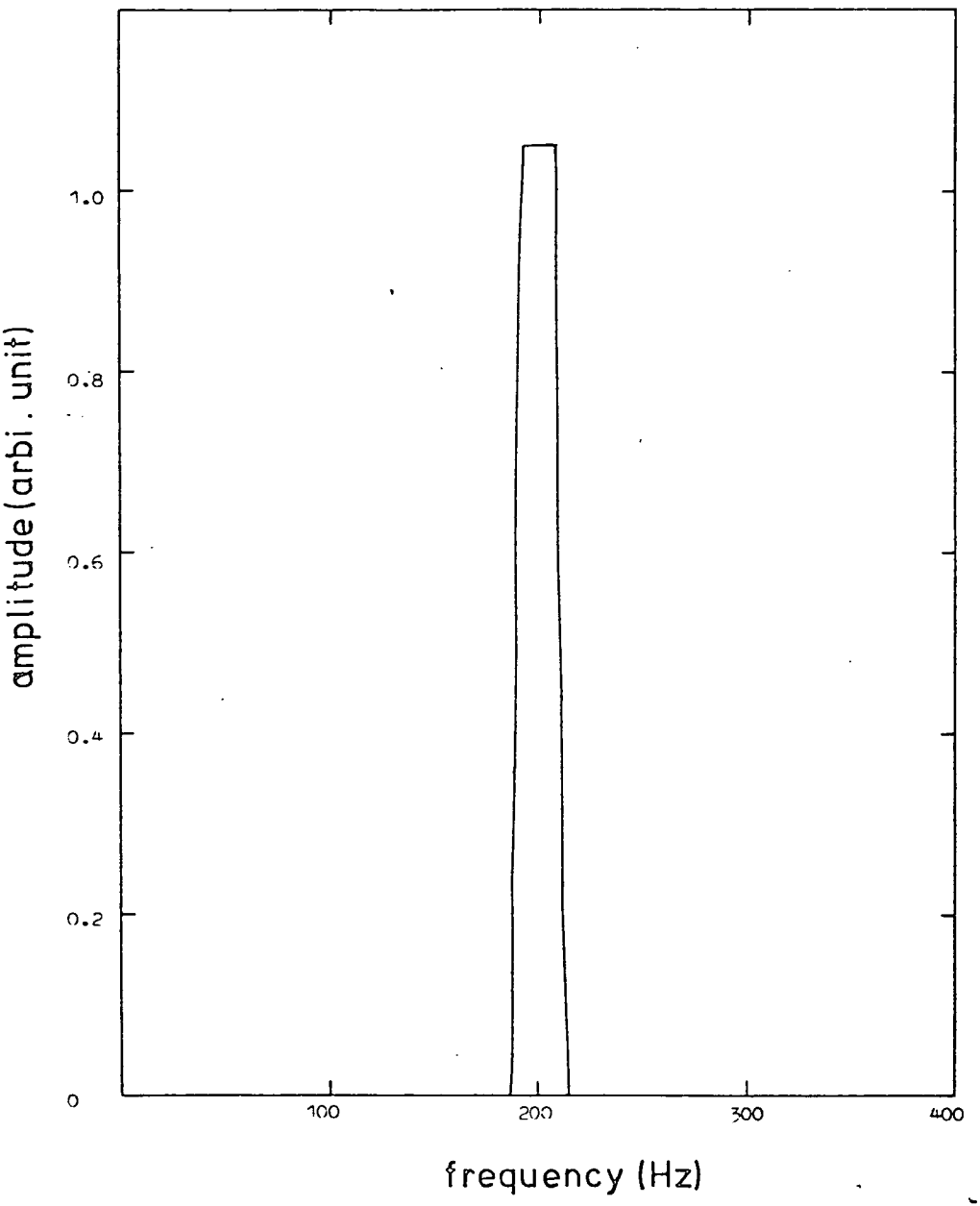

Fig 3.9 A spectrum of a Harmonic Wave

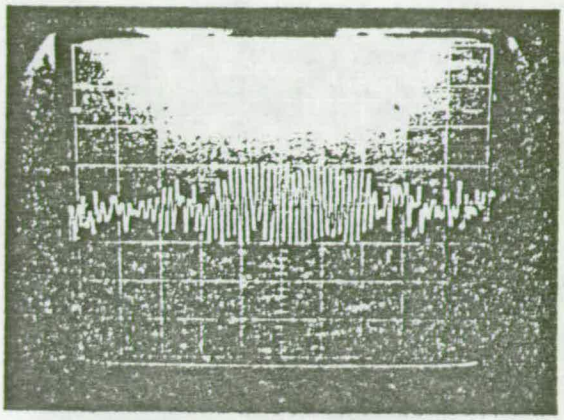

100 ppm milk

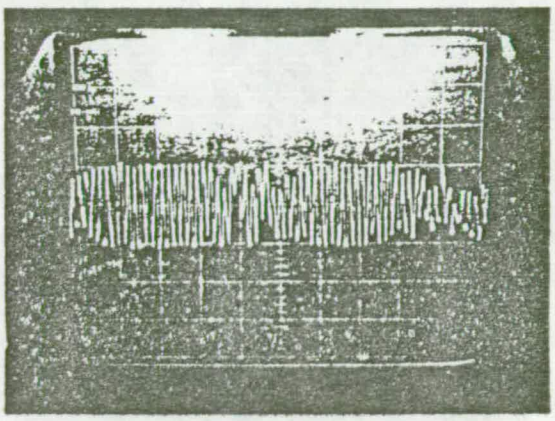

200 ppm milk

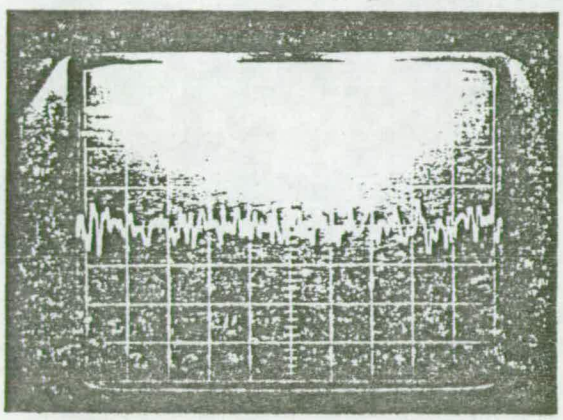

back-ground noise

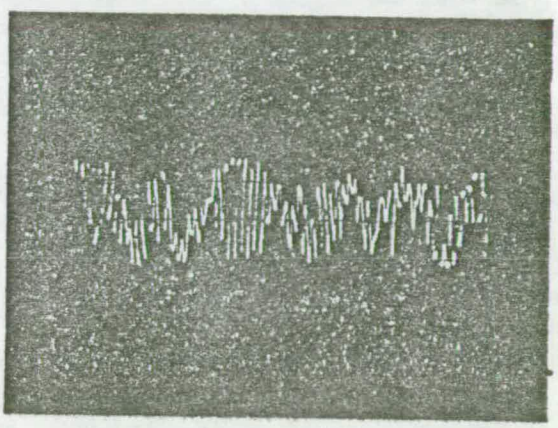

Aerosol OT (0.5%)

Fig 4.1 all at centre, time base = 10 μS/cm.

Re = 1.4×10^4

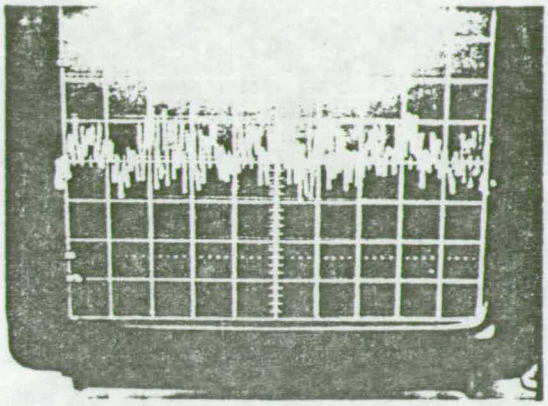

no milk

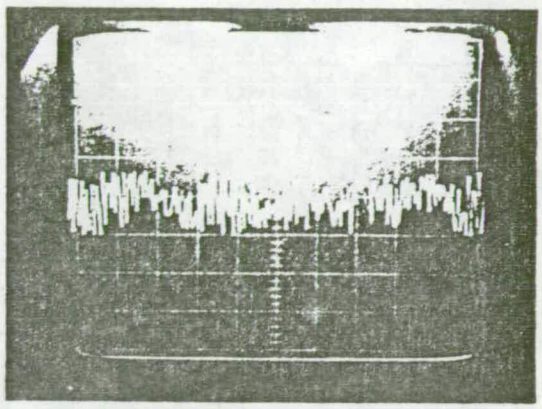

100 ppm milk

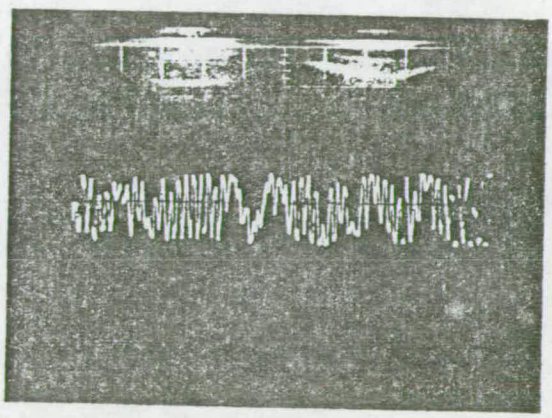

200 ppm milk

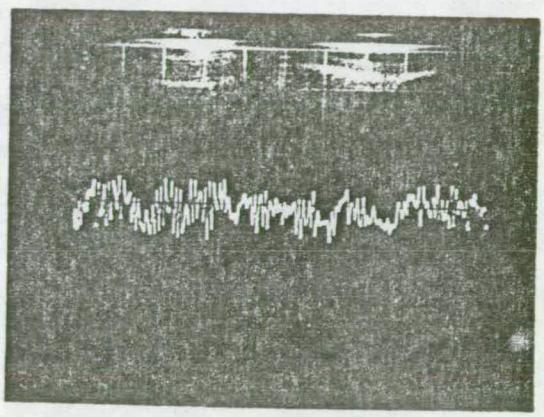

100 ppm milk and
150 ppm polymer (AP30)

Fig 4.2 all for 300 ppm fibre suspension with 0.5% Aerosol OT solution, all at centre, time base = 10 μS/cm. Re = 1.4×10^4

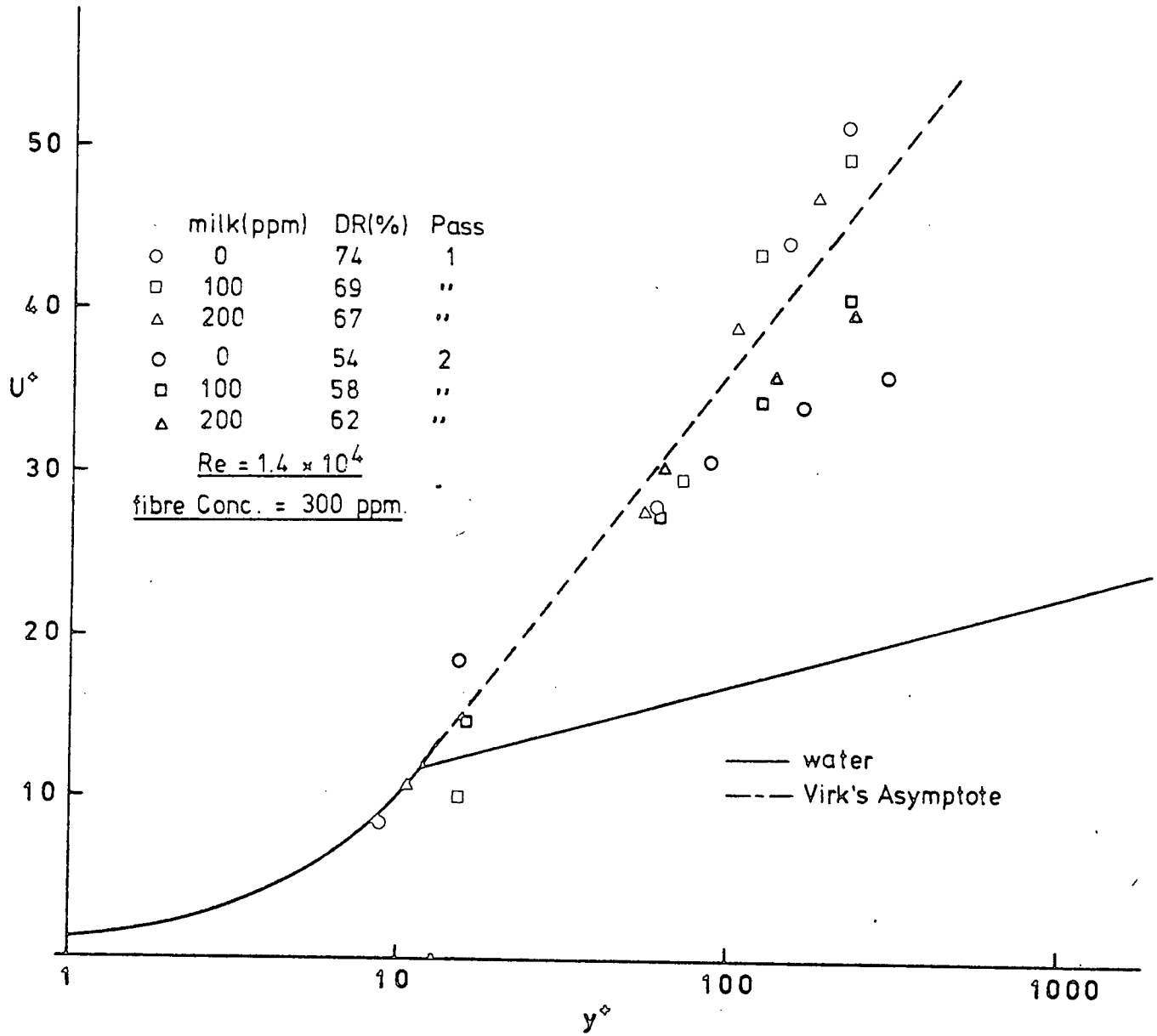

Fig 4.3 The Mean Velocity Profiles

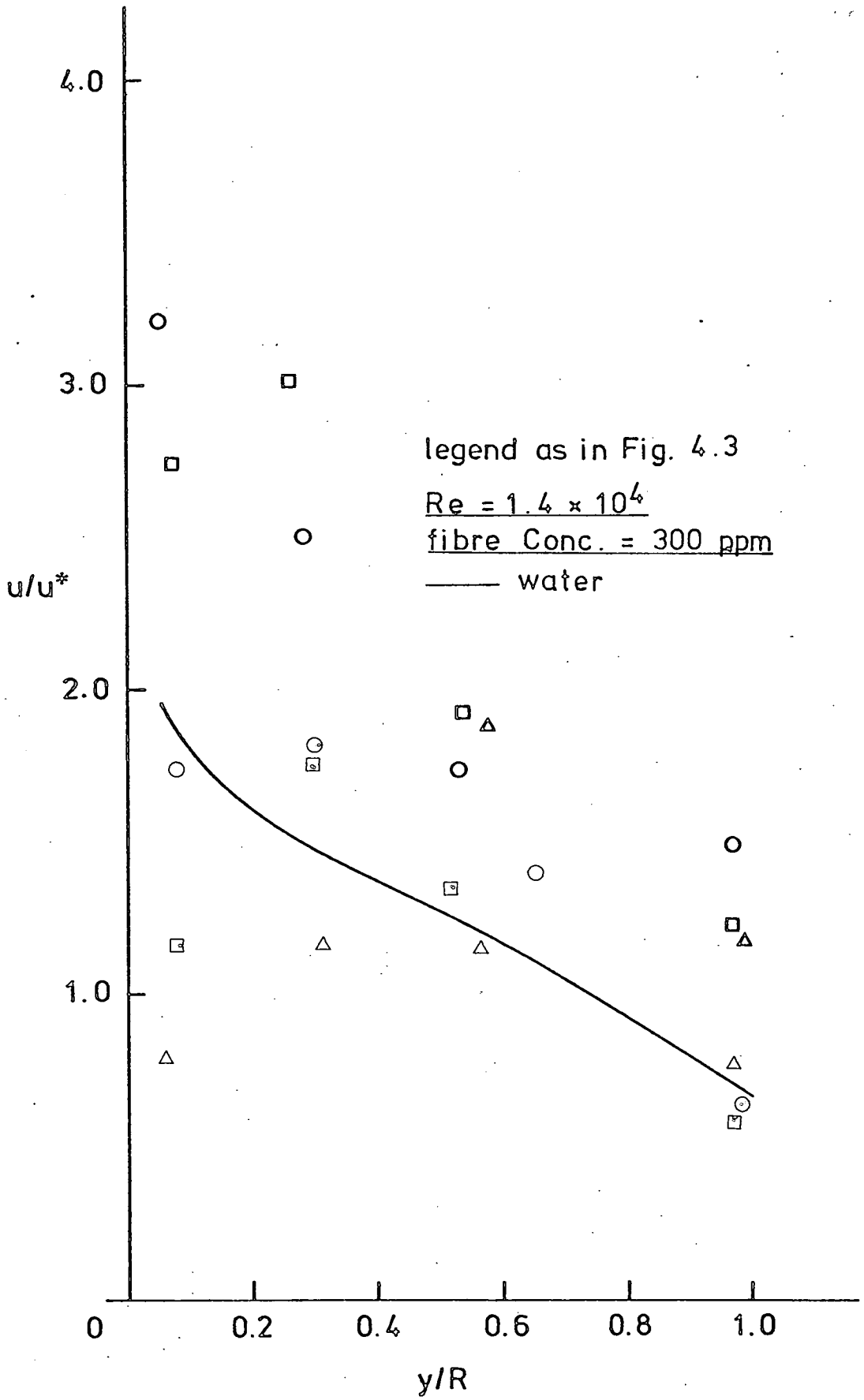

Fig 4.4 The Streamwise Intensity Distributions

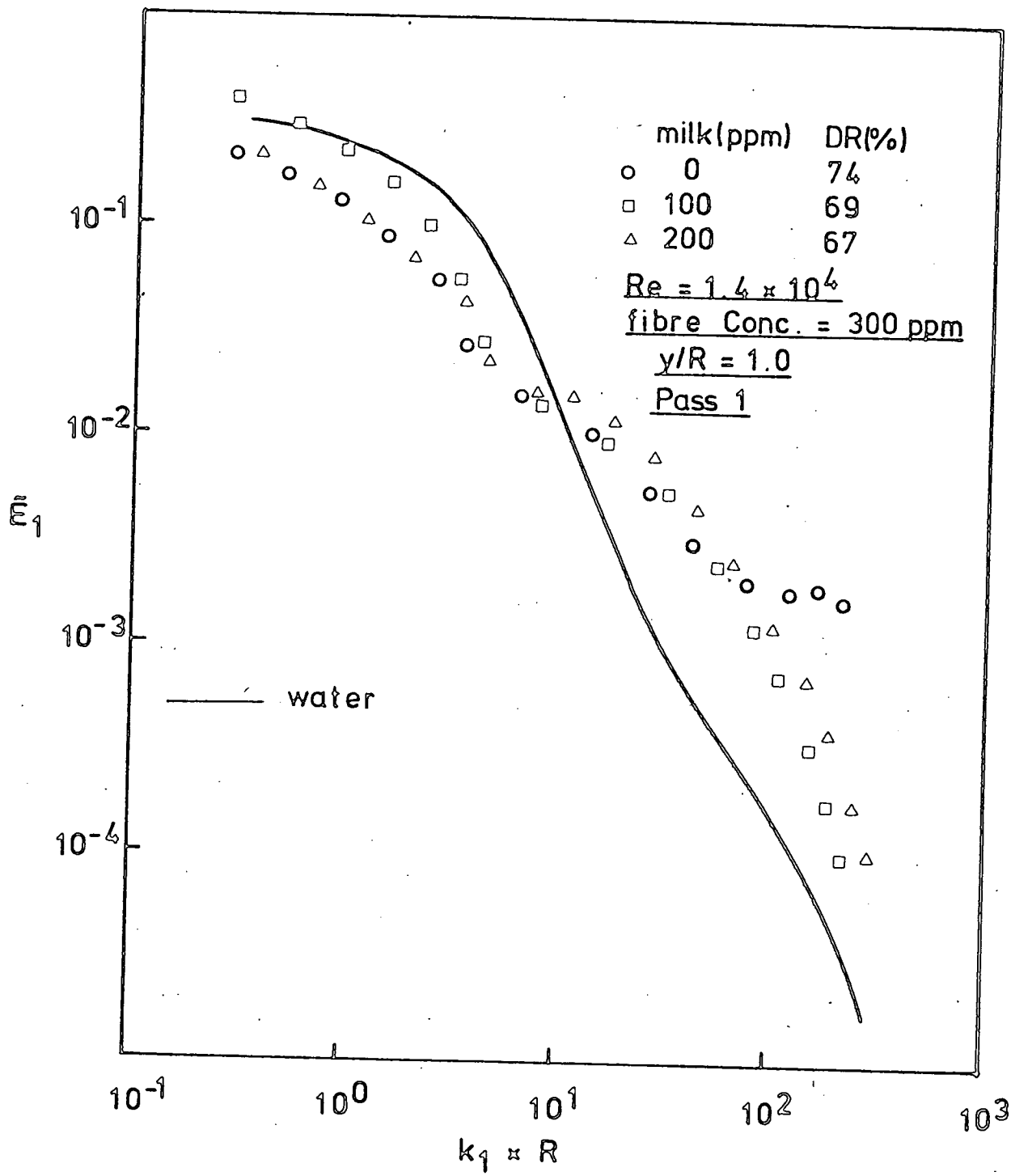

Fig 4.5 The Energy Spectra

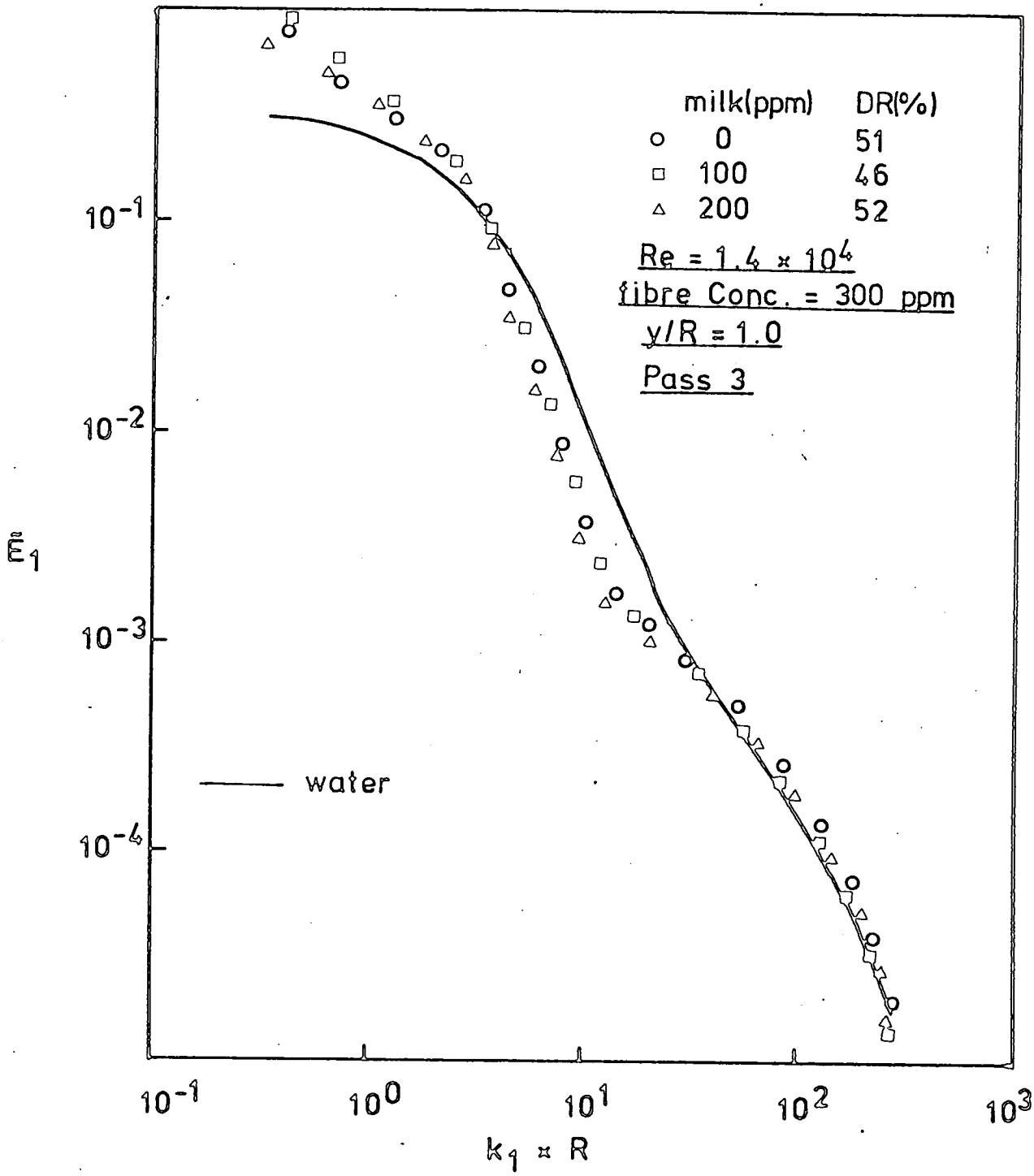

Fig 4.6 The Energy Spectra

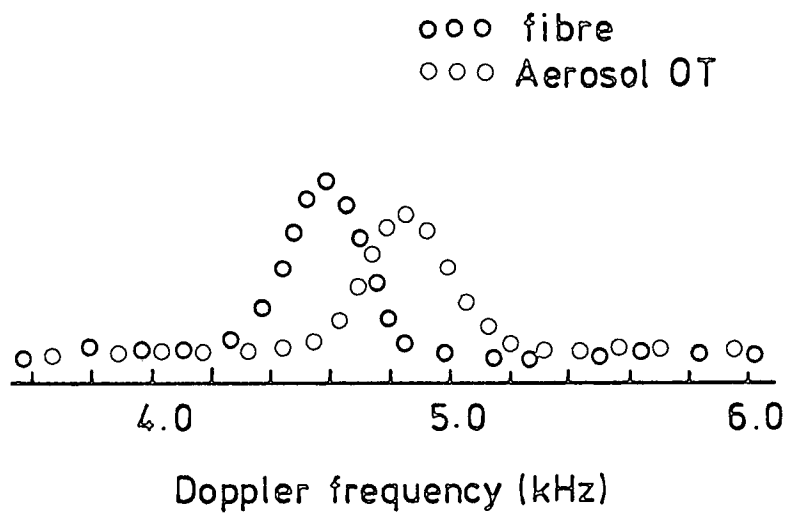

Fig 4.7 Spectra of Photo-current

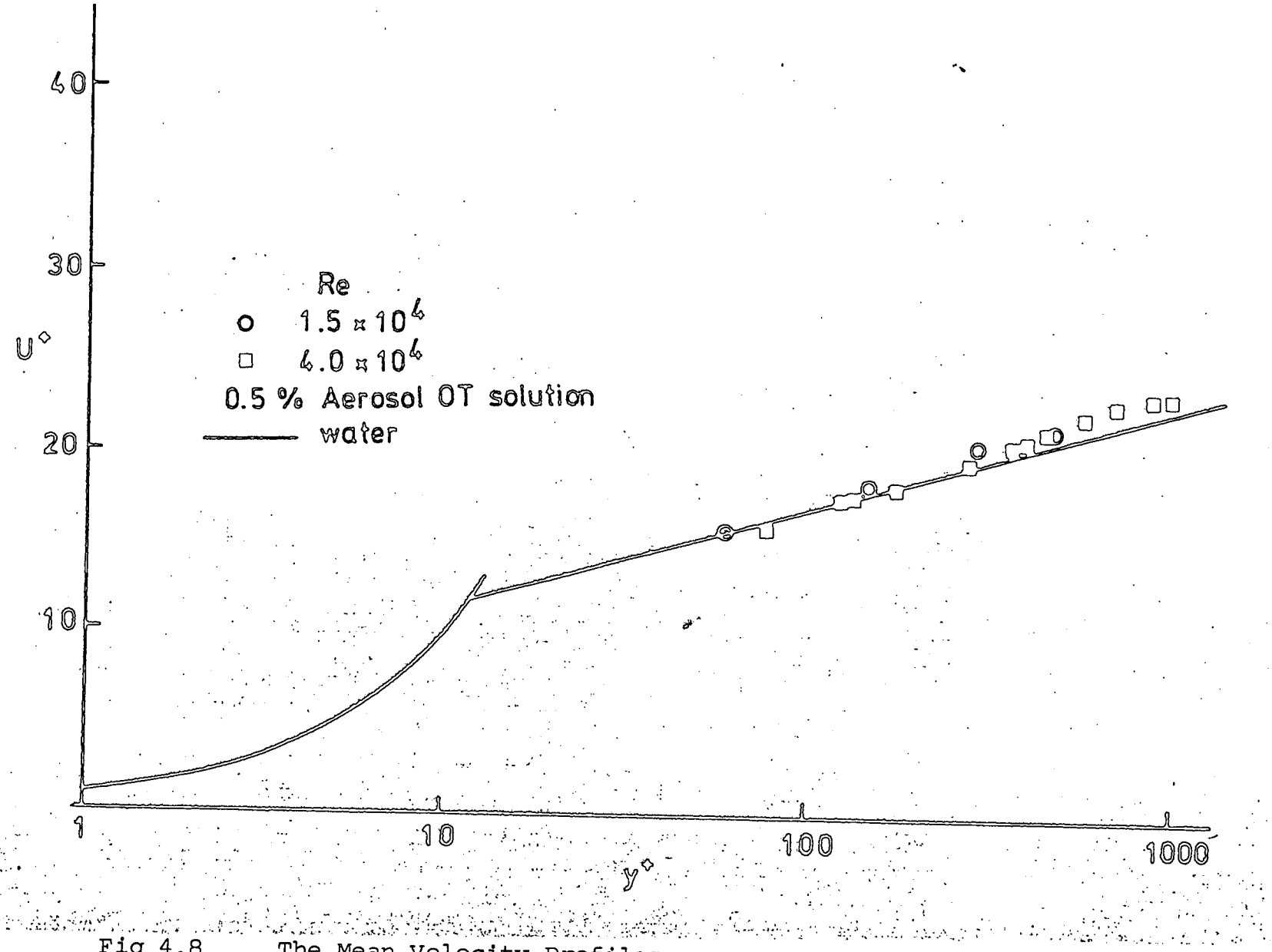

Fig 4.8 The Mean Velocity Profiles

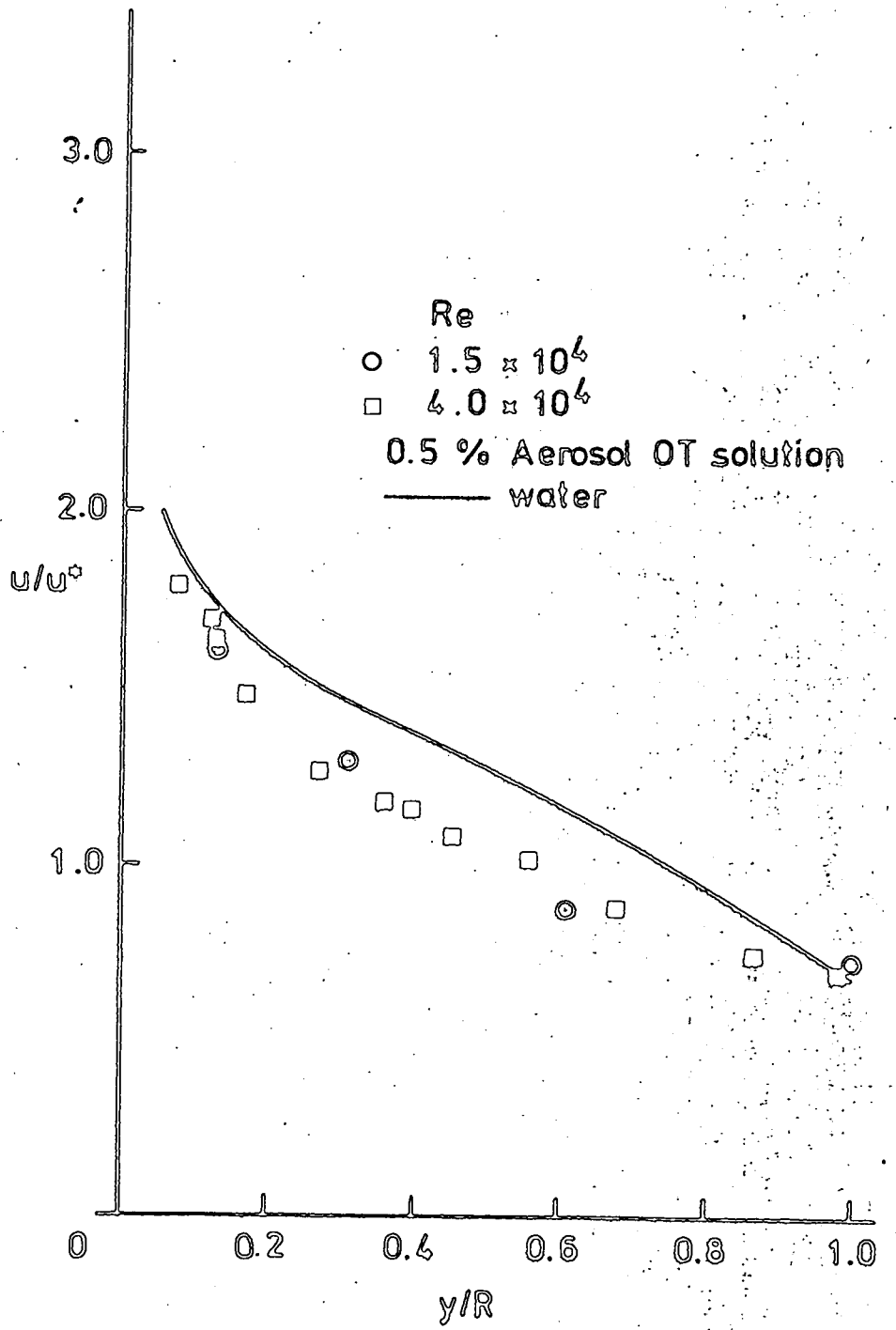

Fig 4.9 The Streamwise Intensity Distributions

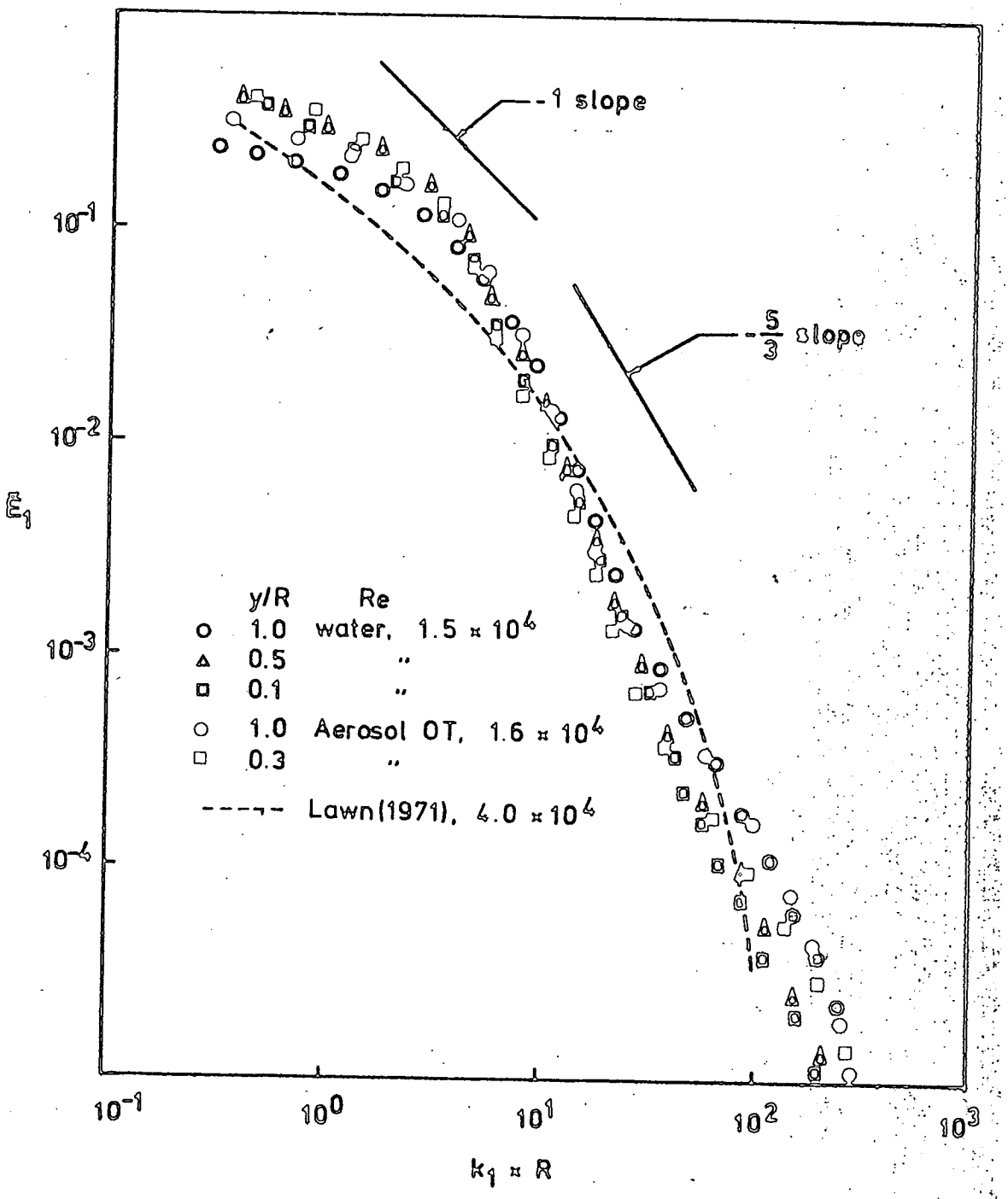

Fig 4.10 The Energy Spectra

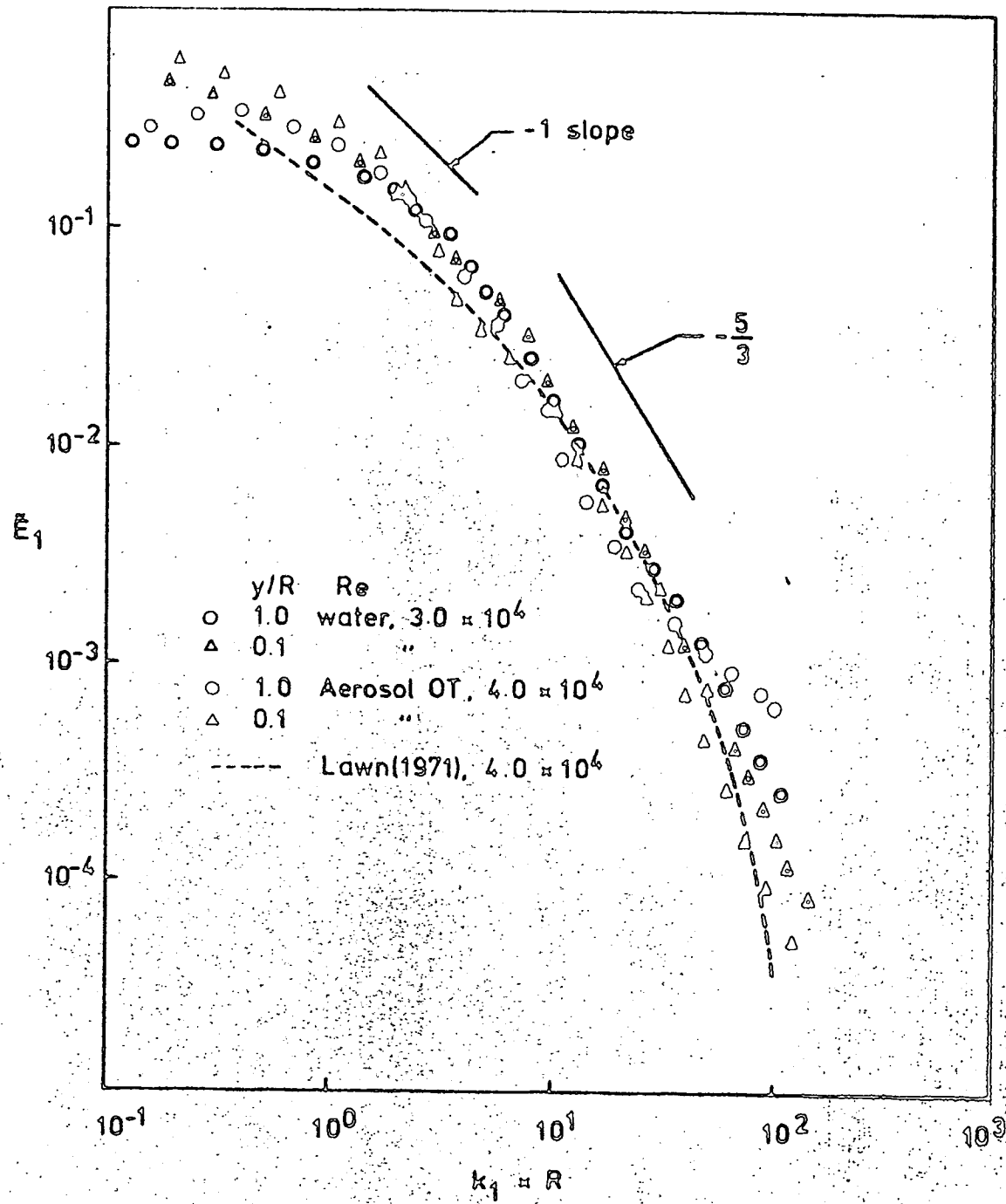

Fig 4.11 The Energy Spectra

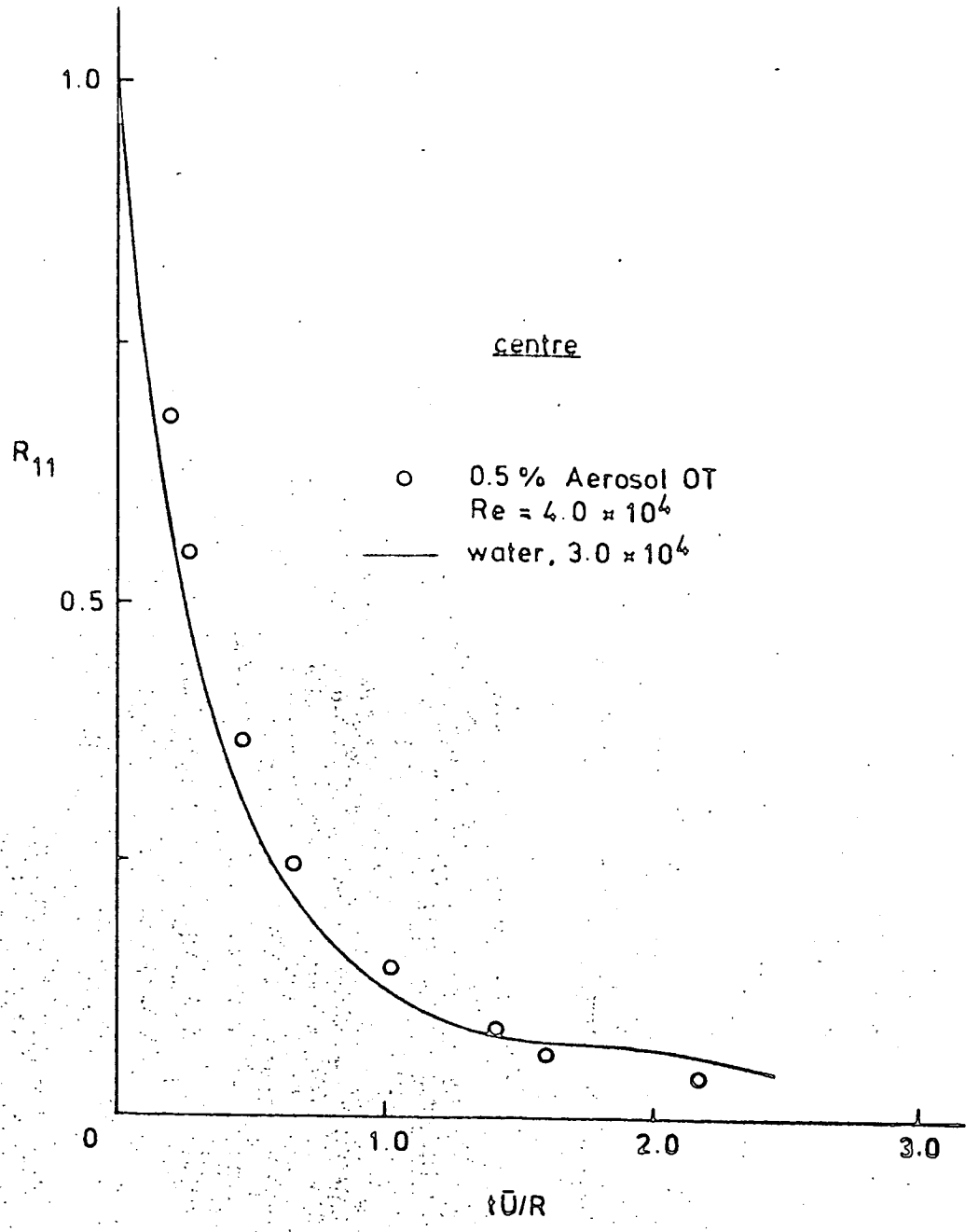

Fig 4.12 The Auto-correlations

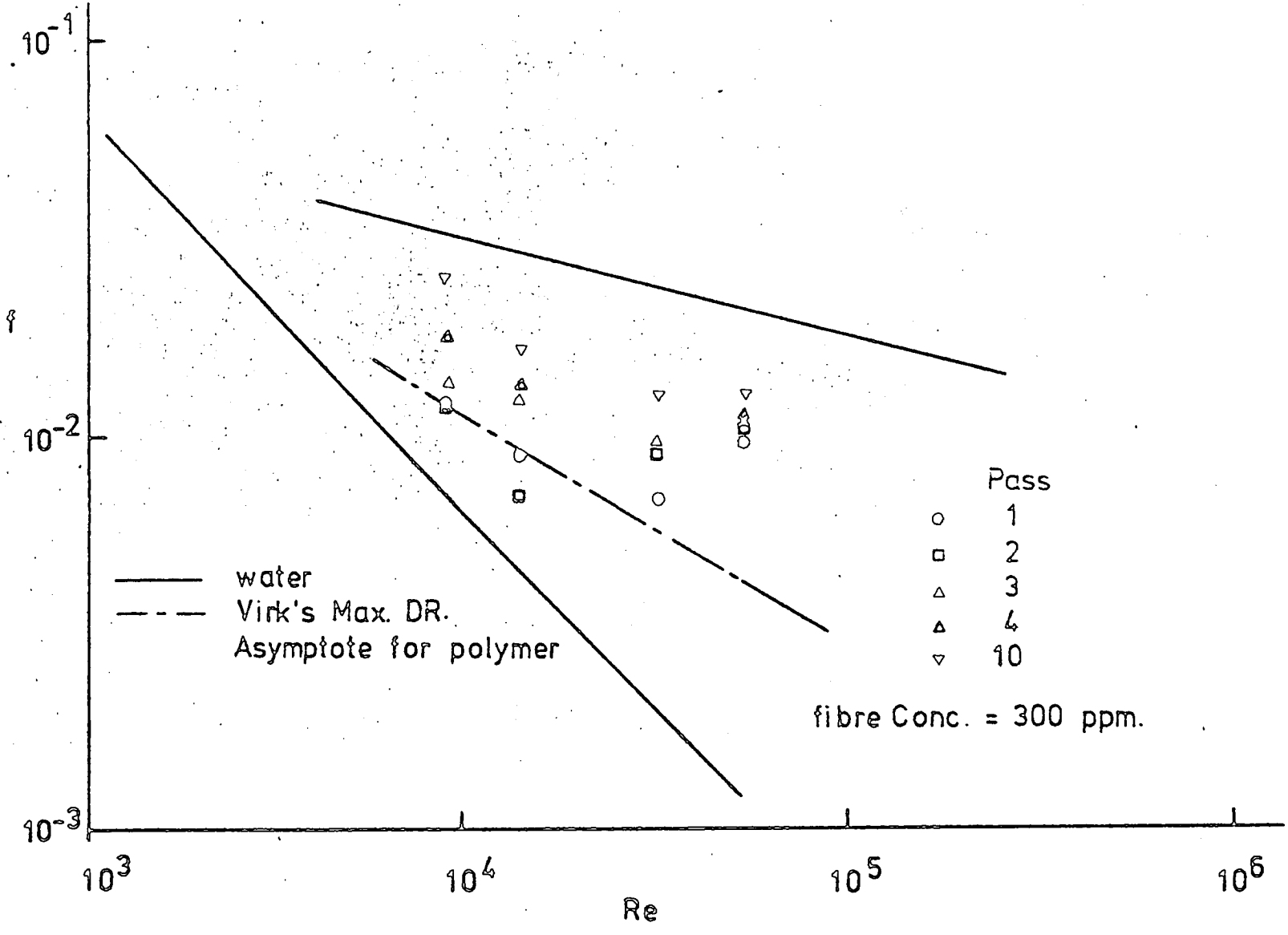

Fig 4.13 Friction Factor versus Reynolds Number

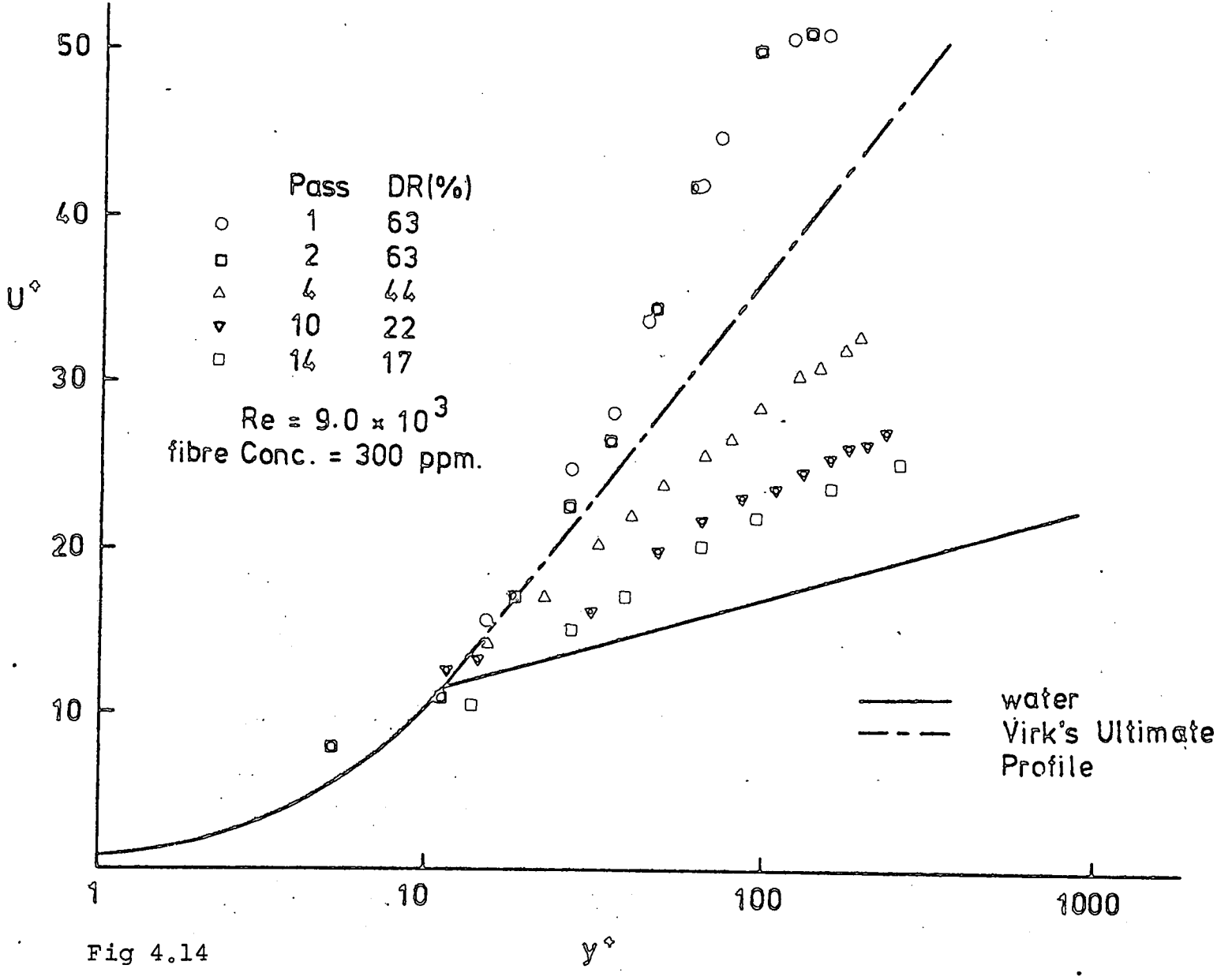
50
40
30
20
10
U+
Pass DR(%)
1 63
2 63
4 44
10 22
14 17
Re = 9.0 x 10^3
fibre Conc. = 300 ppm.
water
Virk's Ultimate Profile
1
10
100
1000
y+

Fig 4.14

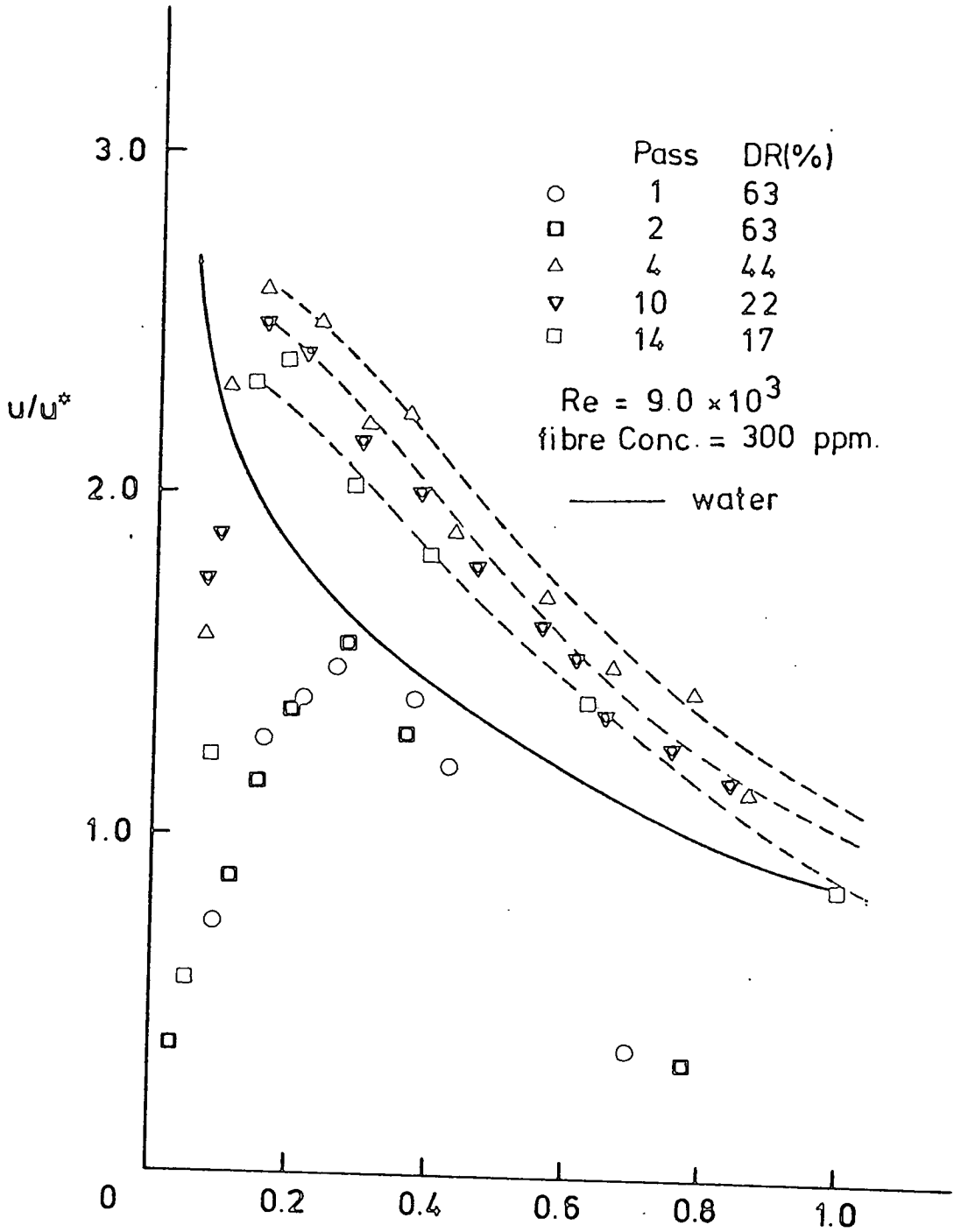
3.0
2.0
1.0
0
u/u*
0.2
0.4
0.6
0.8
1.0
y/R
Pass
DR(%)
1
63
2
63
4
44
10
22
14
17
Re = 9.0 x 10^3
fibre Conc. = 300 ppm.
water

Fig 4.15

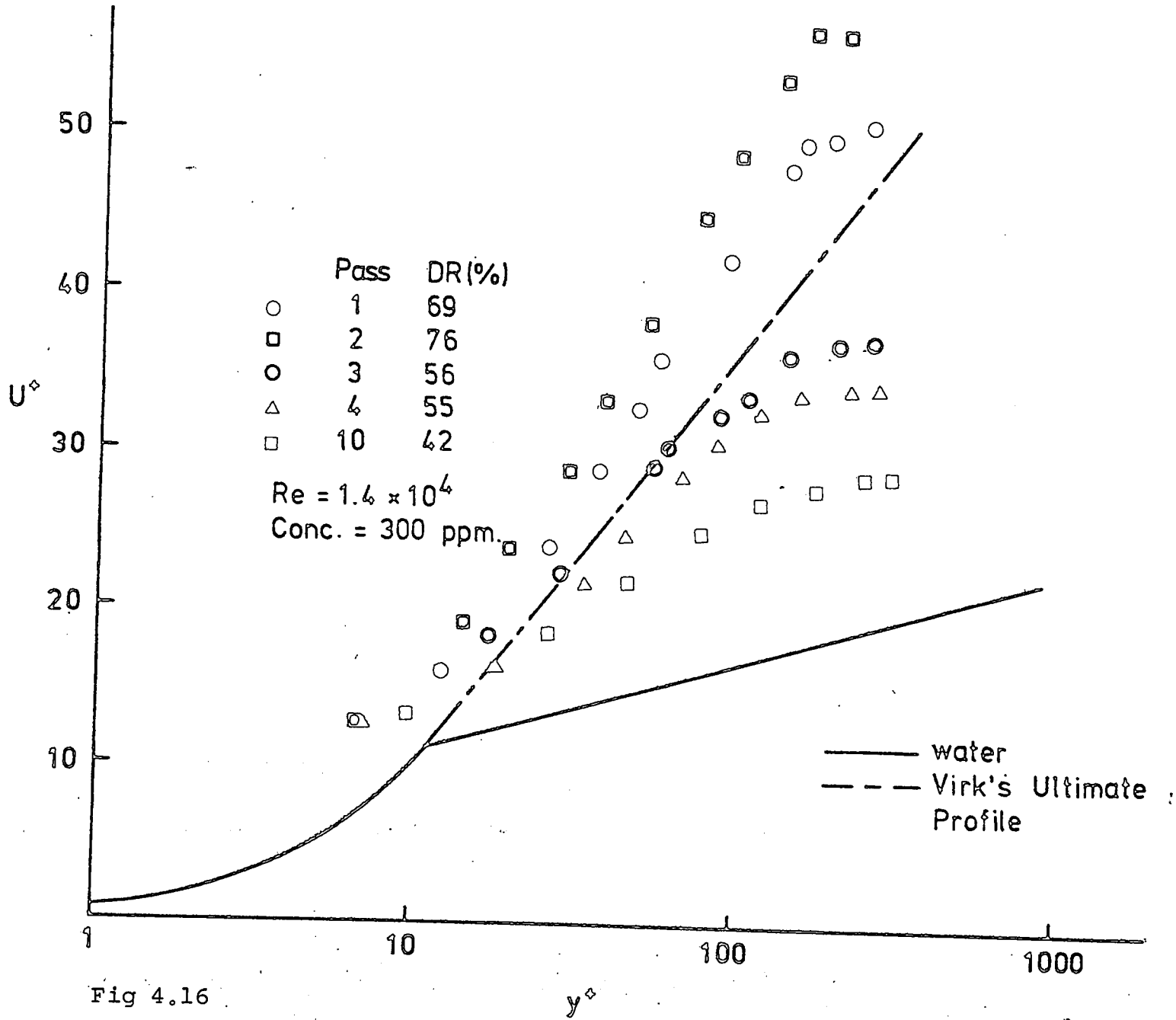
50
40
30
20
10
U+
Pass DR(%)
1 69
2 76
3 56
4 55
10 42
Re = 1.4 x 10^4
Conc. = 300 ppm.
water
Virk's Ultimate Profile
1
10
100
1000
y+

Fig 4.16

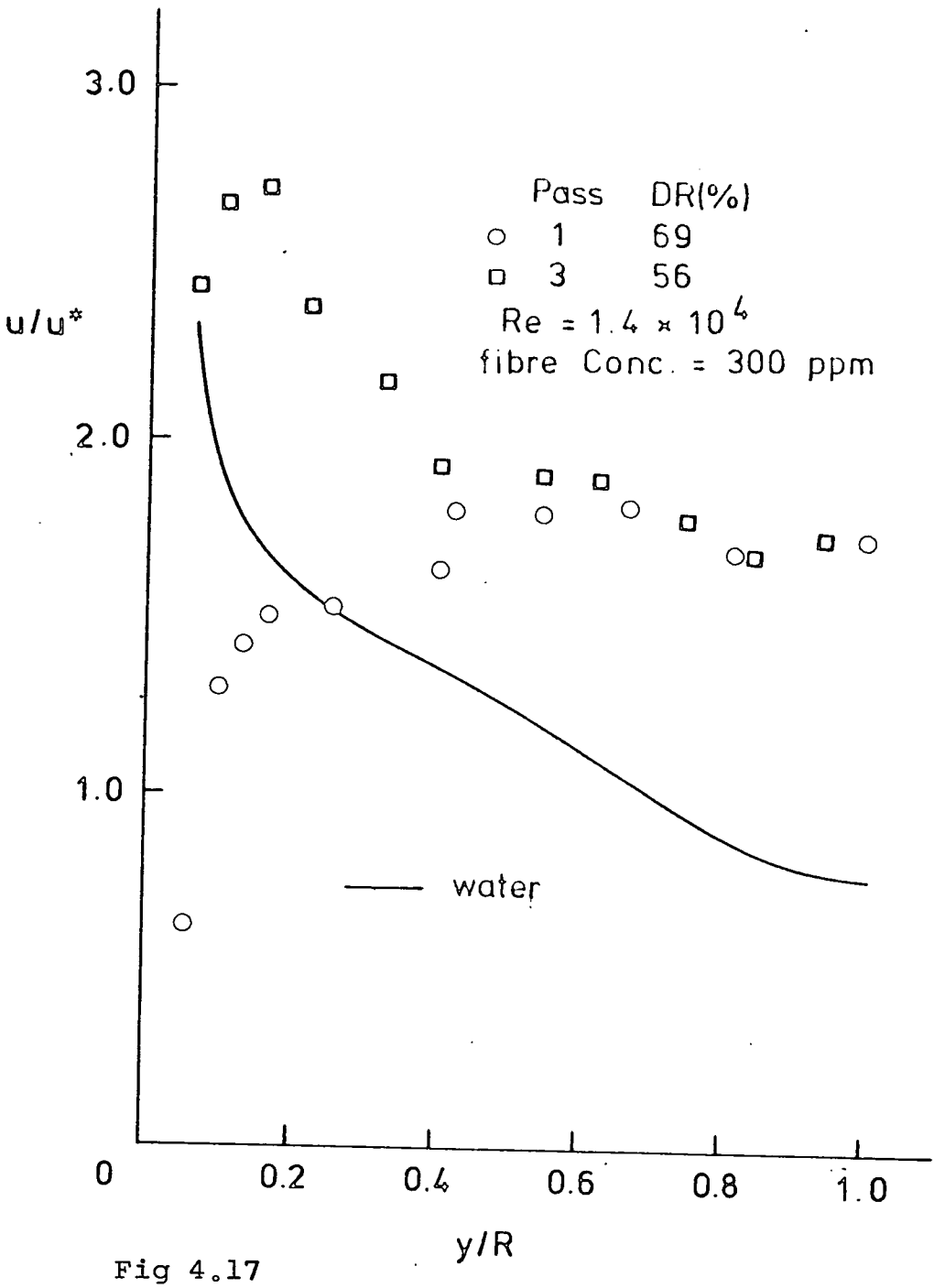
3.0
2.0
1.0
0
u/u*
Pass DR(%)
1 69
3 56
Re = 1.4 × 10^4
fibre Conc. = 300 ppm
water
0.2
0.4
0.6
0.8
1.0
y/R

Fig 4.17

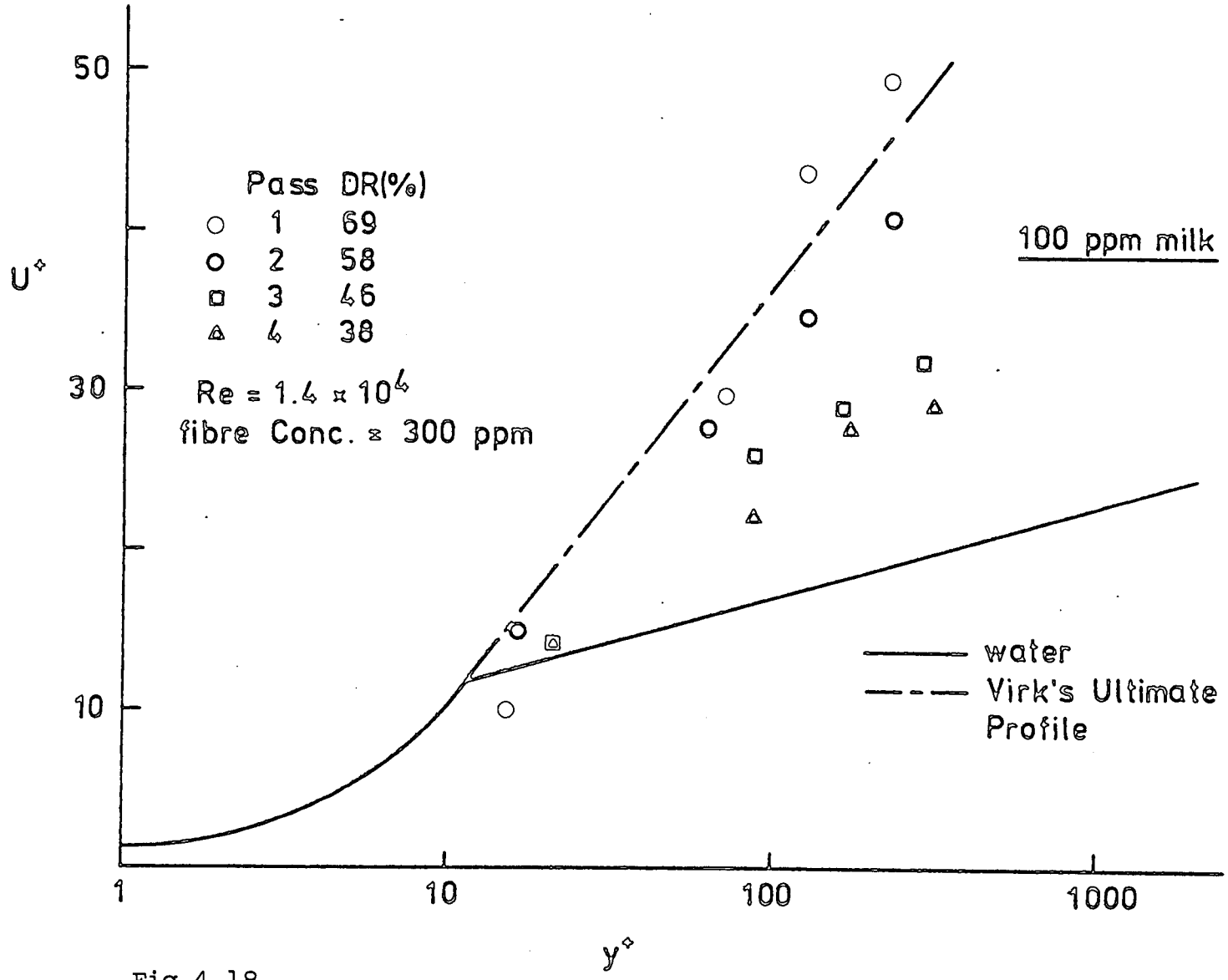
50
30
10
U+
Pass DR(%)
1 69
2 58
3 46
4 38
Re = 1.4 x 10^4
fibre Conc. = 300 ppm
100 ppm milk
water
Virk's Ultimate Profile
1
10
100
1000
y+

Fig 4.18

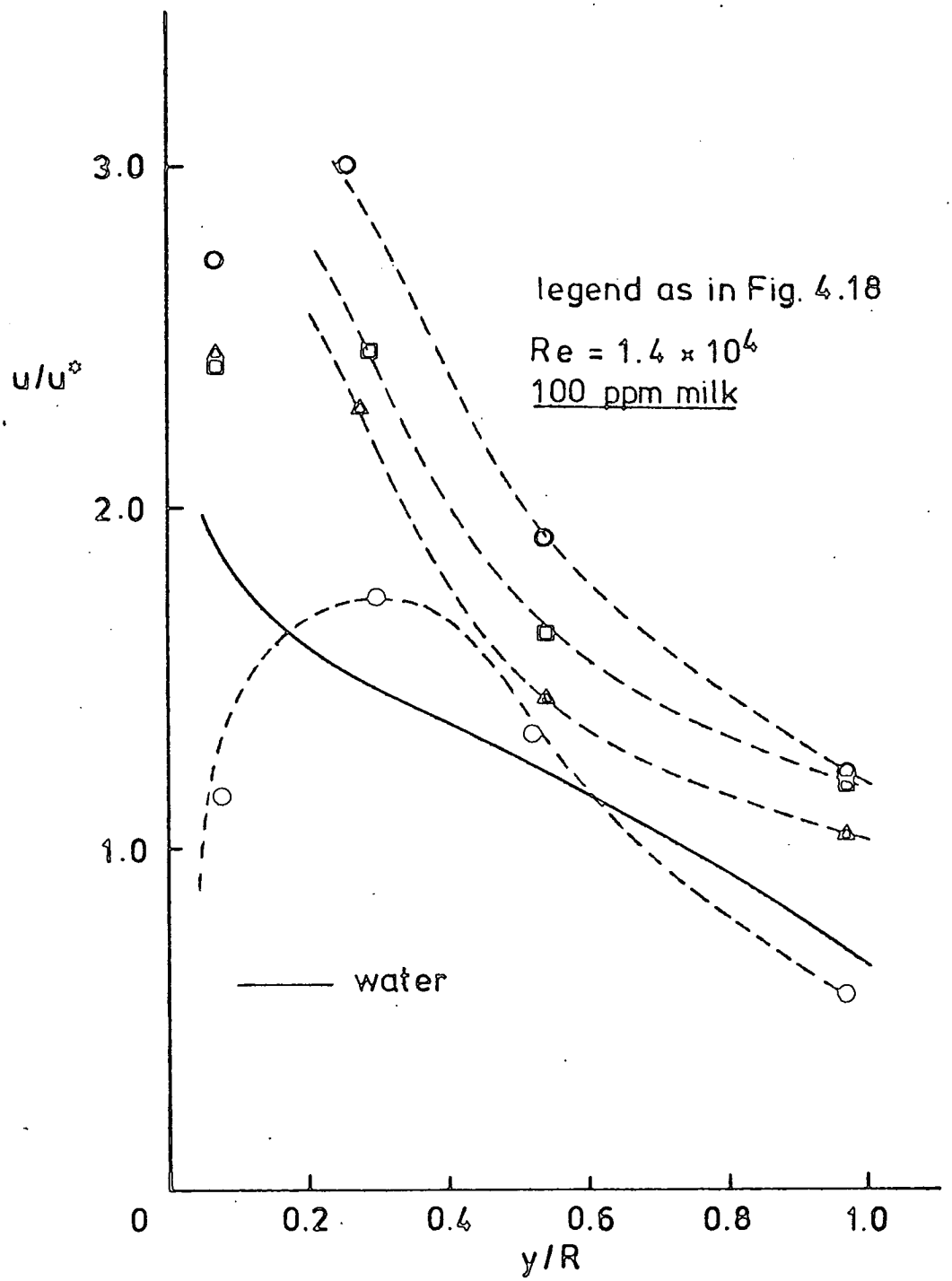
3.0
2.0
1.0
u/u*
legend as in Fig. 4.18
Re = 1.4 × 10^4
100 ppm milk
water
0
0.2
0.4
0.6
0.8
1.0
y/R

Fig 4.19

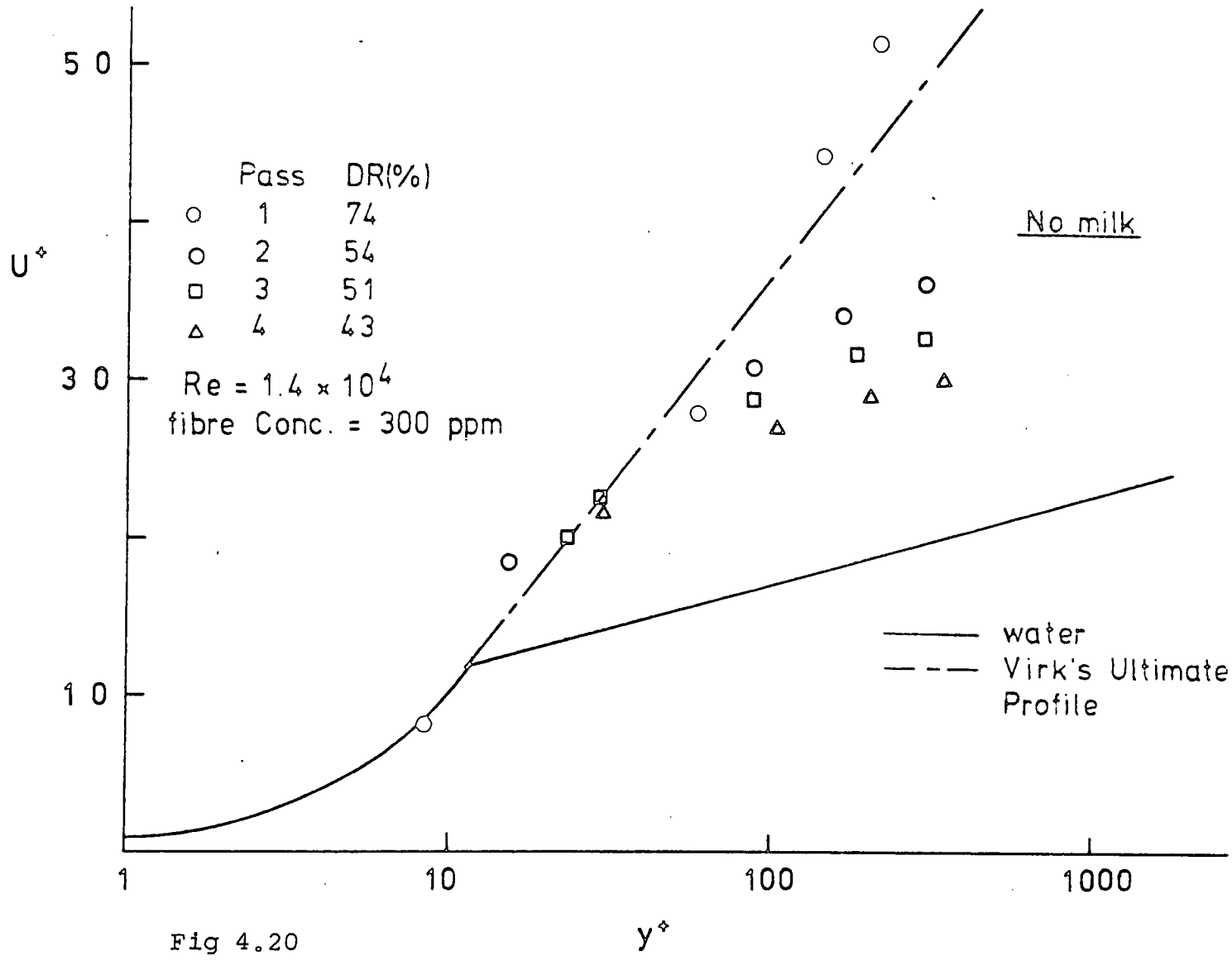
5 0
3 0
1 0
U+
Pass DR(%)
1 74
2 54
3 51
4 43
Re = 1.4 × 10^4
fibre Conc. = 300 ppm
No milk
water
Virk's Ultimate Profile
1
10
100
1000
y+

Fig 4.20

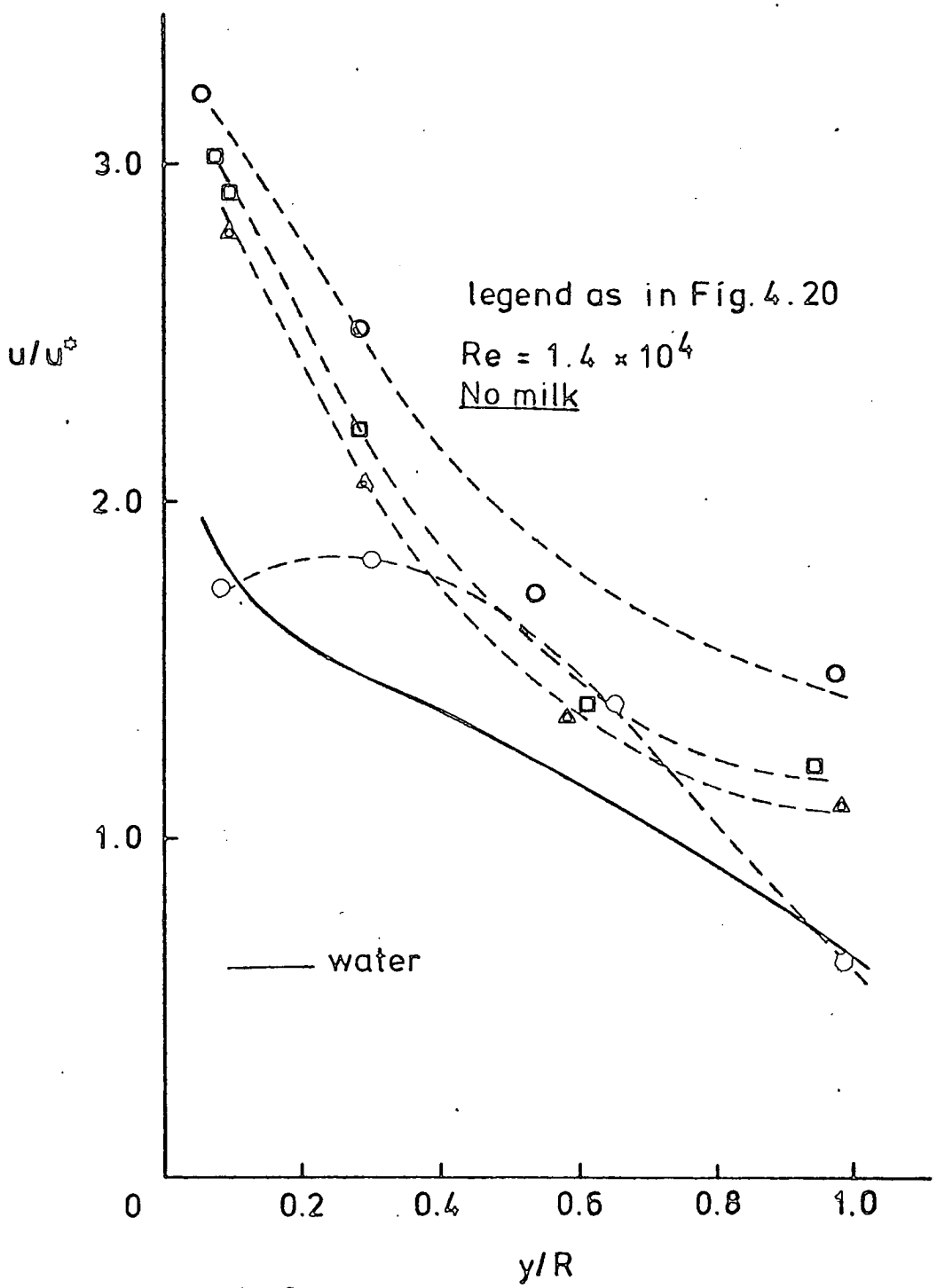
3.0
2.0
1.0
0
u/u*
legend as in Fig. 4.20
Re = 1.4 × 10^4
No milk
water
0.2
0.4
0.6
0.8
1.0
y/R

Fig 4.21

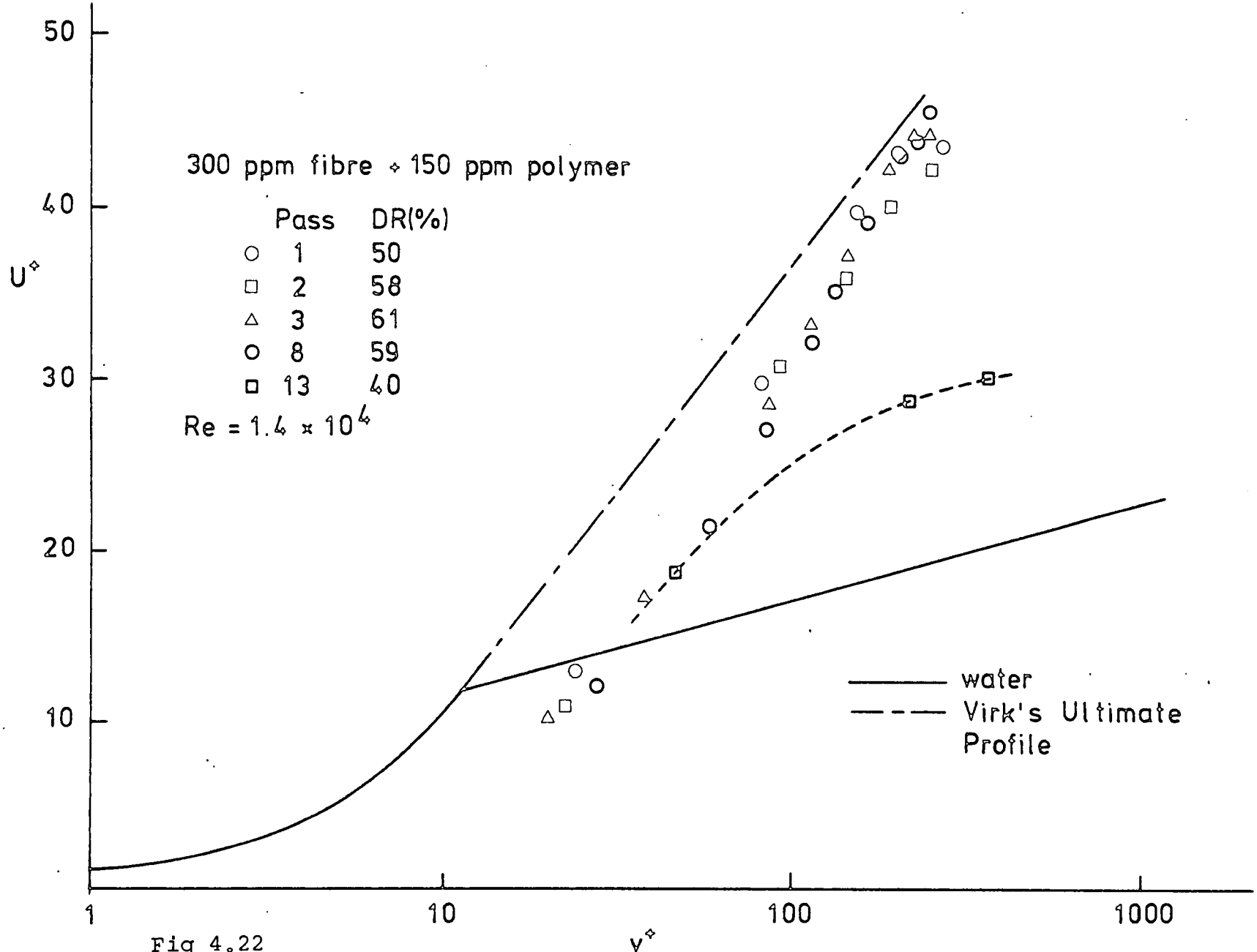
50
40
30
20
10
U+
300 ppm fibre + 150 ppm polymer
Pass DR(%)
1 50
2 58
3 61
8 59
13 40
Re = 1.4 × 10^4
water
Virk's Ultimate Profile
1
10
100
1000
y+

Fig 4.22

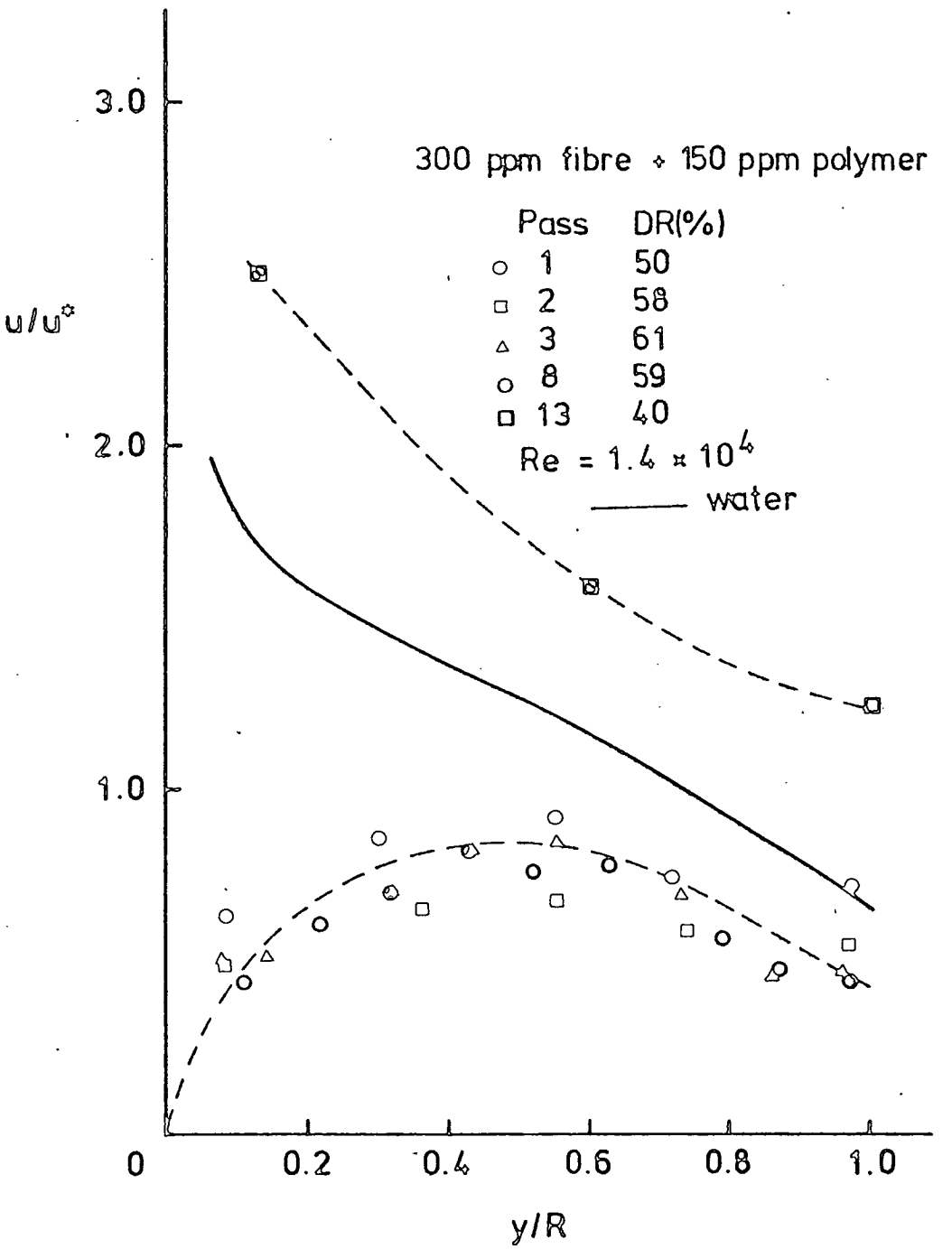
3.0
2.0
1.0
0
0.2
0.4
0.6
0.8
1.0
u/u*
y/R
300 ppm fibre + 150 ppm polymer
Pass DR(%)
1 50
2 58
3 61
8 59
13 40
Re = 1.4 × 10⁴
water

Fig 4.23

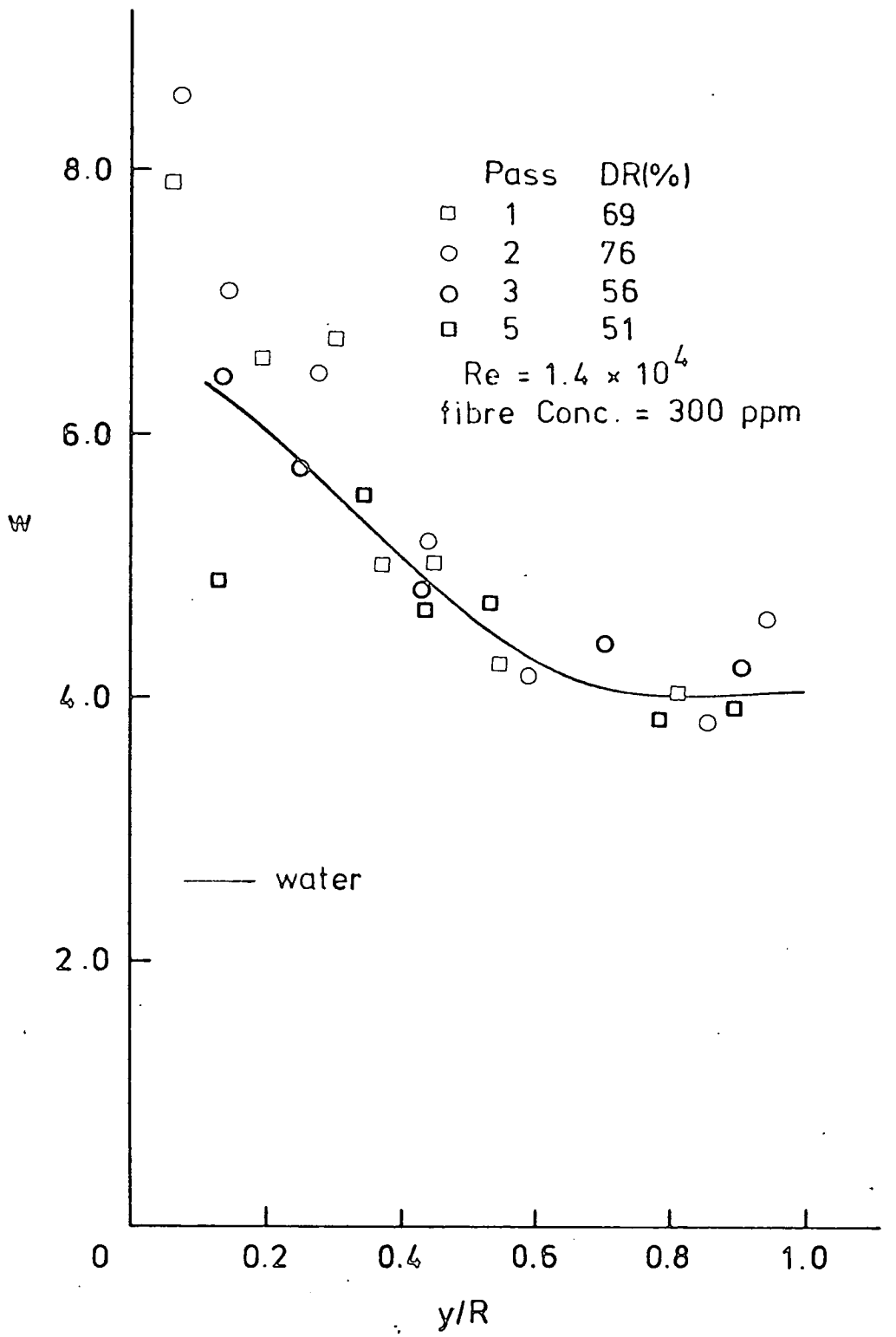
8.0
6.0
4.0
2.0
0
0.2
0.4
0.6
0.8
1.0
W
y/R
Pass DR(%)
1 69
2 76
3 56
5 51
Re = 1.4 × 10^4
fibre Conc. = 300 ppm
water

Fig 4.24

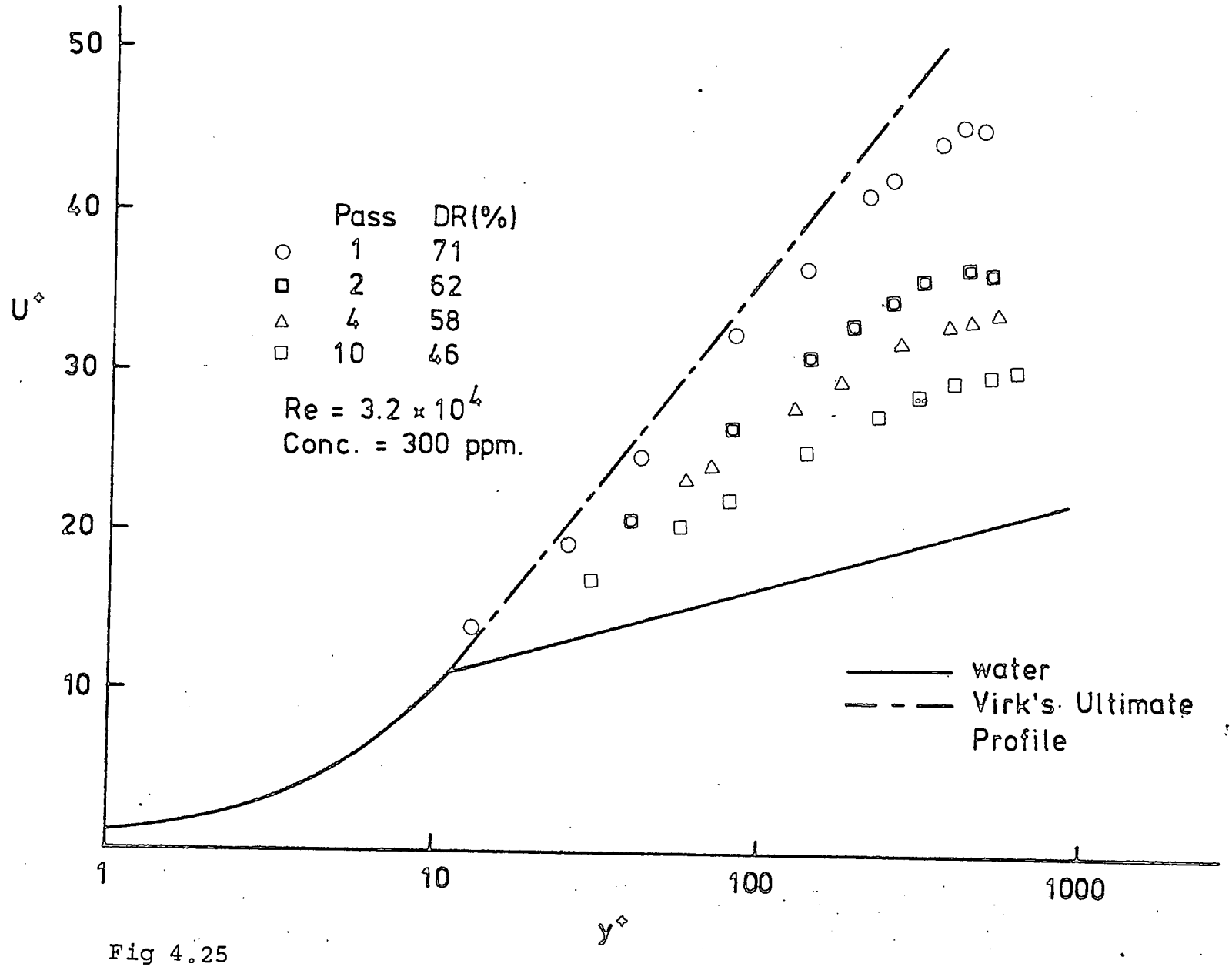
50
40
30
20
10
U+
Pass DR(%)
1 71
2 62
4 58
10 46
Re = 3.2 x 10^4
Conc. = 300 ppm.
water
Virk's Ultimate Profile
1
10
100
1000
y+

Fig 4.25

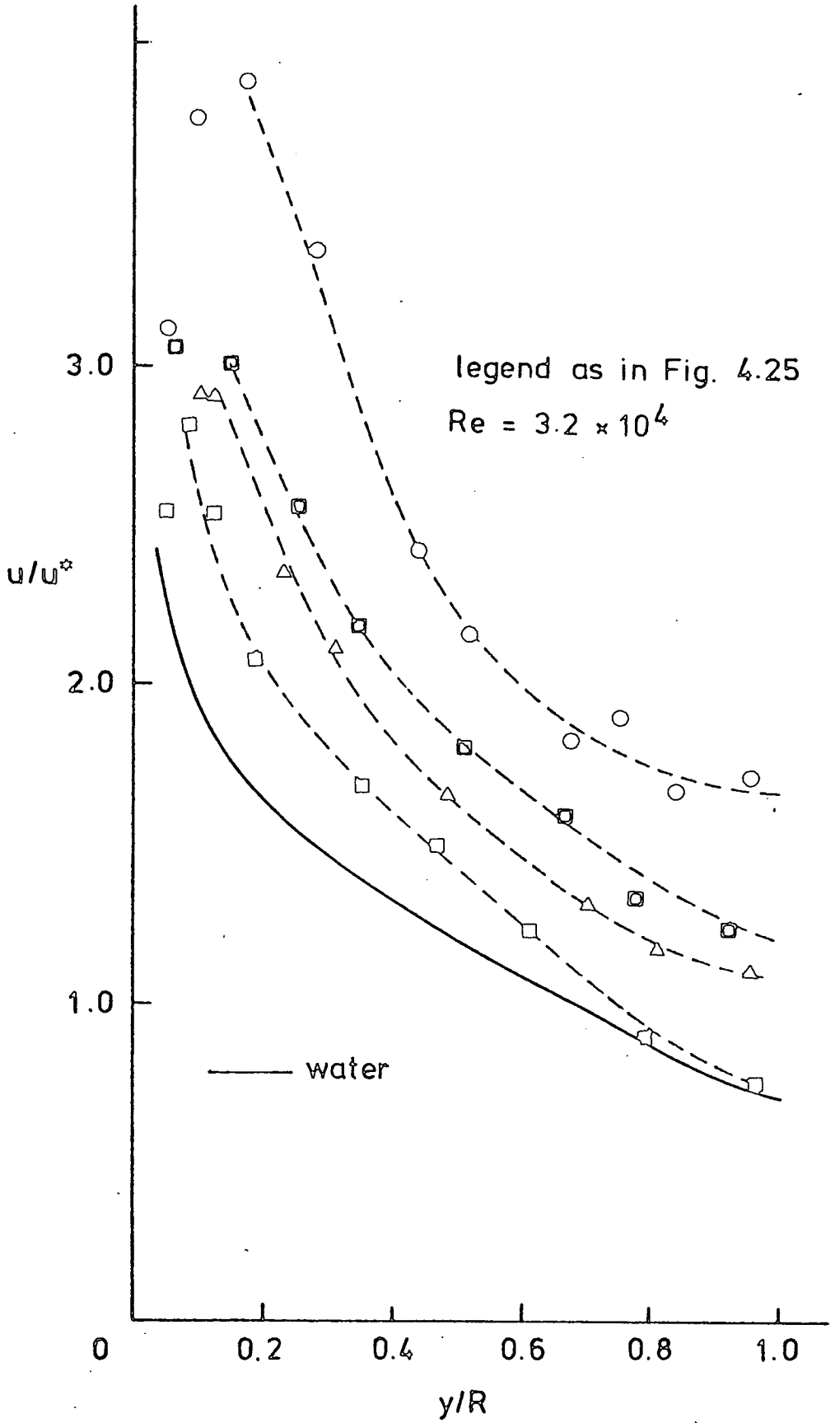

Fig 4.26

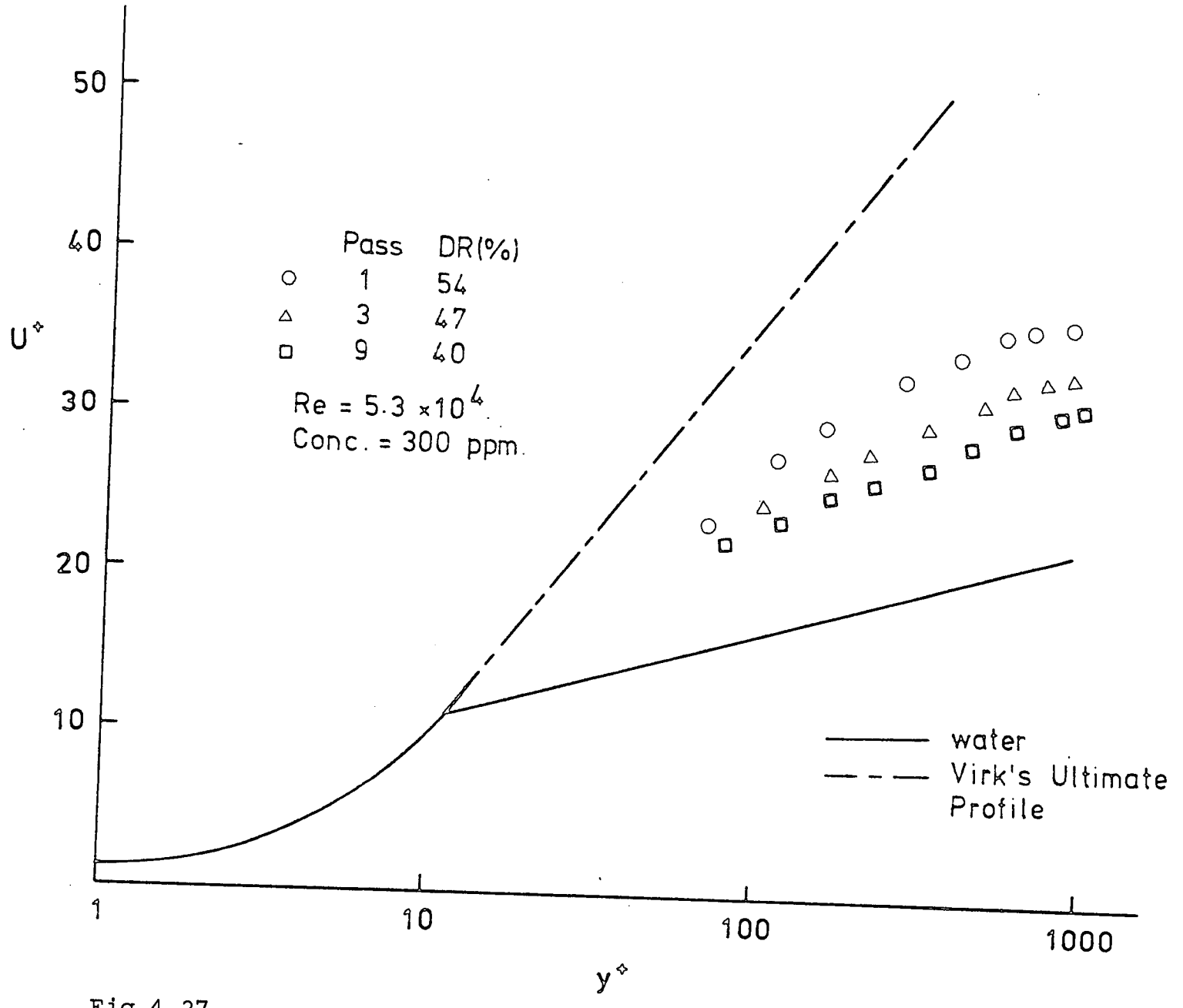
50
40
30
20
10
U+
Pass DR(%)
1 54
3 47
9 40
Re = 5.3 ×10^4
Conc. = 300 ppm.
water
Virk's Ultimate Profile
1
10
100
1000
y+

Fig 4.27

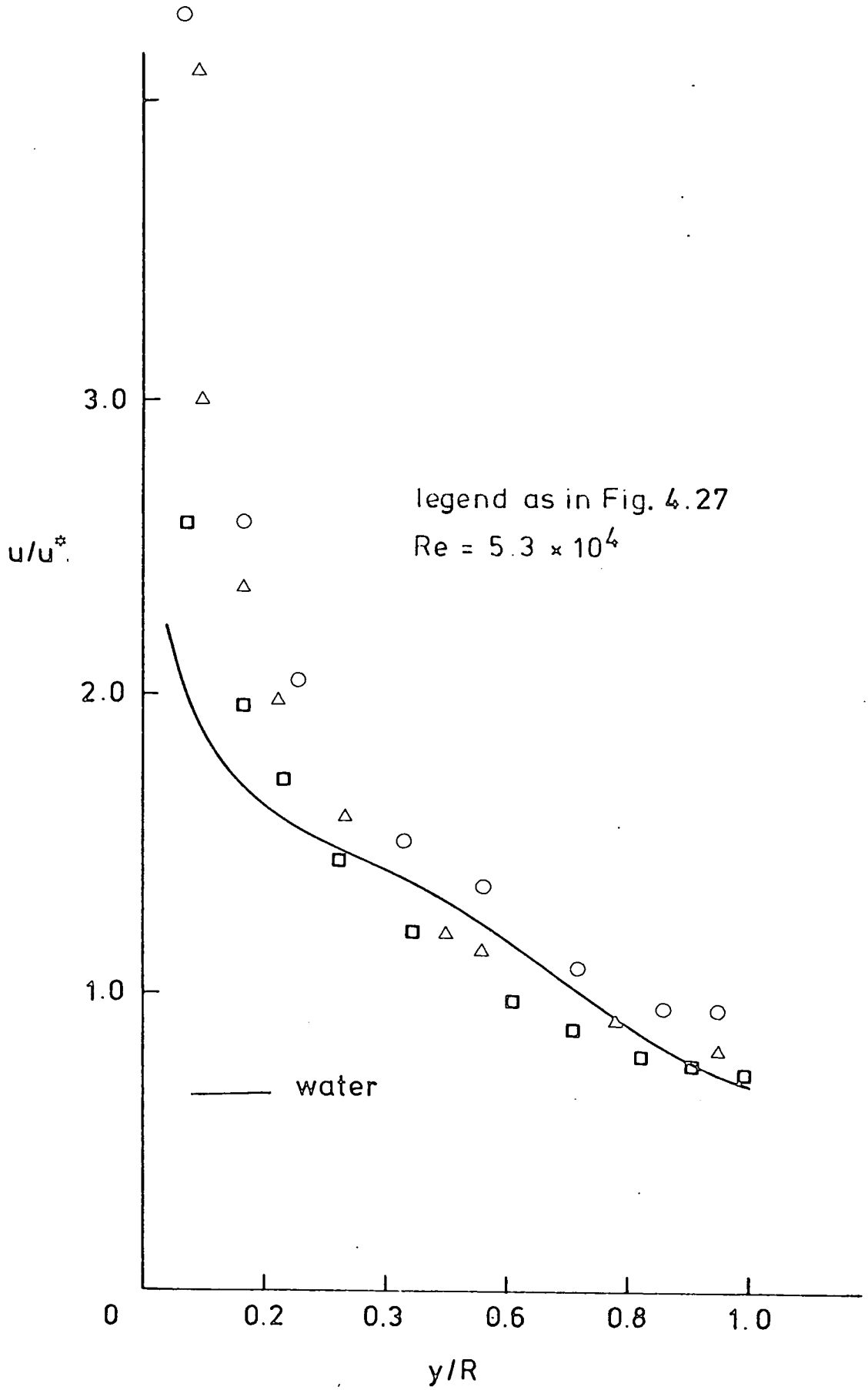
3.0
2.0
1.0
0
u/u*
legend as in Fig. 4.27
Re = 5.3 x 10^4
water
0.2
0.3
0.6
0.8
1.0
y/R

Fig 4.28

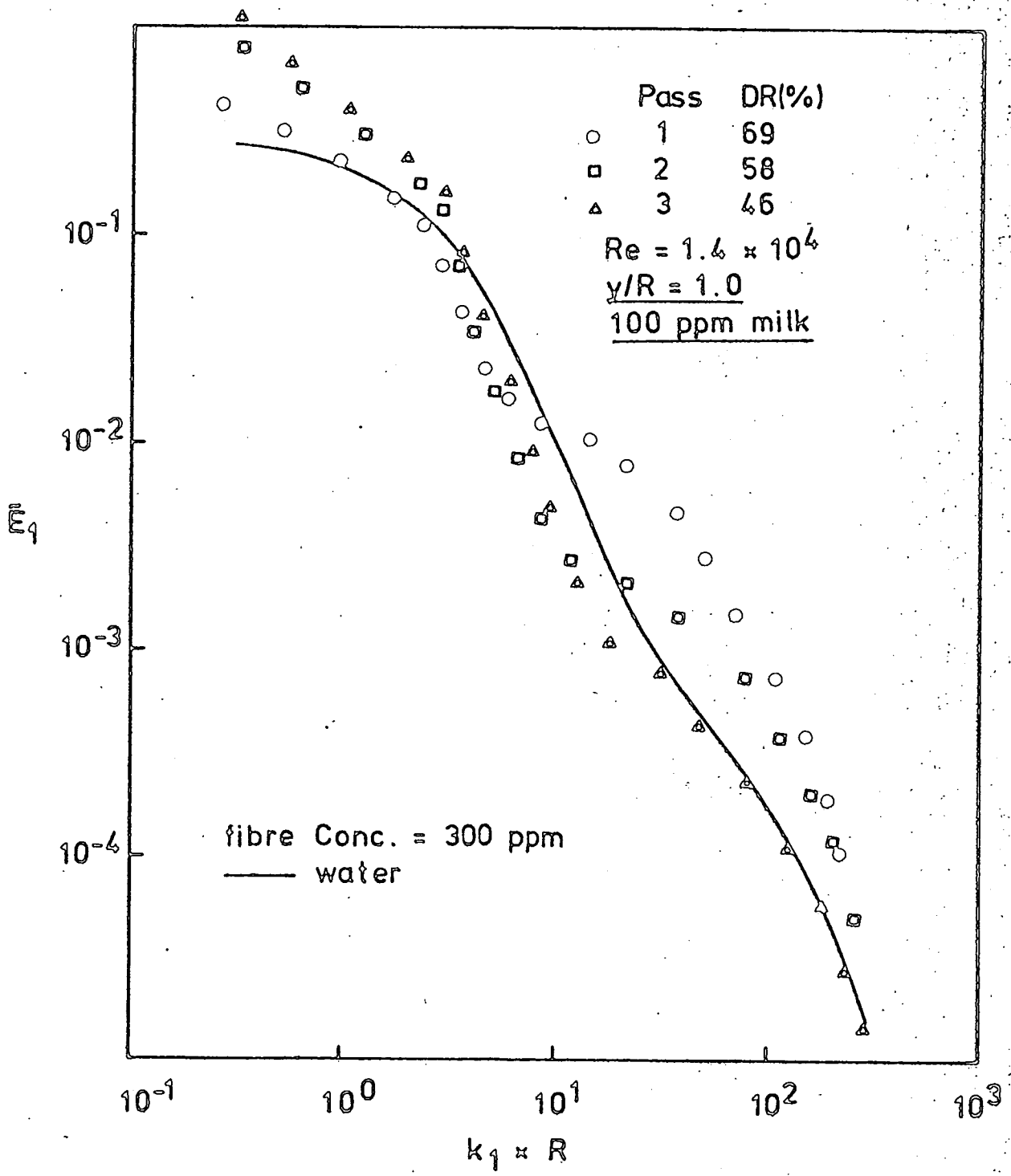
Pass DR(%)
1 69
2 58
3 46
Re = 1.4 × 10^4
y/R = 1.0
100 ppm milk
fibre Conc. = 300 ppm
water
$\bar{E}_1$
$k_1 \times R$
10^{-1}
10^{-2}
10^{-3}
10^{-4}
10^{-1}
10^{0}
10^{1}
10^{2}
10^{3}

Fig 4.29

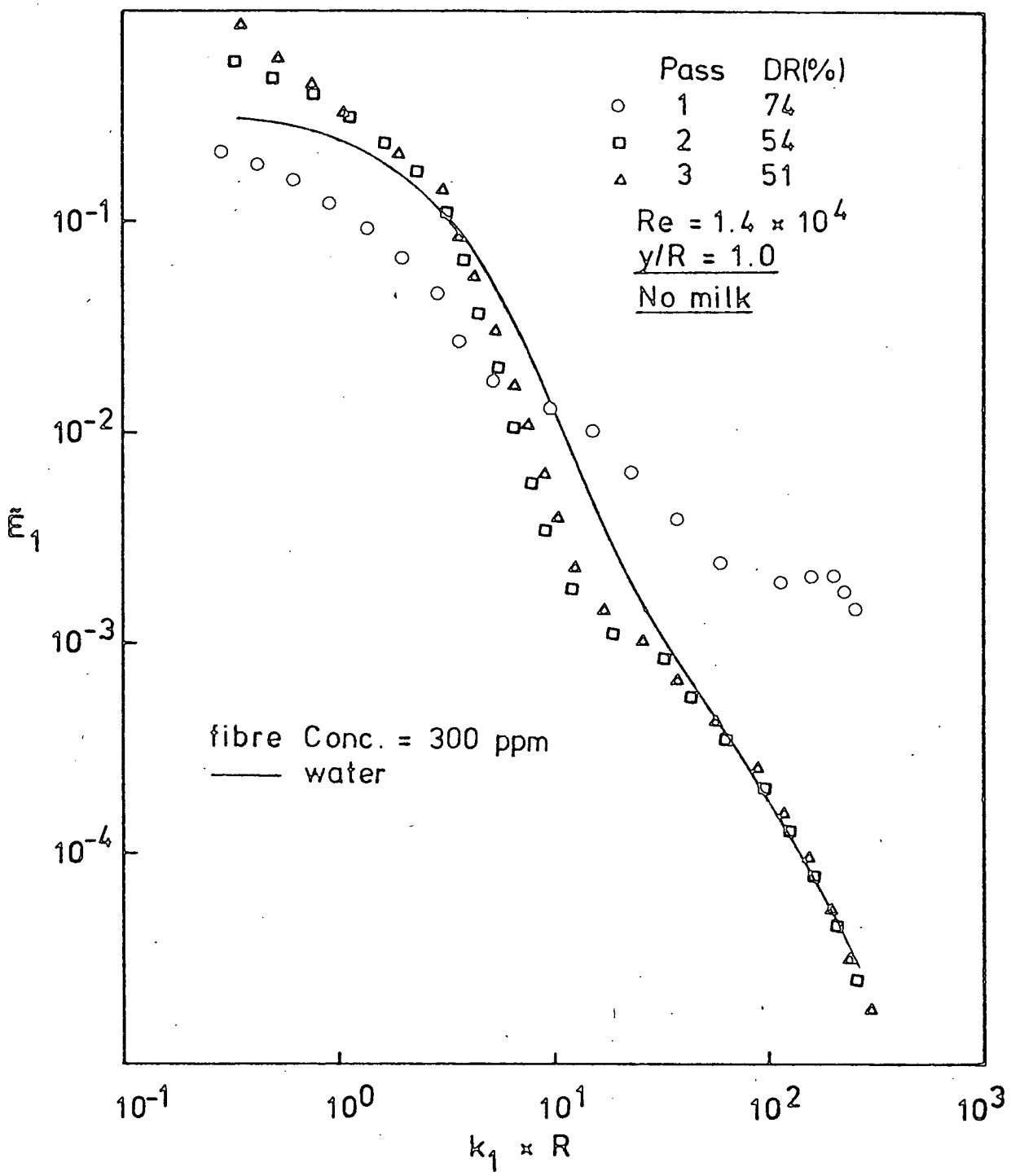
Pass DR(%)
1 74
2 54
3 51
Re = 1.4 × 10^4
y/R = 1.0
No milk
fibre Conc. = 300 ppm
water
$\tilde{E}_1$
10^{-1}
10^{-2}
10^{-3}
10^{-4}
10^{-1}
10^{0}
10^{1}
10^{2}
10^{3}
$k_1 \times R$

Fig 4.30

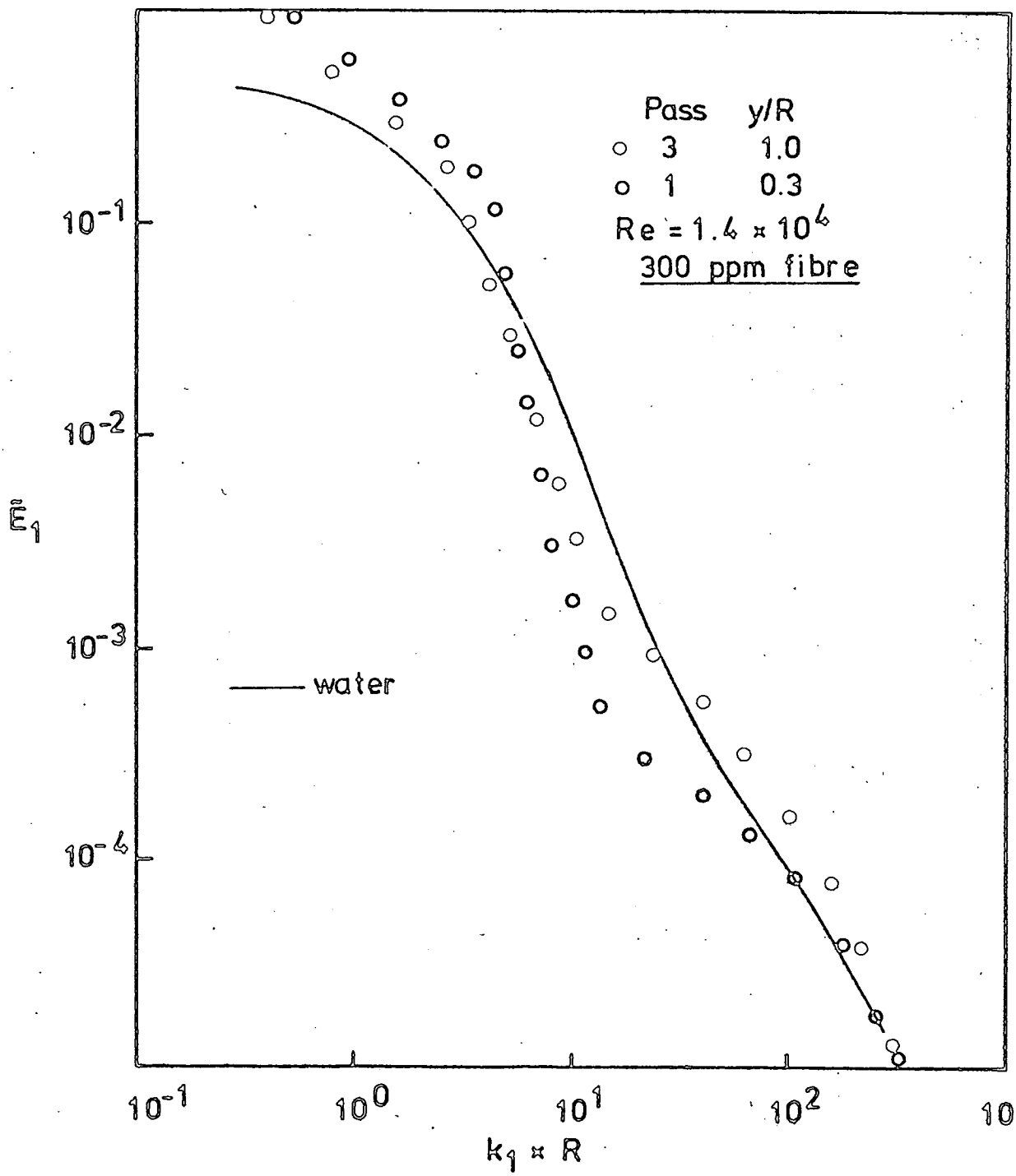
Pass y/R
3 1.0
1 0.3
Re = 1.4 × 10⁴
300 ppm fibre
water
10^{-1}
10^{-2}
10^{-3}
10^{-4}
$\tilde{E}_1$
10^{-1}
10^{0}
10^{1}
10^{2}
10^{3}
$k_1 \times R$

Fig 4.31

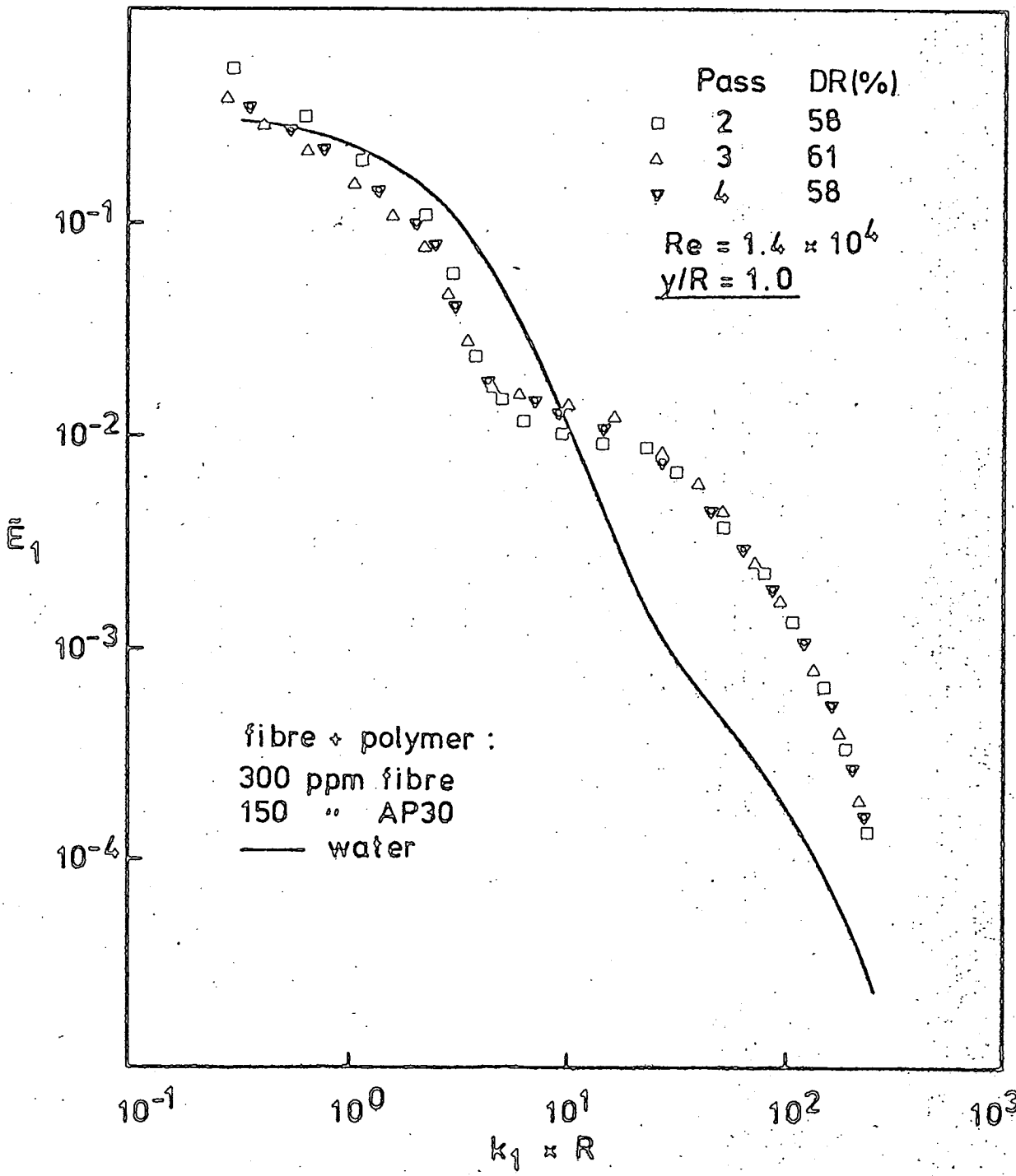
Pass DR(%)
2 58
3 61
4 58
Re = 1.4 × 10⁴
y/R = 1.0
fibre + polymer :
300 ppm fibre
150 " AP30
water
$\tilde{E}_1$
10^{-1}
10^{-2}
10^{-3}
10^{-4}
10^{-1}
10^{0}
10^{1}
10^{2}
10^{3}
$k_1 \times R$

Fig 4.32

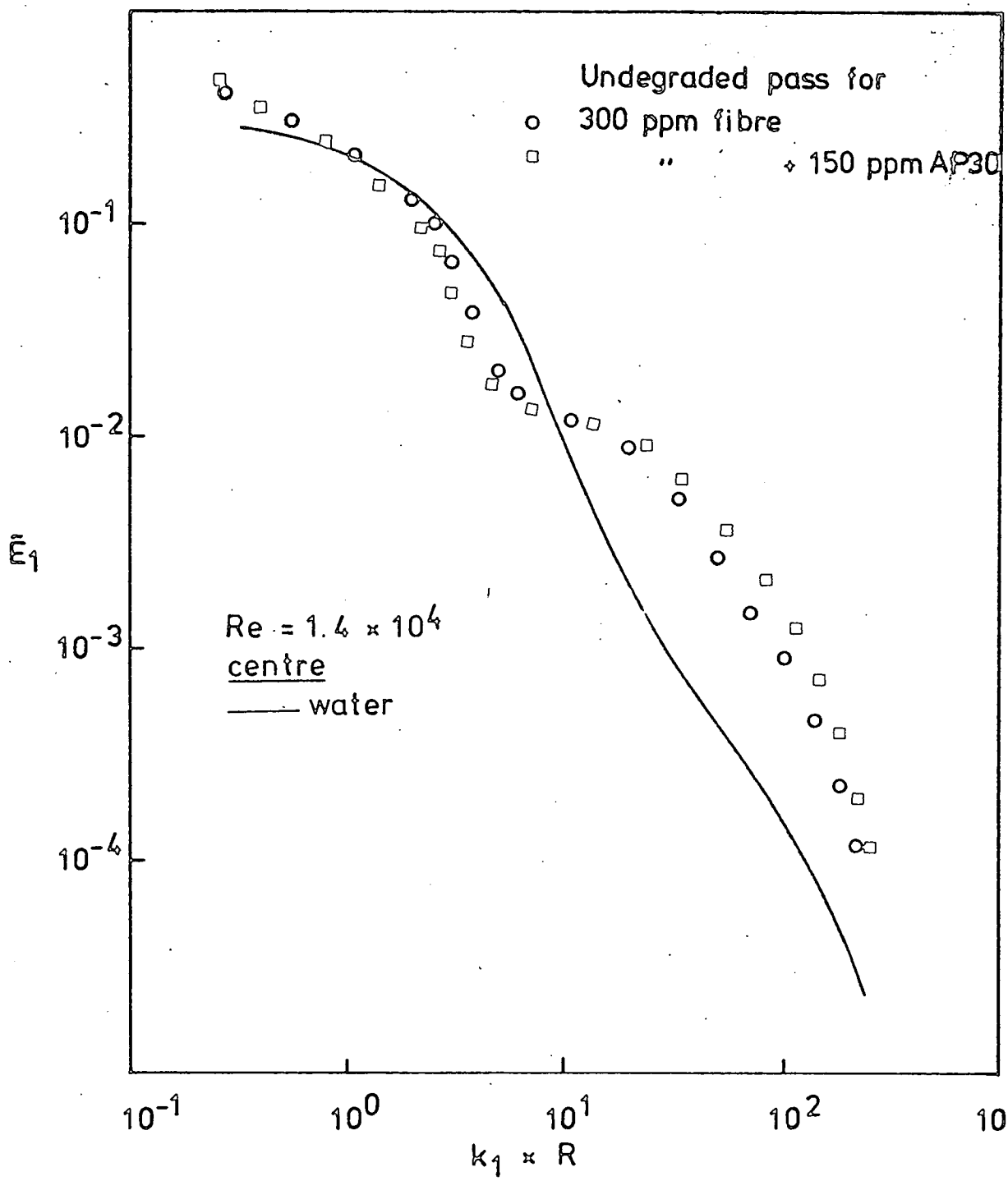
Undegraded pass for
300 ppm fibre
" ◇ 150 ppm AP30
10^{-1}
10^{-2}
10^{-3}
10^{-4}
$\tilde{E}_1$
Re = 1.4 × 10^4
centre
water
10^{-1}
10^{0}
10^{1}
10^{2}
10^{3}
$k_1 \times R$

Fig 4.33

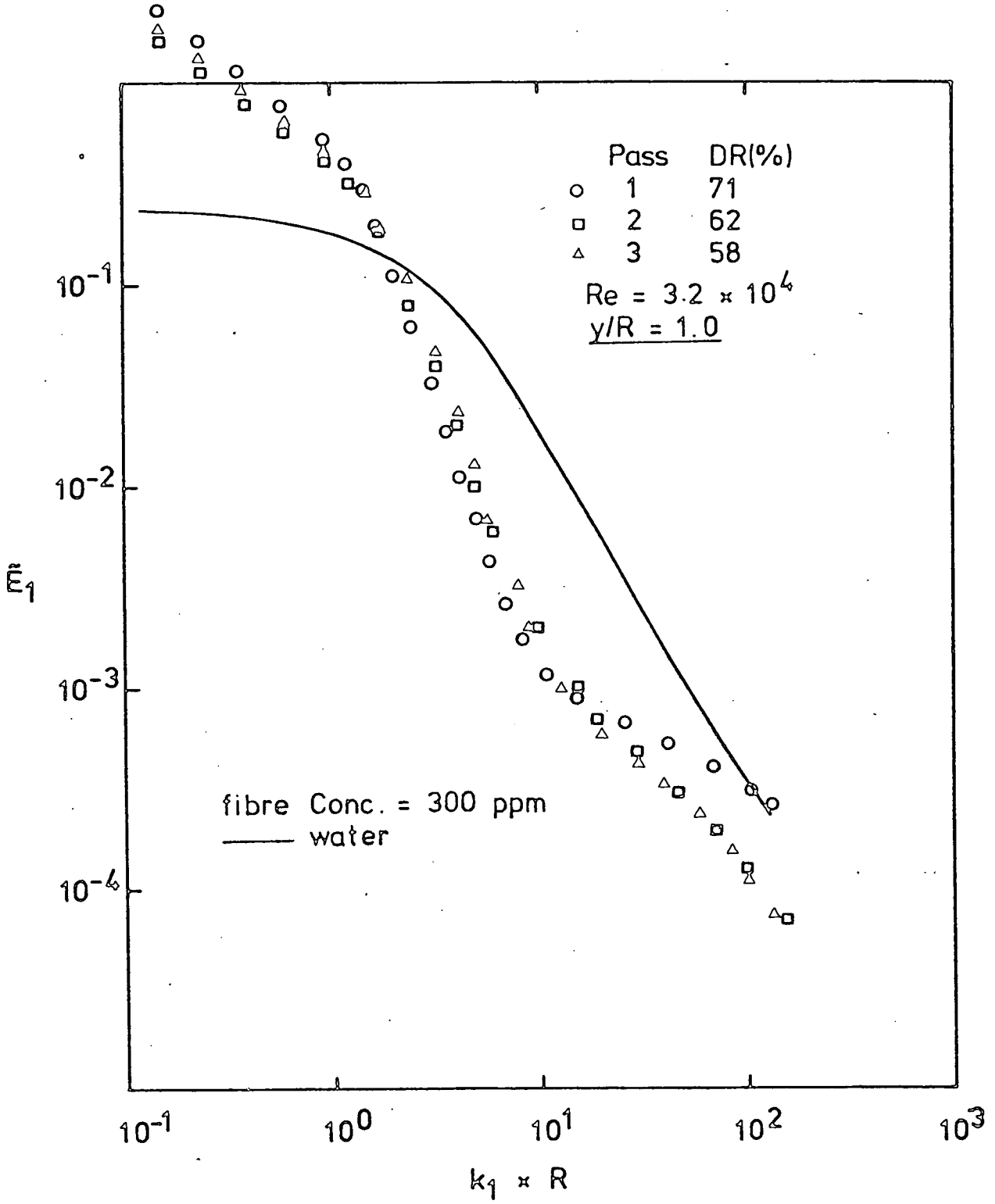
Pass DR(%)
1 71
2 62
3 58
Re = 3.2 × 10^4
y/R = 1.0
fibre Conc. = 300 ppm
water
$\tilde{E}_1$
10^{-1}
10^{-2}
10^{-3}
10^{-4}
10^{-1}
10^{0}
10^{1}
10^{2}
10^{3}
$k_1 \times R$

Fig 4.34

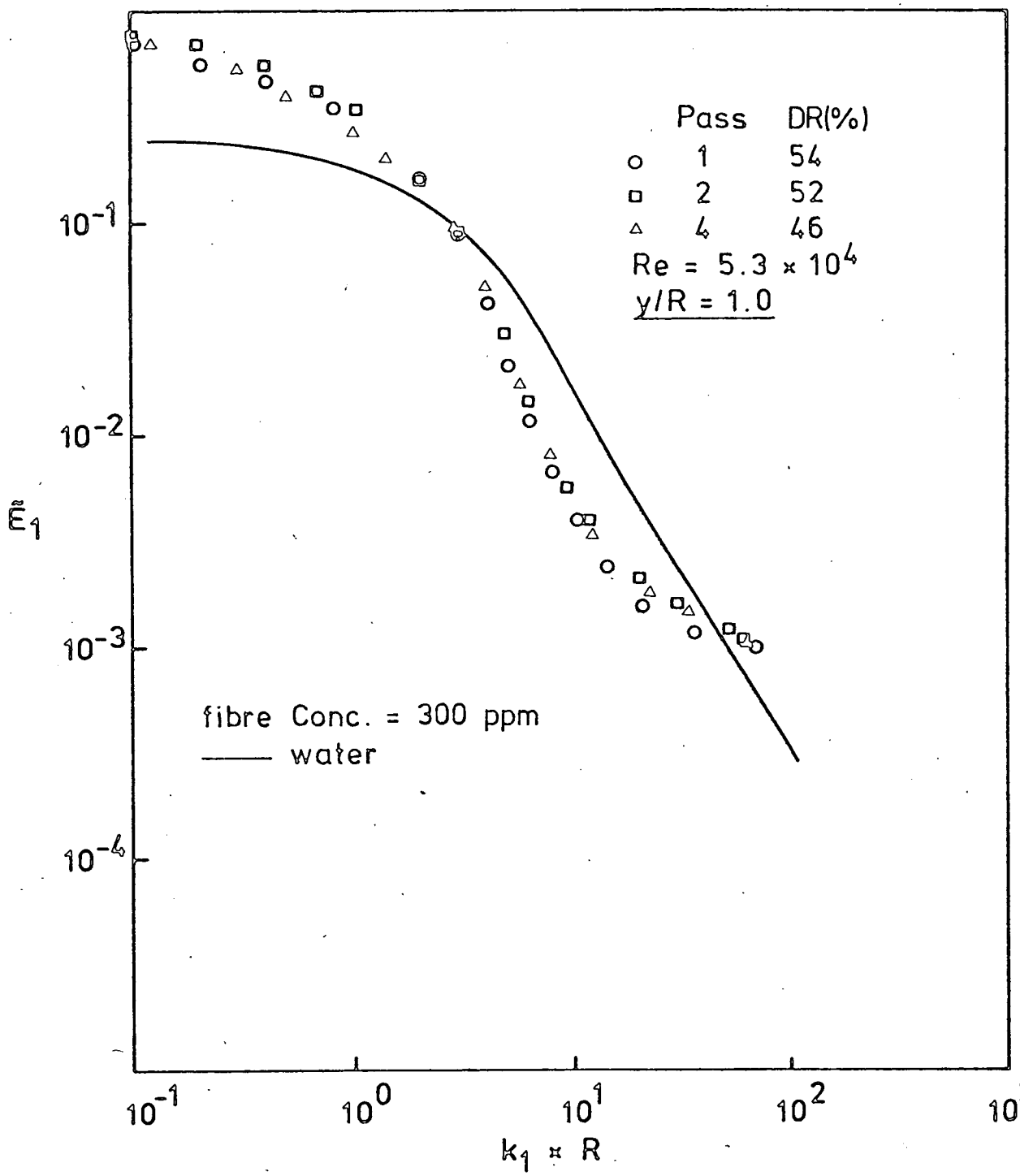
Pass DR(%)
1 54
2 52
4 46
Re = 5.3 × 10^4
y/R = 1.0
fibre Conc. = 300 ppm
water
$\tilde{E}_1$
$k_1 \times R$
10^{-1}
10^{-2}
10^{-3}
10^{-4}
10^{-1}
10^{0}
10^{1}
10^{2}
10^{3}

Fig 4.35

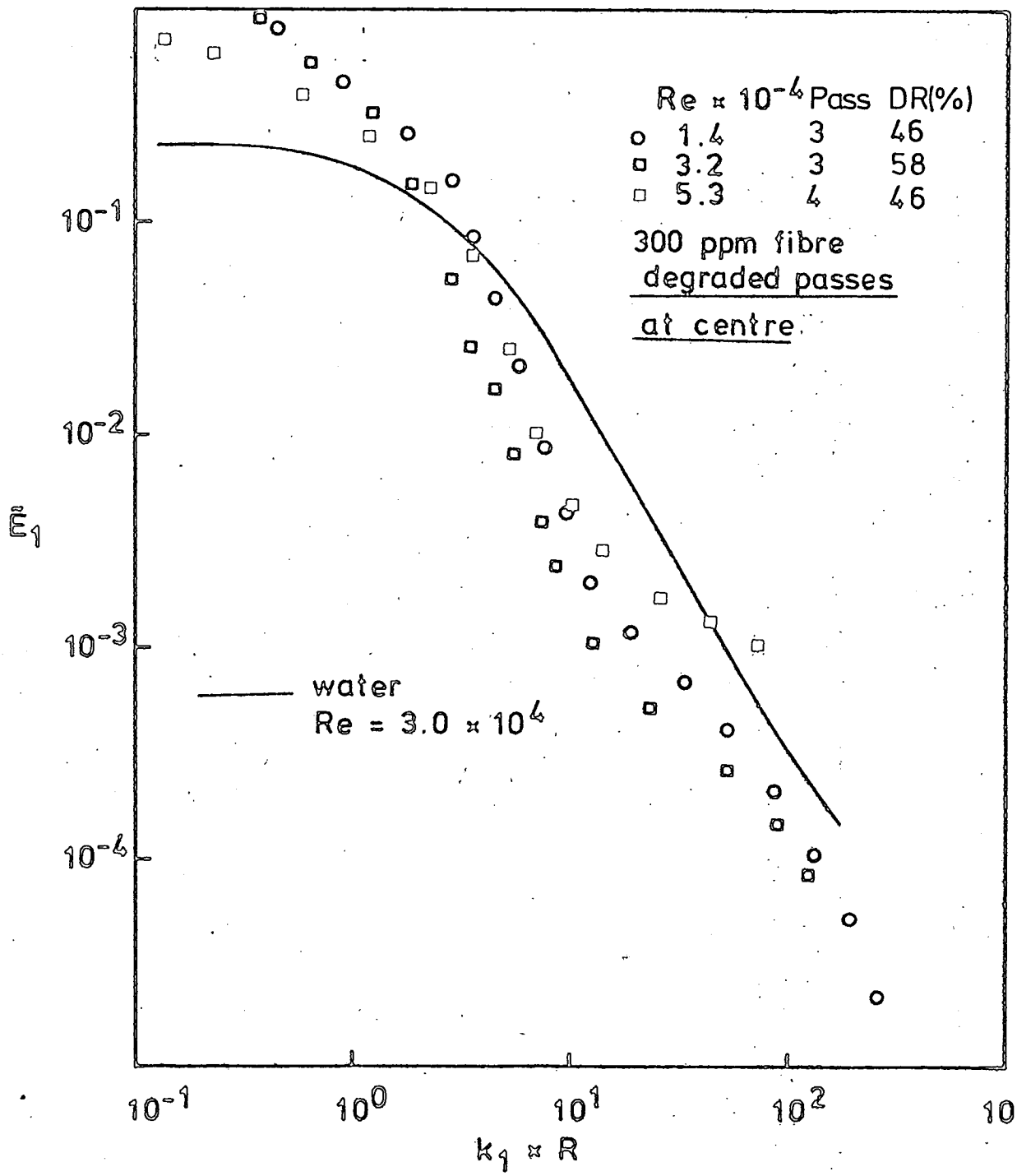
Re × 10⁻⁴ Pass DR(%)
o 1.4 3 46
□ 3.2 3 58
□ 5.3 4 46
300 ppm fibre
degraded passes
at centre
water
Re = 3.0 × 10⁴
10⁻¹
10⁻²
10⁻³
10⁻⁴
Ẽ₁
10⁻¹
10⁰
10¹
10²
10³
k₁ × R

Fig 4.36

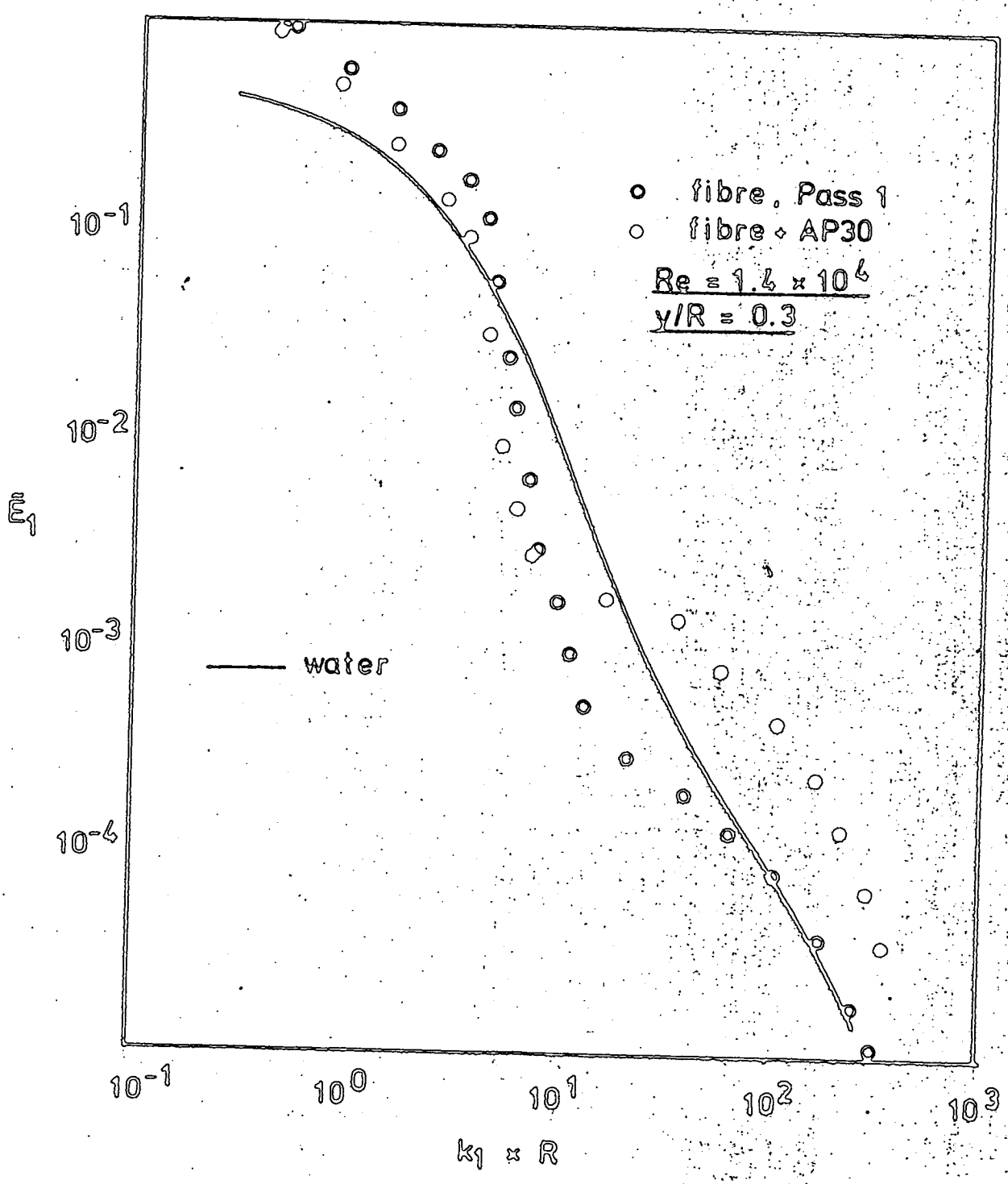
fibre, Pass 1
fibre + AP30
Re = 1.4 × 10⁴
y/R = 0.3
water
10⁻¹
10⁻²
10⁻³
10⁻⁴
E₁
10⁻¹
10⁰
10¹
10²
10³
k₁ × R

Fig 4.37

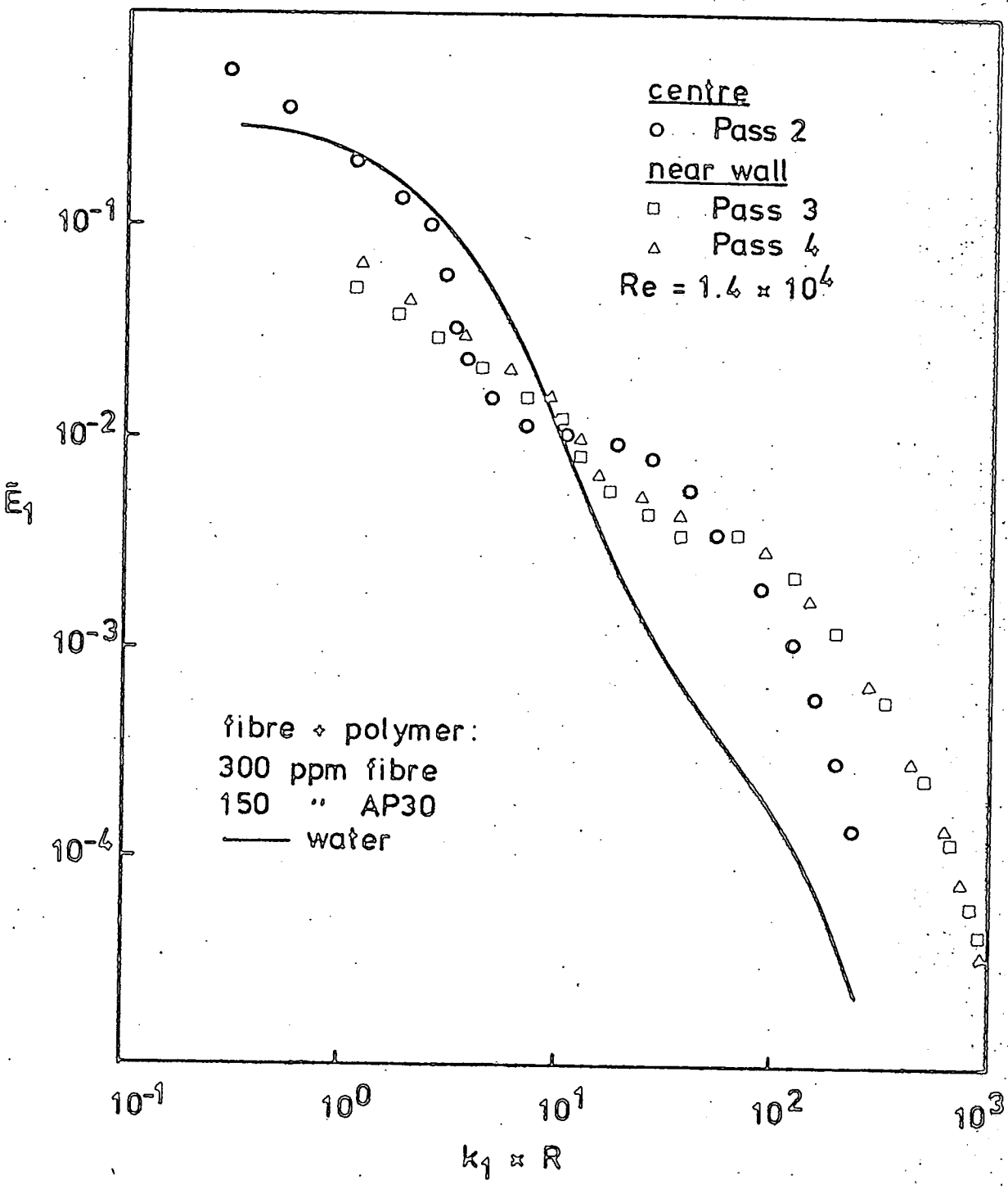
centre
Pass 2
near wall
Pass 3
Pass 4
Re = 1.4 × 10⁴
fibre + polymer:
300 ppm fibre
150 " AP30
water
$\tilde{E}_1$
10^{-1}
10^{-2}
10^{-3}
10^{-4}
10^{-1}
10^{0}
10^{1}
10^{2}
10^{3}
$k_1 \times R$

Fig 4.38

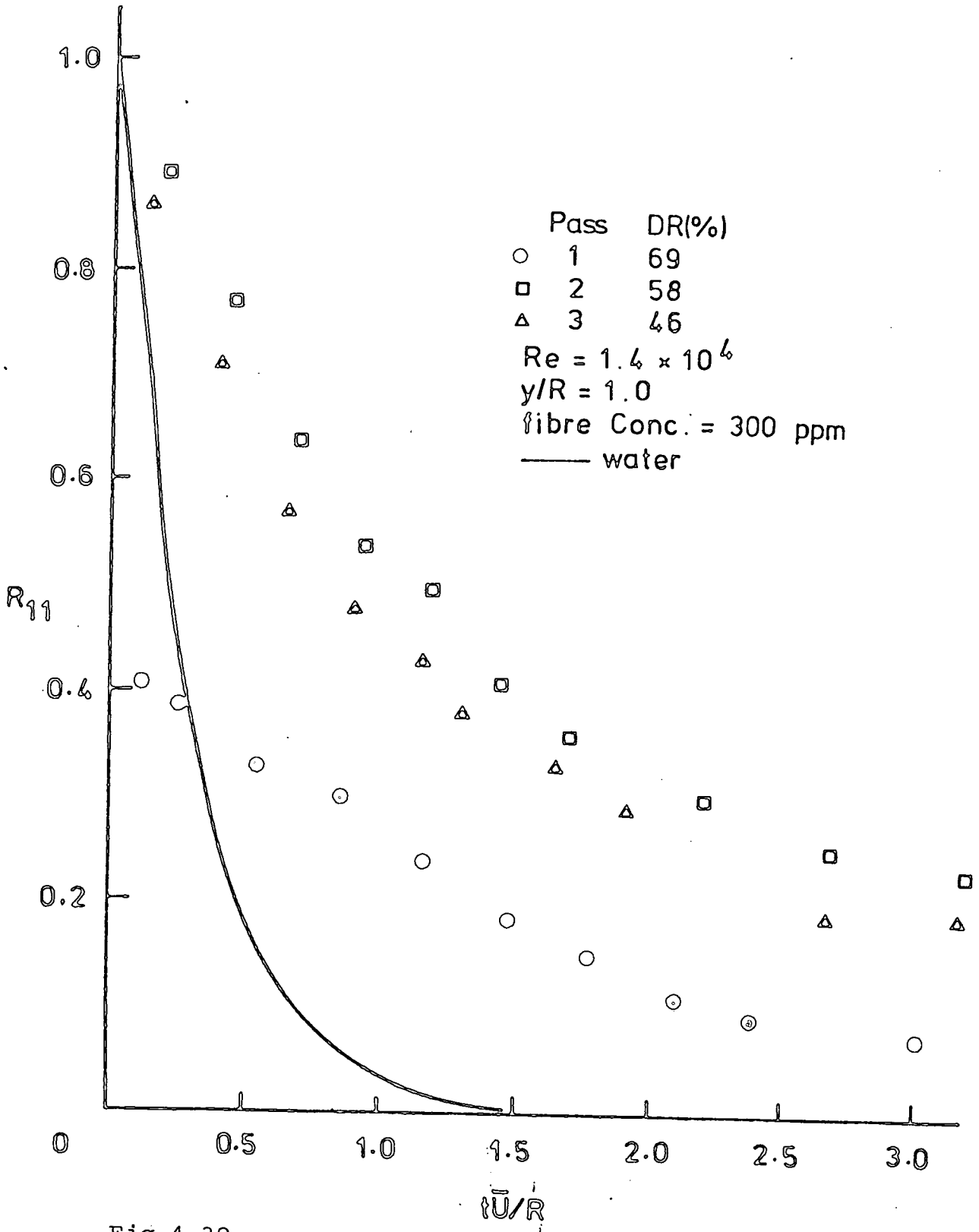
1.0
0.8
0.6
0.4
0.2
0
R_{11}
0.5
1.0
1.5
2.0
2.5
3.0
$\ell\bar{U}/R$
Pass DR(%)
1 69
2 58
3 46
Re = 1.4 × 10⁴
y/R = 1.0
fibre Conc. = 300 ppm
water

Fig 4.39

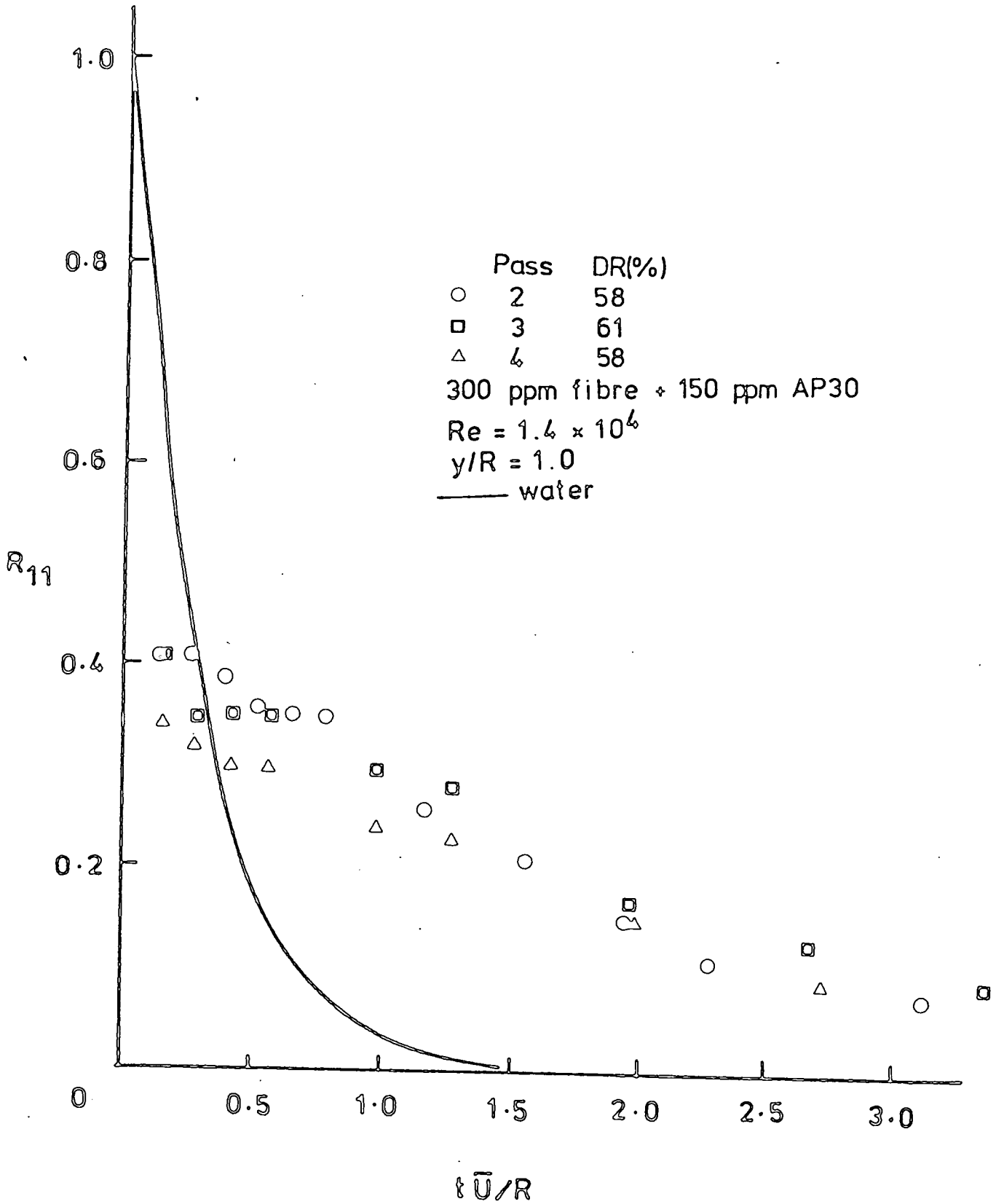
1·0
0·8
0·6
0·4
0·2
0
R_{11}
0·5
1·0
1·5
2·0
2·5
3·0
$t\bar{U}/R$
Pass DR(%)
2 58
3 61
4 58
300 ppm fibre + 150 ppm AP30
$Re = 1.4 \times 10^4$
y/R = 1.0
water

Fig 4.40

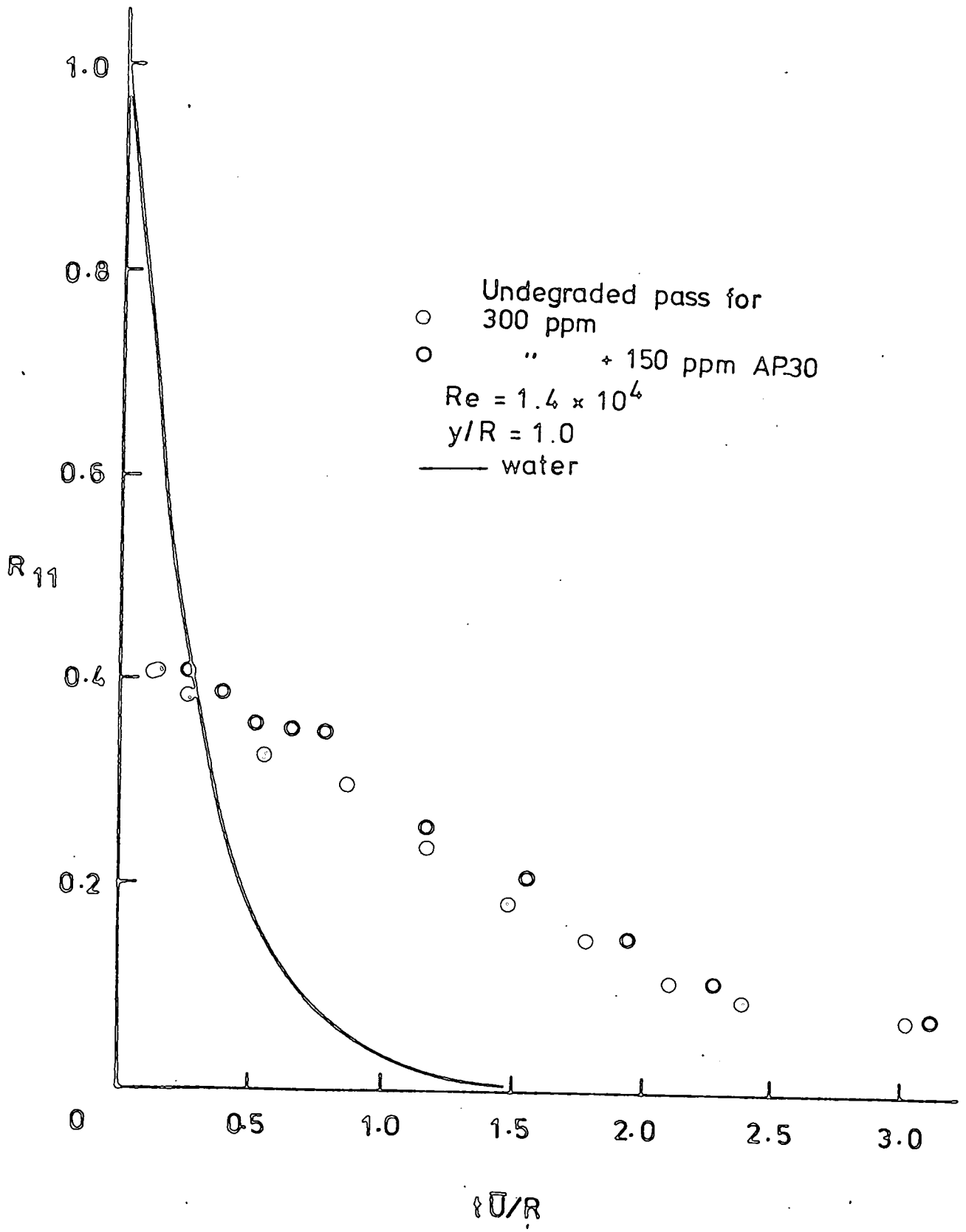
1.0
0.8
0.6
0.4
0.2
0
R_{11}
Undegraded pass for
300 ppm
" + 150 ppm AP30
$Re = 1.4 \times 10^4$
y/R = 1.0
water
0.5
1.0
1.5
2.0
2.5
3.0
$\ell \bar{U}/R$

Fig 4.41

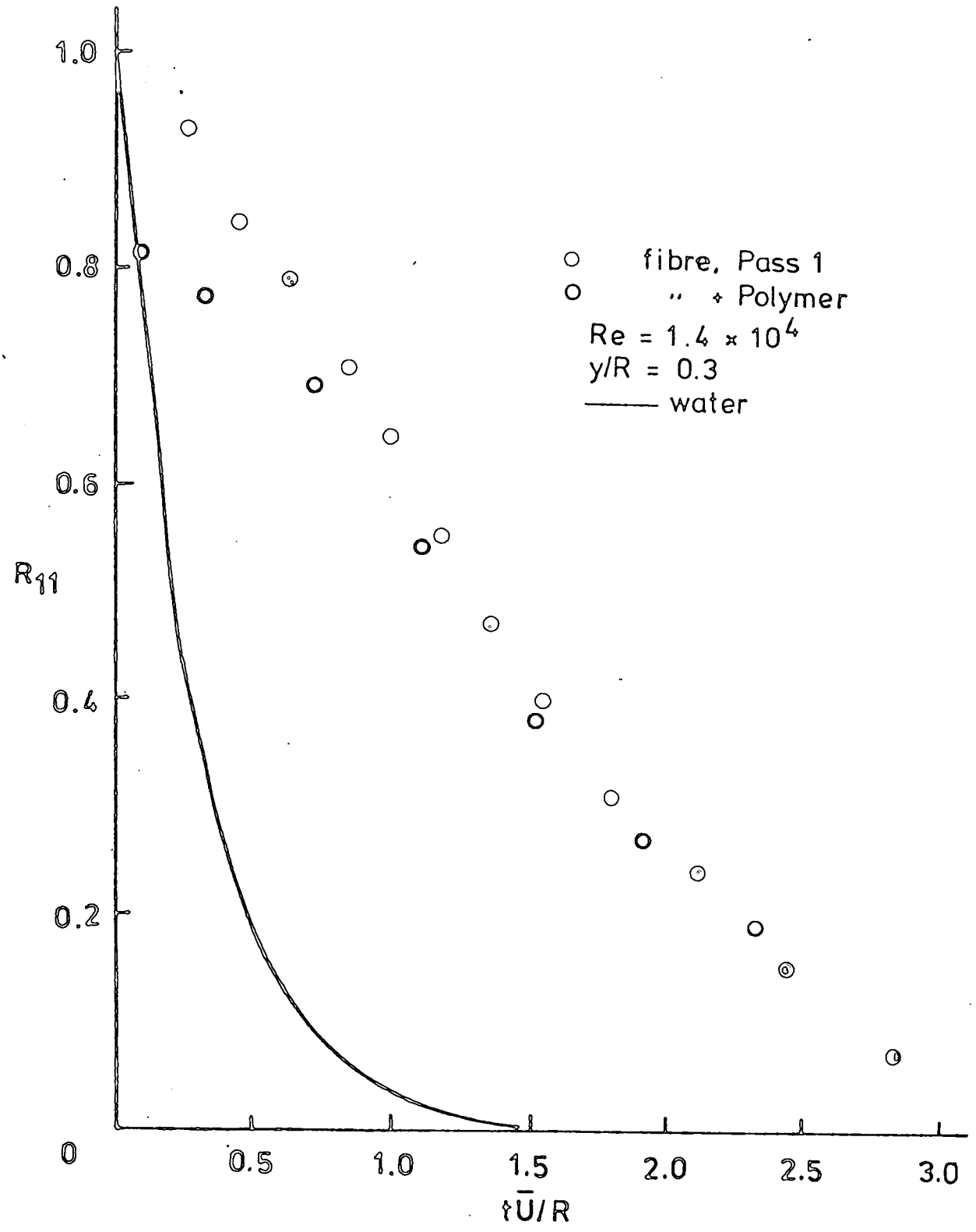
1.0
0.8
0.6
0.4
0.2
0
R_{11}
0.5
1.0
1.5
2.0
2.5
3.0
$t\bar{U}/R$
fibre, Pass 1
" + Polymer
Re = 1.4 × 10^4
y/R = 0.3
water

Fig 4.42

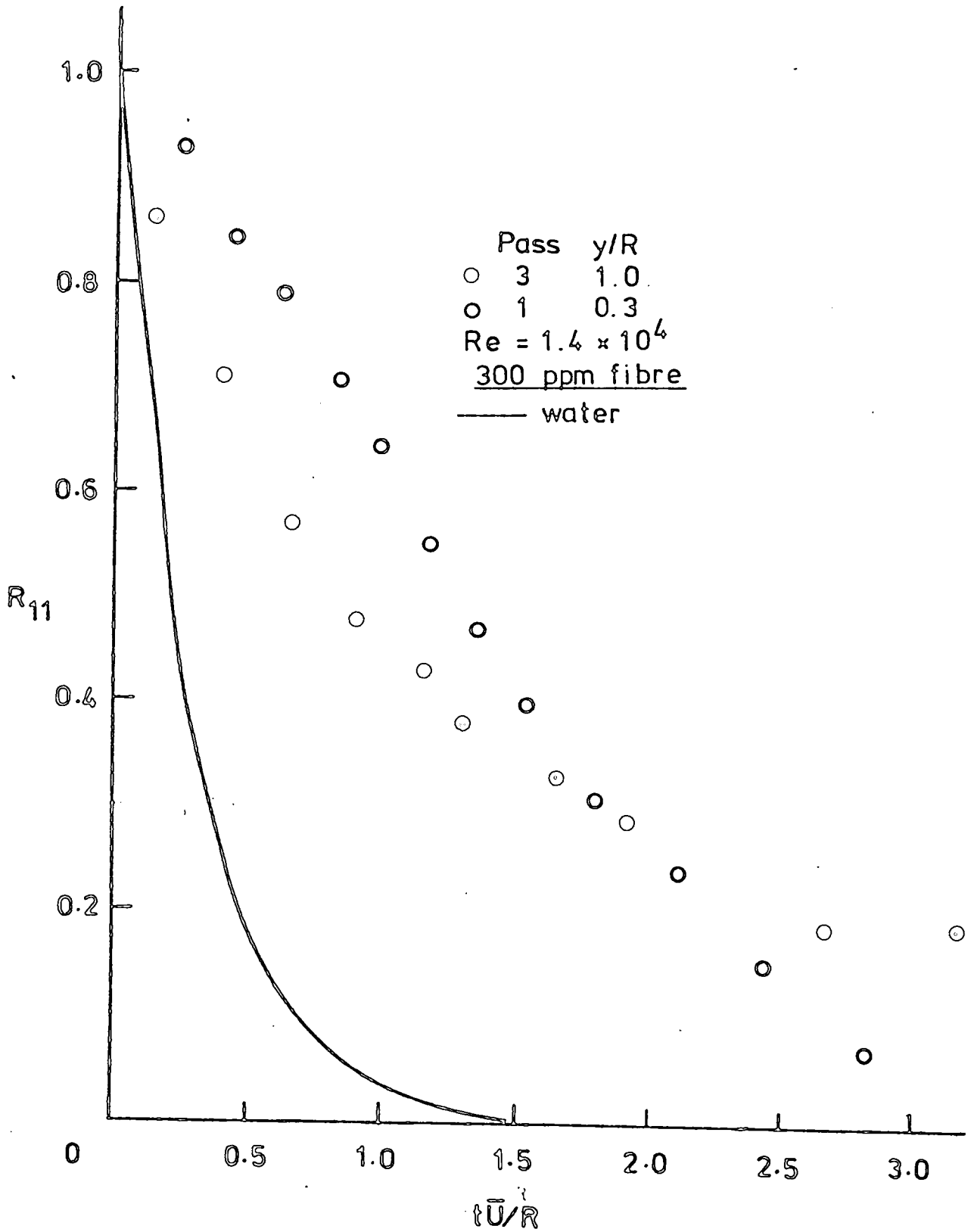
1.0
0.8
0.6
0.4
0.2
0
R_{11}
0.5
1.0
1.5
2.0
2.5
3.0
$t\bar{U}/R$
Pass y/R
3 1.0
1 0.3
Re = 1.4 × 10^4
300 ppm fibre
water

Fig 4.43

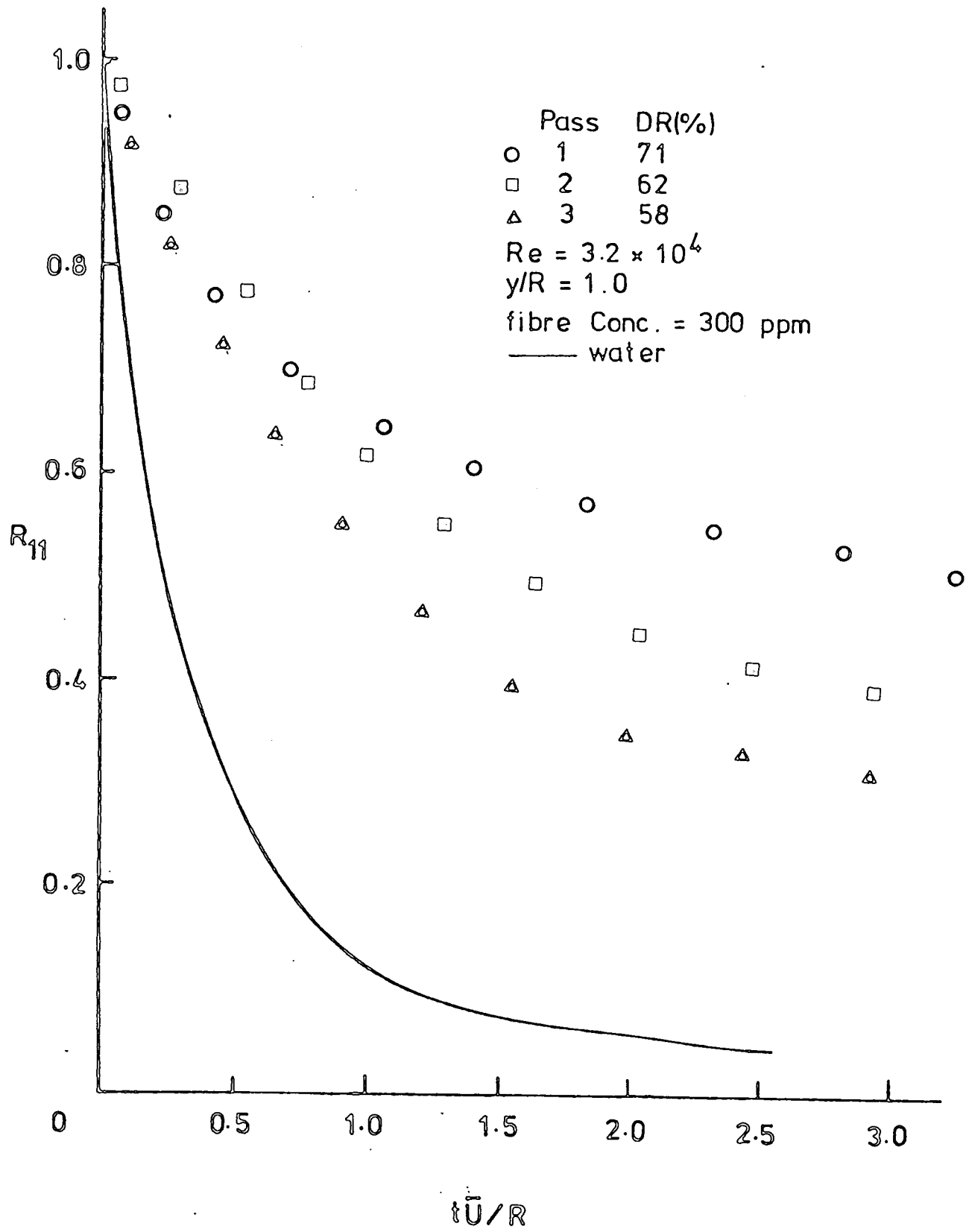
Pass DR(%)
1 71
2 62
3 58
Re = 3.2 × 10^4
y/R = 1.0
fibre Conc. = 300 ppm
water
R11
1.0
0.8
0.6
0.4
0.2
0
0.5
1.0
1.5
2.0
2.5
3.0
tŪ/R

Fig 4.44

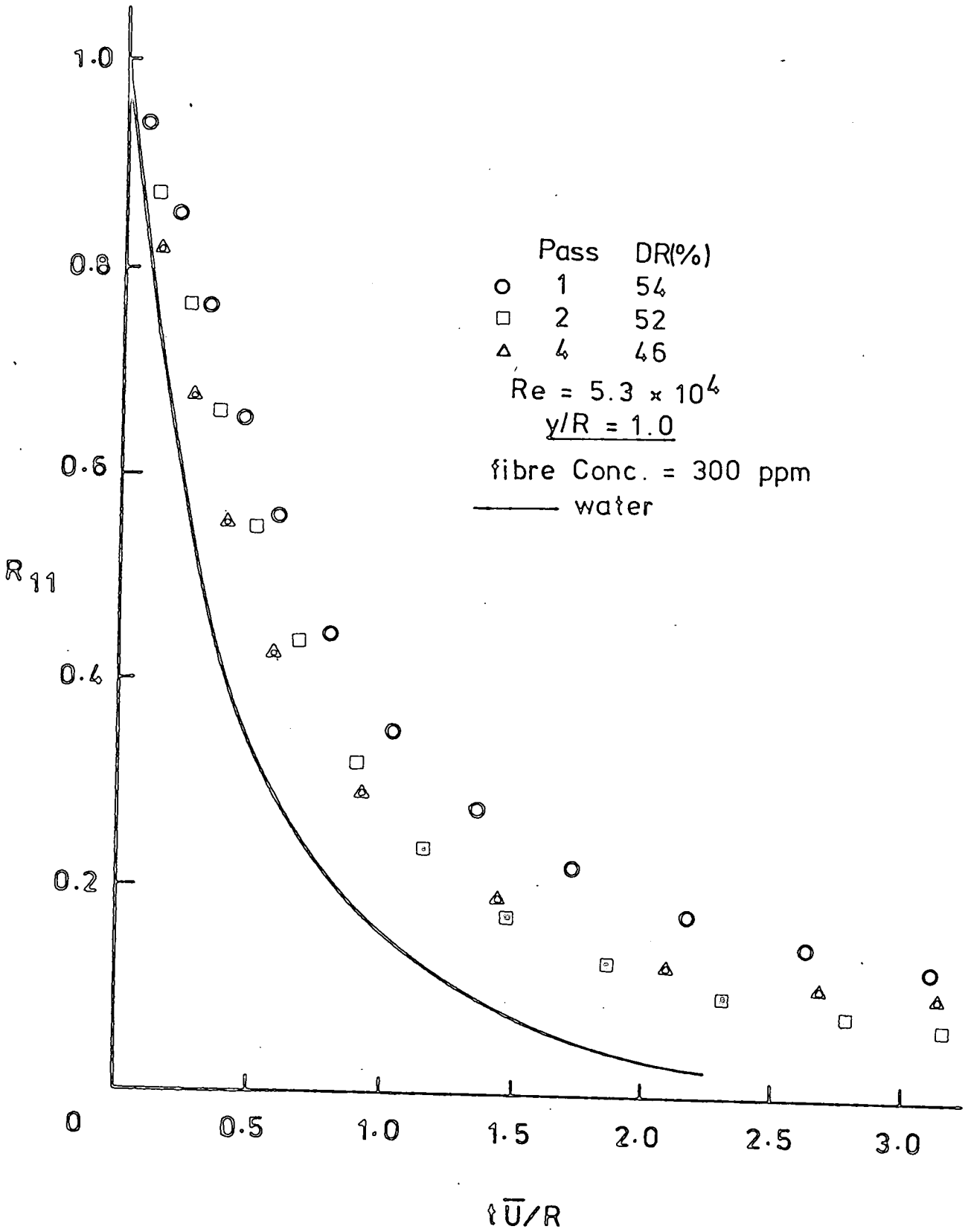
1.0
0.8
0.6
0.4
0.2
0
R_{11}
0.5
1.0
1.5
2.0
2.5
3.0
$\ell \bar{U}/R$
Pass DR(%)
1 54
2 52
4 46
Re = 5.3 x 10^4
y/R = 1.0
fibre Conc. = 300 ppm
water

Fig 4.45

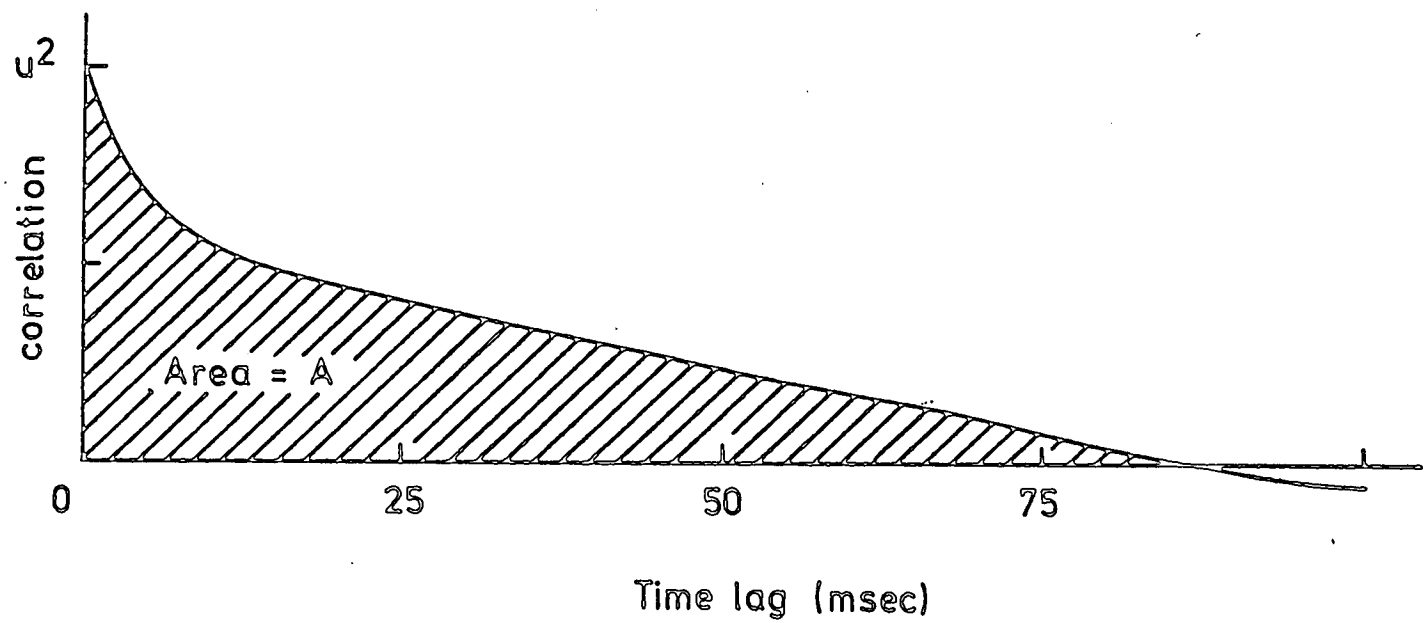

Fig 4.46

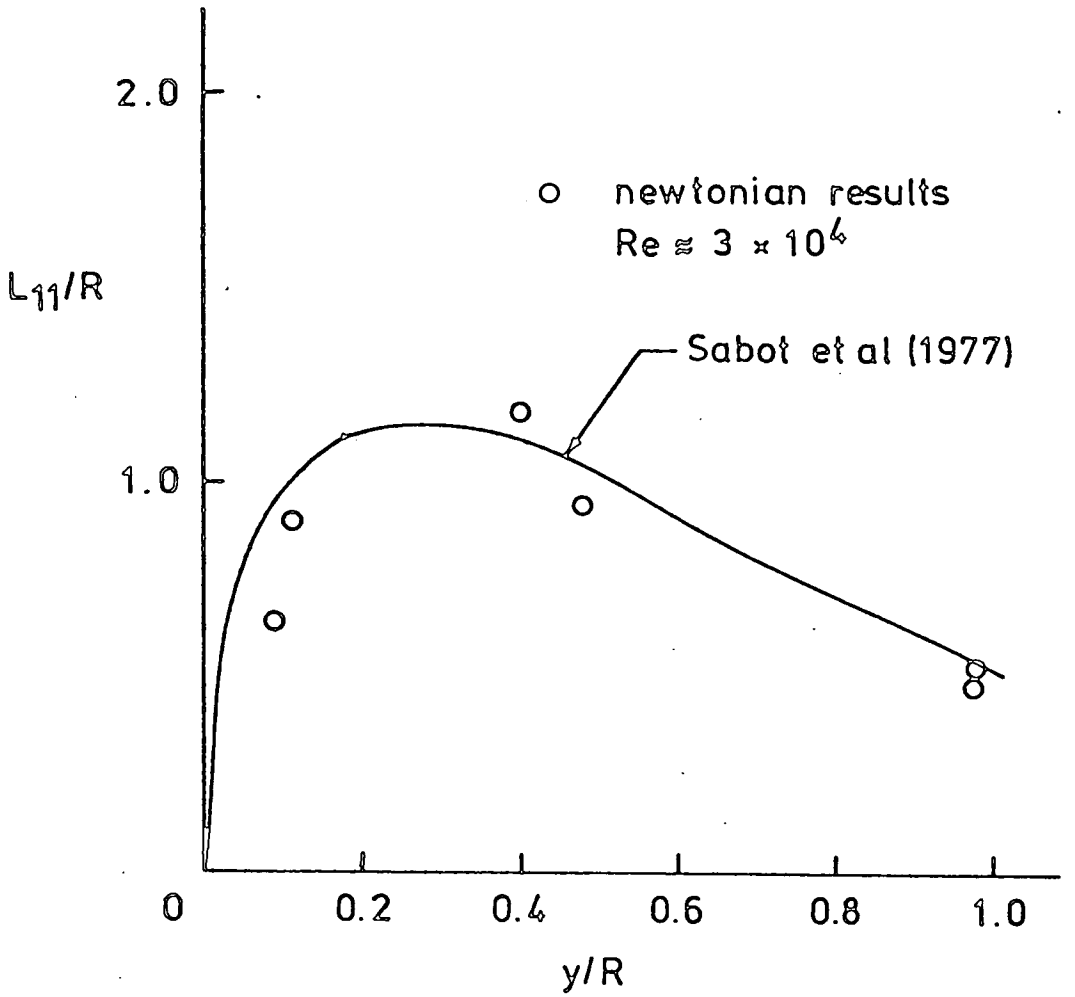

Fig 4.47 The Integral Length Scale

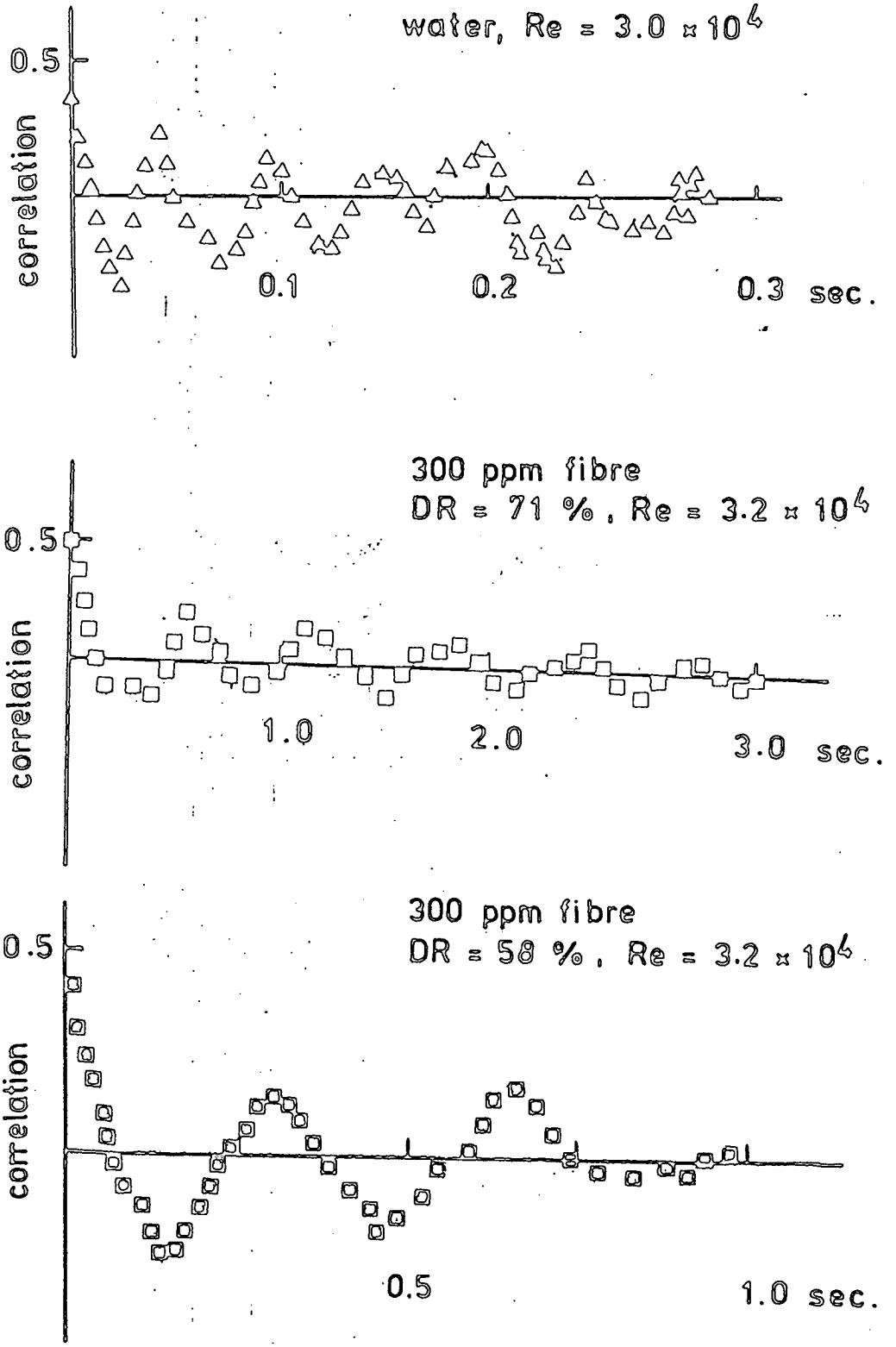

Fig 4.48 Typical Traces of The ' Short Time ' Auto-Correlation

Appendix

I. The Principle of a LDA

The principle of a LDA is based on the Doppler effect. Sometimes, one describes the operation of the system in terms of a particle crossing a fringe region. They are introduced as follows.

(1) Frequency Shift of Light Scattered by a Moving Particle

Consider a beam of light illuminating a particle moving with a velocity $\underline{V}$. According to the Doppler principle, the number of wave-fronts falling on the particle in one second will be f_p given by

$$\lambda f_p = c - \underline{V} \cdot \underline{e_i} \tag{I.1}$$

where λ is the wavelength of light, c the speed of light and $\underline{e_i}$ the unit wave vector of the incident beam.

The number of wave-fronts emitted by the particle in one second is therefore f_p.

In the mean time, a stationary observer is attempting to measure the frequency of light scattered by the moving particle. Since f_p number of wave-fronts emitted by the particle has been expanded (or suppressed) into a distance $c - \underline{V} \cdot \underline{e_s}$ due to the motion of the particle, the number of wave-fronts received in one second by the observer is

$$f = f_p \frac{c}{c - \underline{V} \cdot \underline{e_s}} \tag{I.2}$$

Thus,

$$f = \frac{c - \underline{V} \cdot \underline{e_i}}{\lambda} \cdot \frac{c}{c - \underline{V} \cdot \underline{e_s}} \tag{I.3}$$

we get

(I.4a) $$\Delta f = \frac{c - \underline{V} \cdot \underline{e_i}}{\lambda} \cdot \frac{c}{c - \underline{V} \cdot \underline{e_s}} - \frac{c}{\lambda}$$

(I.4b) $$= \frac{c}{\lambda} \cdot \frac{\underline{V} \cdot (\underline{e_s} - \underline{e_i})}{c\left(1 - \frac{\underline{V} \cdot \underline{e_s}}{c}\right)}$$

(I.4c) $$= \frac{1}{\lambda}[\underline{V} \cdot (\underline{e_s} - \underline{e_i})]$$

if $V \ll c$.

In a dual beam LDA system, two beams intersect each other in an illuminating region as shown in Figure A1. A moving particle in the region scatters light from both beams. The frequency of beam 1 is shifted in the scattering process, and the shifted value is given by

(I.5) $$\Delta f_1 = \frac{1}{\lambda}[\underline{V} \cdot (\underline{e_s} - \underline{e_{i,1}})]$$

Similarly, the shifted value for beam 2 is

(I.6) $$\Delta f_2 = \frac{1}{\lambda}[\underline{V} \cdot (\underline{e_s} - \underline{e_{i,2}})]$$

A "square-law" photodetector measures the difference of the two, giving

(I.7) $$\Delta f = \Delta f_2 - \Delta f_1 = \frac{1}{\lambda}[\underline{V} \cdot (\underline{e_{i,2}} - \underline{e_{i,1}})] \quad ,$$

which is independent of $\underline{e_s}$.

In practice this implies that in a dual-beam system, the same frequency is obtained regardless of the detection direction.

In Figure A1,

(I.8) $$\underline{V} = V_x\underline{i} + V_y\underline{j}$$

where $\underline{i}$ and $\underline{j}$ are unit vectors of the x and y axes,

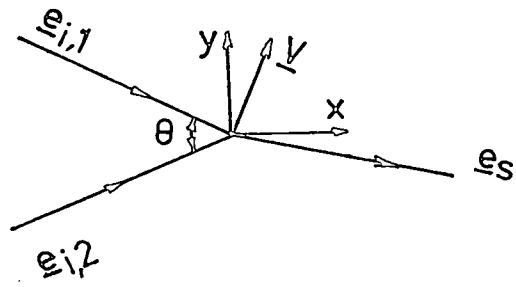

Figure A1

respectively.

(I.9) $$\underline{e}_{i,\,1} = \underline{e}^{x}_{i,\,1} + \underline{e}^{y}_{i,\,1}$$

(I.10) $$\underline{e}_{i,\,2} = \underline{e}^{x}_{i,\,2} + \underline{e}^{y}_{i,\,2}$$

$$\Delta f = \frac{1}{\lambda}\left[(V_x \underline{i} + V_y \underline{j}) \cdot (\underline{e}^{x}_{i,\,2} - \underline{e}^{x}_{i,\,1} + \underline{e}^{y}_{i,\,2} - \underline{e}^{y}_{i,\,1})\right]$$

$$= \frac{1}{\lambda}\left[(V_x \underline{i} + V_y \underline{j}) \cdot (\cos\tfrac{\theta}{2}\,\underline{i} - \cos\tfrac{\theta}{2}\,\underline{i} + \sin\tfrac{\theta}{2}\,\underline{j} + \sin\tfrac{\theta}{2}\,\underline{j})\right]$$

(I.11) $$\Delta f = \frac{2V_y}{\lambda}\sin\frac{\theta}{2}$$

In general $\lambda = \frac{\lambda_o}{n}$, where λ_o is the wavelength of light in empty space and n is the refractive index of the medium in which the beams meet.

Thus

(I.12) $$\Delta f = \frac{2V_y n}{\lambda_o}\left(\sin\frac{\theta}{2}\right) .$$

(2) Formation of Fringe Pattern

Suppose Beam 1 and Beam 2 meet at 0 in phase (Fig. A2). The beams form a crossing region of finite size. Let P(x, y) be a point in this region where (x, y) is the coordinate as shown in figure A2. In the figure we see that the path difference at the point P(x, y) is y" - x'. Transforming,

(I.13a) $$y'' = x\cos\frac{\theta}{2} + y\sin\frac{\theta}{2} ,$$

(I.13b) $$x' = x\cos\frac{\theta}{2} - y\sin\frac{\theta}{2} ,$$

we get

(I.14) $$y'' - x' = 2y\sin\tfrac{1}{2}\theta .$$

Dark region occurs when the path difference is equal to the odd number of half wavelengths. That is

(I.15) $$2y\left(\sin\tfrac{1}{2}\theta\right) = \frac{\lambda}{2}, \frac{3\lambda}{2}, \frac{5\lambda}{2}, \cdots .$$

Thus, the fringe spacing is given by

(I.16a) $$b = \frac{3\lambda}{4 \sin\frac{\theta}{2}} - \frac{\lambda}{4 \sin\frac{\theta}{2}}$$

(I.16b) $$= \frac{\lambda_o}{2n \sin\frac{\theta}{2}}$$

Imagine now a small particle passing through the pattern, there will be some time that the particle disappears due to its presence in the dark region, and other time that it appears when it is present in the bright region. Flashes of light should appear, and this sequence of flashes contained the information of the motion of the particle. That is, the interval between two subsequent flashes is given by

(I.17) $$t = \frac{b}{V_y} \quad ,$$

where V_y is the velocity of the particle in the y direction. Therefore, the frequency of the flashes is

(I.18a) $$f = V_y/b$$

(I.18b) $$= \frac{2nV_y \sin\frac{\theta}{2}}{\lambda_o} \quad ,$$

which is equivalent to equation (I.12).

II. Geometry of the LDA for Transverse Measurement

Figure A3.a shows the light path entering the side walls of the pipe with water in it, the arrows indicating the direction of the light path. In the figure, S is the location of the probe volume, M a point on the outer surface of the pipe. MR is the actual distance the optical system travels, starting from M. This distance can be measured by the micrometer which is mounted on the steel plate of the optical system. The problem is to find the value of NS in terms of MR and to find the angle, $\angle$NSJ.

Figure A3.b shows the triangle MOI and the refracted path IT. The notations are as indicated in the figure, and MO = OI = r. By the sine rule

$$\frac{MR}{\sin \angle MIR} = \frac{MI}{\sin \gamma},$$

$$MR = \frac{\sin(180^\circ - 90^\circ + \frac{\delta}{2} - \gamma)}{\sin \gamma} MI.$$

$$MR = \frac{\cos(\gamma - \frac{\delta}{2})}{\sin \gamma} MI. \qquad \text{(A3.1)}$$

Similarly,

$$\frac{r}{\sin(90^\circ - \frac{\delta}{2})} = \frac{MI}{\sin \delta},$$

$$MI = \frac{\sin \delta}{\cos \frac{\delta}{2}} r \qquad \text{(A3.2)}$$

Substituting MI in (A3.1) we get

$$MR = \frac{\cos(\gamma - \frac{\delta}{2})}{\sin \gamma} \frac{\sin \delta}{\cos \frac{\delta}{2}} r \qquad \text{(A3.3)}$$

Considering ΔMTI, similarly, we obtain

$$(A3.4) \qquad MT = \frac{\cos(\theta - \frac{\delta}{2})}{\sin\theta} \frac{\sin\delta}{\cos\frac{\delta}{2}} r$$

therefore

$$(A3.5) \qquad MT = \frac{\cos(\theta - \frac{\delta}{2})}{\cos(\gamma - \frac{\delta}{2})} \frac{\sin\gamma}{\sin\theta} MR$$

Relating θ and γ, we must apply Snell's law, obtaining

$$(A3.6) \qquad \frac{\sin(\gamma - \delta)}{\sin(\theta - \delta)} = \frac{n_p}{n_a}$$

where n_p is the refractive index of the pipe and n_a is that of air.

Therefore, MT and θ can be calculated from equations (A3.3), (A3.4) and (A3.6), MR and γ being measurable parameters.

Figure A3.c shows the triangle NOJ and the refracted path JS. NO = OJ = R_o.

Similarly, we get

$$(A3.7) \qquad NS = \frac{\cos(\Omega - \frac{\Delta}{2})}{\sin\Omega} \frac{\sin\Delta}{\cos\frac{\Delta}{2}} R_o$$

$$(A3.8) \qquad NT = \frac{\cos(\phi - \frac{\Delta}{2})}{\sin\phi} \frac{\sin\Delta}{\cos\frac{\Delta}{2}} R_o$$

and

$$(A3.9) \qquad \frac{\sin(\phi - \Delta)}{\sin(\Omega - \Delta)} = \frac{n_w}{n_p}$$

NT is given by,

$$(A3.10) \qquad NT = MT - (r - R_o)$$

and ϕ is equal to θ already obtained.

Thus, measuring MR and γ, we can use equations (A3.3), (A3.4), (A3.6), (A3.7), (A3.8), (A3.9) and (A3.10)

to find the values of NS and Ω . However, the relations are so implicit that we cannot get them easily.

Alternatively we can use a graphical method to accomplish this task.

The side walls of the pipe in figure A3.a can be considered as a lens. The first 'air-persplex' interface has a radius of curvature r and the second 'persplex-water' interface has a radius of curvature R_o. The lens formulae for these two interfaces are written as:

(A3.11) $$\frac{n_p}{MT} = \frac{n_p - n_a}{r} - \frac{n_a}{MR} \qquad r > 0 \qquad MR < 0 \quad ,$$

and

(A3.12) $$\frac{n_w}{NS} = \frac{n_p - n_w}{R_o} - \frac{n_p}{NT} \qquad R_o < 0 \quad ;$$

the sign convention is given in the Advanced Level Physics.

The graphical method is described as follows.

On a large sheet, draw two concentric circles of radii $5R_o$ and 5r, i.e. scale 5:1. Here, we used a number of MR values to calculate their corresponding values of NS and NSJ. Following the notations as shown in figure A3.a, draw the line RI making an angle γ with MO. By equation (A3.11) MT can be obtained with a known value of MR; thus T can be determined. Then join IT cutting the inner circle at J. Similarly, by equation (A3.12), NS can be obtained since NT (= MT - MN). Joining JS, we can measure $\angle$NSJ. Repeat the same procedure to find NS and Ω as a function of MR.

Using this method, we obtained a curve relating to NS, as shown in figure 3.5.

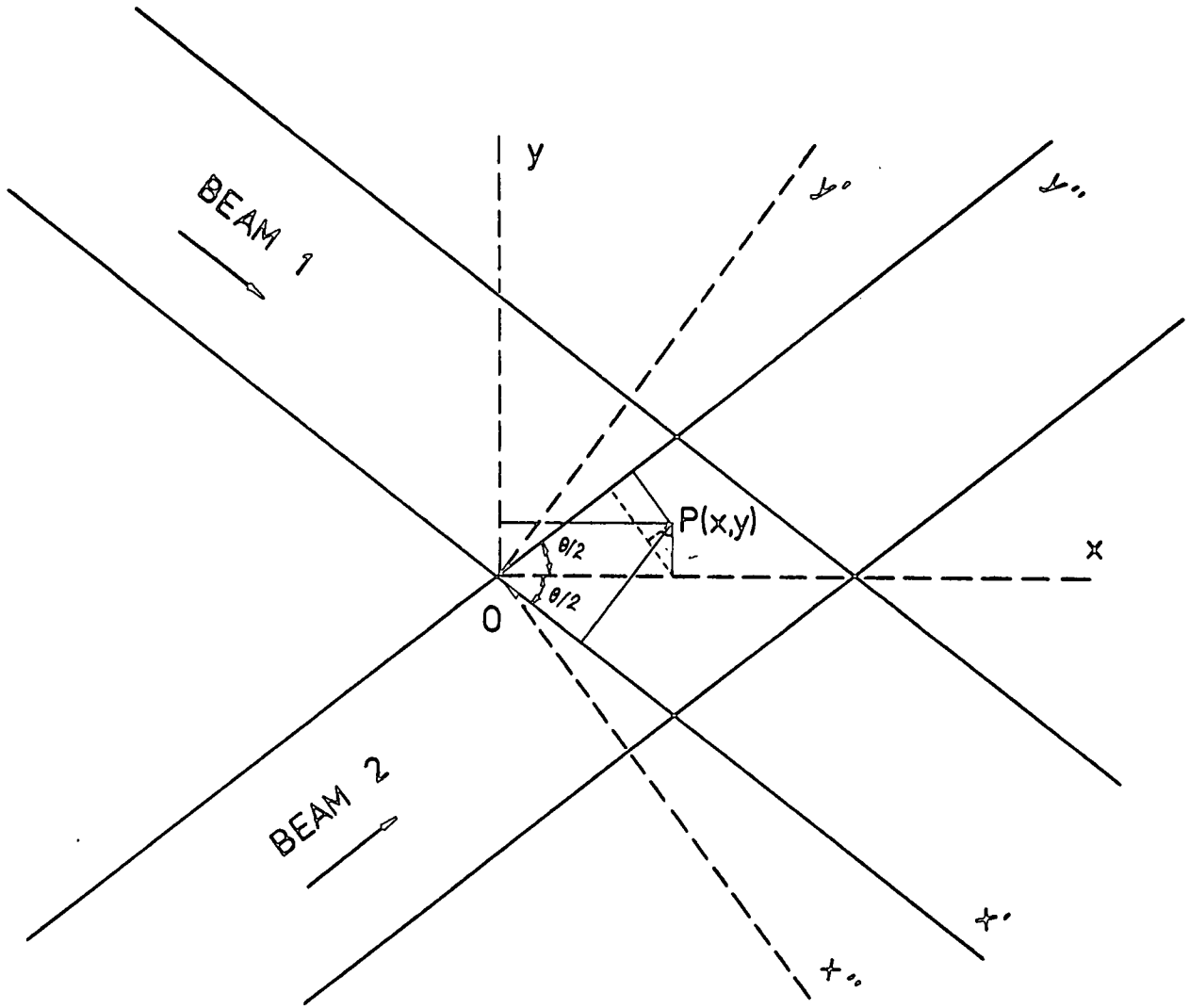

Fig A2 Formation of Fringe Pattern

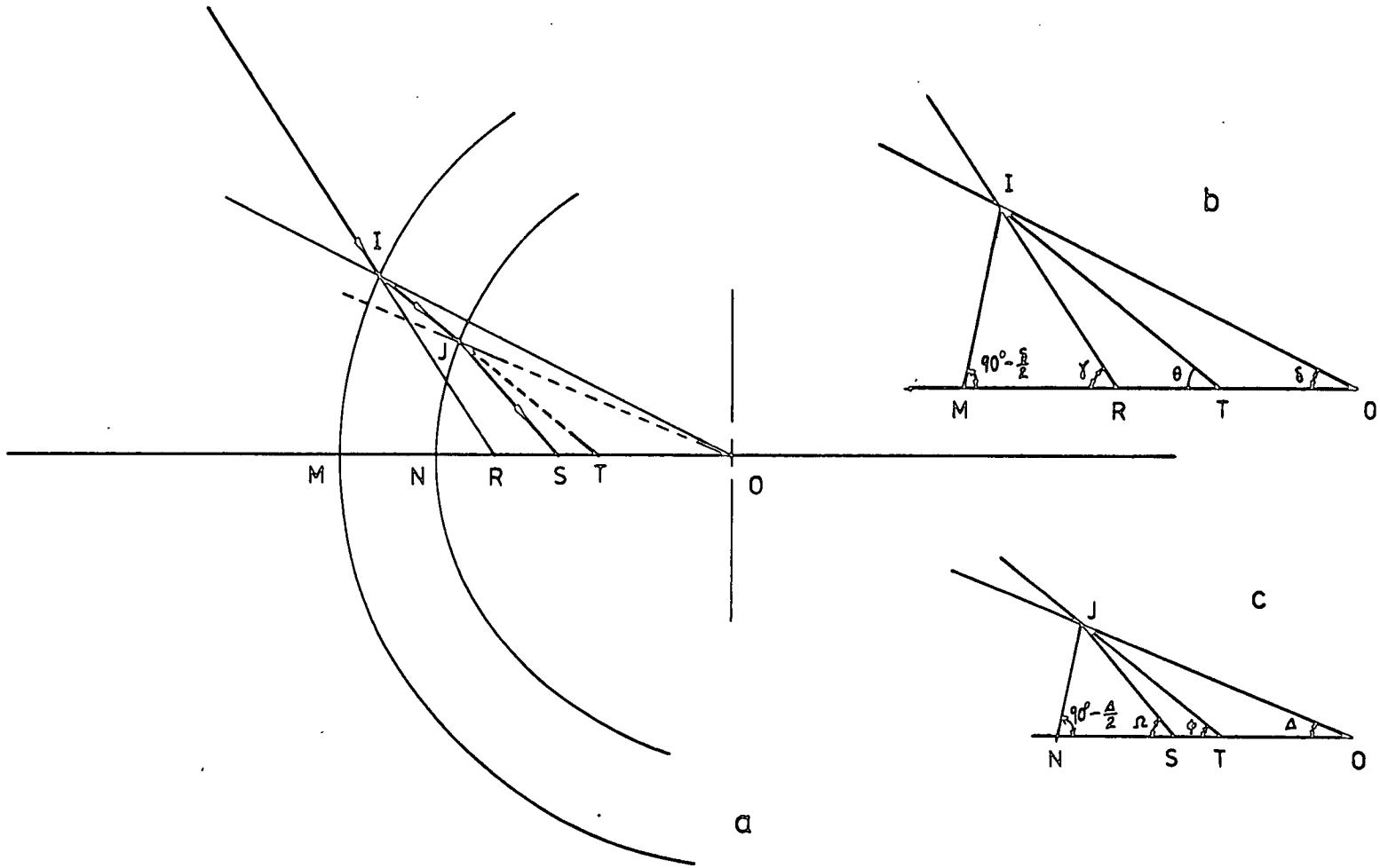

Fig A3 Light Path entering the Side Walls